

Durham E-Theses

Pion interactions in Hydrogen and Deuterium

Geoffrey Arthur Briggs

How to cite:

Briggs, Geoffrey Arthur (1966) Pion interactions in Hydrogen and Deuterium. Doctoral thesis, Durham University.

Use policy

The full-text may be used and/or reproduced, and given to third parties in any format or medium, without prior permission or charge, for personal research or study, educational, or not-for-profit purposes provided that:

- a full bibliographic reference is made to the original source
- a <https://etheses.durham.ac.uk/id/eprint/8602/> is made to the metadata record in Durham E-Theses
- the full-text is not changed in any way

The full-text must not be sold in any format or medium without the formal permission of the copyright holders.

Please consult the [full Durham E-Theses policy](#) for further details.

PION INTERACTIONS IN HYDROGEN AND DEUTERIUM

A Thesis Presented By

Geoffrey Arthur Briggs

for the

Degree of Doctor of Philosophy

at the

University of Durham

August 1966



CONTENTS

	Page
<u>PREFACE</u>	iv
<u>LIST OF FIGURES</u>	v
<u>I. PRODUCTION</u>	1
<u>CHAPTER 1 <u>EXPERIMENTAL CONDITIONS</u></u>	3
1.1 The Deuterium Exposure	3
1.11 The M2 Beam	3
1.12 The Saclay 31 cm. Bubble Chamber	5
1.2 The Exposure in Hydrogen	6
1.21 The O2 Beam	6
1.22 The British National Hydrogen Bubble	8
1.23 Distortions	9
<u>CHAPTER 2 <u>DATA REDUCTION</u></u>	12
2.1 Scanning	12
2.11 Scanning Tables	12
2.12 Scanning the Hydrogen Film	13
2.13 Efficiency of Scanning	14
2.14 Scanning the Deuterium Film	14
2.2 Labelling	16
2.3 Measurement	16
2.31 Measuring Tables	18

	Page
2.4 Data Processing	20
2.41 REAF	21
2.42 TRESH	22
2.43 GRIND	23
2.5 Examination and Analysis	25
2.51 χ^2 Limits	27
2.52 Data Summary Tape	28
2.53 SUMK	29
2.6 Phase Space	29
<u>CHAPTER 3</u> <u>ELASTIC SCATTERING OF π^+ MESONS IN</u>	
<u>DEUTERIUM AT 5 GEV/C</u>	31
3.1 Introduction	31
3.11 Techniques for Studying Elastic Scattering in Deuterium	34
3.2 The Optical Model	36
3.3 High Energy Scattering in the Impulse Approximation	39
3.4 The Deuteron Wave Function	46
3.5 Experimental Analysis	49
3.51 Corrections for Scanning Loss	54
3.52 Experimental Differential Cross Section	56
3.6 Optical Model Calculations	57
3.7 Impulse Model Calculations	63

CHAPTER 4 INELASTIC π^+ p INTERACTIONS OF HIGH
MULTIPLICITY AT 5 GEV/c

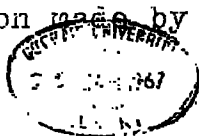
4.1	Introduction	67
4.11	The Peripheral Model	68
4.2	Experimental Results	72
4.21	Cross Sections	73
4.22	Distributions of M^2 and x^2	75
4.23	Effective Mass Distributions of $p\pi^+$, $\pi^+\pi^-$, and $p\pi^-$	76
4.24	Angular Distributions of the Secondary Particles	79
4.25	Distribution of Δ^2 between the Incident Proton and the $p\pi^+$	81
4.26	Three-pion effective mass Distributions, $\pi^+\pi^+\pi^-$ and $\pi^+\pi^-\pi^-$	83
4.27	Four-pion effective mass Distribution, $\pi^+\pi^+\pi^-\pi^-$	86
4.28	Higher Nucleon Isobars	87
4.29	Decay Distribution of the $\pi^+\pi^-$	87
	<u>CONCLUSIONS</u>	90
	<u>ACKNOWLEDGEMENTS</u>	93
	<u>REFERENCES</u>	94

PREFACE

The work described in this thesis concerns two bubble chamber experiments which have been performed to investigate certain aspects of the scattering of high energy π mesons in hydrogen and deuterium.

The trend in bubble chamber experiments is towards the analysis of larger numbers of photographs to obtain greater statistical analysis and to examine events which occur with very small cross sections; generally the facilities of several laboratories are combined for the analysis of the data. Both experiments reported here have been performed in such collaborations. The study of the elastic scattering of 6 GeV/c π^+ mesons in deuterium is the combined work of the Ecole Polytechnique, Paris and CERNA and Durham University. The investigation of the inelastic scattering of 5 GeV/c π^+ mesons in hydrogen has been undertaken by the Universities of Bonn, Durham, Nijmegen, Paris (E.P.), Strasbourg and Turin. The exposure, in which the author assisted, was planned by representatives of all the laboratories and was made at CERNA.

The results presented in this thesis represent that part of the analysis which was the particular concern of the author. Acknowledgement is made in the text to any specific contribution made by his colleagues.



LIST OF FIGURES

Figure

- 1 - Schematic Layout of the M2 Beam
(from Goldberg J., and Perreau J.M., CERN 63-12)
- 2 - Optical System of Saclay 81 cm. Bubble Chamber
- 3 - Camera Position of Saclay 81 cm. Bubble Chamber
- 4 - Interaction of π^+ meson in the Deuterium of the
Saclay 81 cm. Bubble Chamber. The Fiducial Volume
is indicated.
- 5 - Schematic Layout of the O2 Beam
(from Keil E., and Neale W.W., CERN/TC/O2 63-3)
- 6 - Plan View of B.N.H.B.C. showing Optical System and
Magnet (from CERN Courier, September 1964)
- 7 - Photograph of Interaction of 5 GeV/c π^+ meson in the
B.N.H.B.C. The Fiducial Volume is indicated
- 8 - Flow Diagram of the Analysis of Events
- 9 - Measuring and Recording Layout
- 10 - Schematic Diagram of Coordinate Punching
- 11 - Gartenhaus S-Wave Function with Hulthen Wave Function
and Approximate Hard Core Wave Function
(from Moravcsik M.J., Nuclear Physics, 7, 113)
- 12 - Distribution of the Projected Angle Between the
Proton and Neutron
- 13 - Distribution of quantity 'A' for Different Momentum
Zones of Recoil
- 14 - Distribution of Events Found as function of Angle
of Recoil in Chamber for Different Momentum Zones
- 15 - Ratio of E.P. and CERN-Durham Scanning Efficiencies
as function of recoil momentum
- 16 - Correction Factor for Scanning Loss as function of
Deuteron Momentum
- 17 - Comparison of Experimental Differential Cross Section
with Predictions of Optical Model

Figure

- 18 - Variation of Ks with Impact parameter, ρ , for Uniform Deuteron and for Deuteron described by Hulthen and Hard Core Wave Functions
- 19 - Comparison of Experimental Differential Cross Section with Predictions of Impulse model
- 20 - Feynman Diagram for Reaction $a+b \rightarrow c+d$
- 21 - Distribution of Squared Missing Mass
- 22 - Distribution of α^2
- 23 - Effective Mass of $p\pi^+$
- 24 - Effective Mass of $\pi^+\pi^-$
- 25 - Effective Mass of $p\pi^-$
- 26 - Angular Distributions in the Centre of Mass, p, π^+, π^-
- 27 - Angular Distributions in the Centre of Mass $p\pi^+, \pi^+\pi^-$
- 28 - Distribution of Production Angle of $p\pi^+$ Combination for condition $1120 < M(p\pi^+) < 1320$ MeV
- 29 - Distribution of $\Delta^2(p\pi^+/p)$, (a) Overall
(b) for $1120 < M(p\pi_1^+) < 1320$ MeV
 $670 < M(\pi_2^+\pi_1^-) < 850$ MeV
 $-1 < \cos\theta^* < -0.75$
- 30 - Effective Mass of $\pi^+\pi^+\pi^-$
- 31 - Effective Mass of $\pi^+\pi^-\pi^-$
- 32 - Effective Mass of $\pi_2^+\pi_1^+\pi_3^-$ for
 $1120 < M(p\pi^+) < 1320$ MeV
 $670 < M(\pi^+\pi^-) < 850$ MeV
(a) $-1 < \cos\theta^* < -0.75$ (b) $-0.75 < \cos\theta^* < 0$

Figure

- 33 - Effective Mass of $\pi^+\pi^+\pi^-\pi^-$
- 34 - Effective Mass of $p\pi^+\pi^+$
- 35 - Effective Mass of $p\pi^+\pi^-$
- 36 - Effective Mass of $p\pi^+\pi^-\pi^-$
- 37 - Effective Mass of $p\pi^+\pi^+\pi^-$
- 38 - Decay Distribution of $\pi_2^+\pi_1^-$ for

$$1120 < M(p\pi_1^+) < 1320 \text{ MeV}$$

$$-1 < \cos \frac{x}{p\pi_1^+} < -0.75$$

(a) $670 < M(\pi_2^+\pi_1^-) < 850 \text{ MeV}$

(b) $490 < M(\pi_2^+\pi_1^-) < 670 \text{ MeV}$

(c) $850 < M(\pi_2^+\pi_1^-) < 1010 \text{ MeV}$

INTRODUCTION

The first beams of pions with energies into the GeV region became available a little over ten years ago and since then an intensive effort has been made to examine the pion-nucleon interaction which is fundamental to the understanding of strong interactions. The inelastic processes have proved to be particularly suitable to be examined by the bubble chamber technique as the multiple production of particles, which is the dominating feature of pion-nucleon interactions in the GeV region, cannot be observed easily in any other way at present. Over the last few years many resonances have been discovered between the particles of the final state and many of their properties e.g. their cross sections, lifetimes and quantum numbers have been determined from bubble chamber experiments. This information has provided the basis for various theoretical models for particle production in this energy region, the most successful of which has been the peripheral model. There is still, however, no universal theory to explain all phenomena observed and much more information about the less frequent processes is needed. An increasing number of bubble chamber photographs are becoming available for analysis and the study of interactions of very small cross section has become possible. Such a study is reported in Chapter 4 concerning the production of six charged particles in the final state when 5 GeV/c π^+ mesons interact in a hydrogen bubble chamber.

Experiments in deuterium bubble chambers have generally been performed to study scatterings on the loosely bound neutron which closely resembles a free particle in its inelastic interactions. However, information other than on π -n scattering can be learned from collisions of pions in deuterium; knowledge of the bound nucleon-nucleon state can be obtained by observing interactions with the deuteron as a whole, such as elastic scatterings. At present only bubble chambers and nuclear emulsions have sufficient resolution to distinguish between elastic scatterings and interactions in which the proton and neutron are separated. In Chapter 3 an investigation into the elastic scattering of 6 GeV/c π^+ mesons in a deuterium bubble chamber is described. A report is given of the determination of the angular distribution of the scattered pions at this momentum and of the comparison of different deuteron wave functions for the interpretation of the experimental data.

The first two Chapters contain a description of the experimental and analytic techniques used in the evaluation of the data. The experimental conditions are described in Chapter 1 and details of the data reduction, common to both experiments, are given in Chapter 2. It has been considered appropriate to introduce the last two chapters separately.

CHAPTER 1

EXPERIMENTAL CONDITIONS

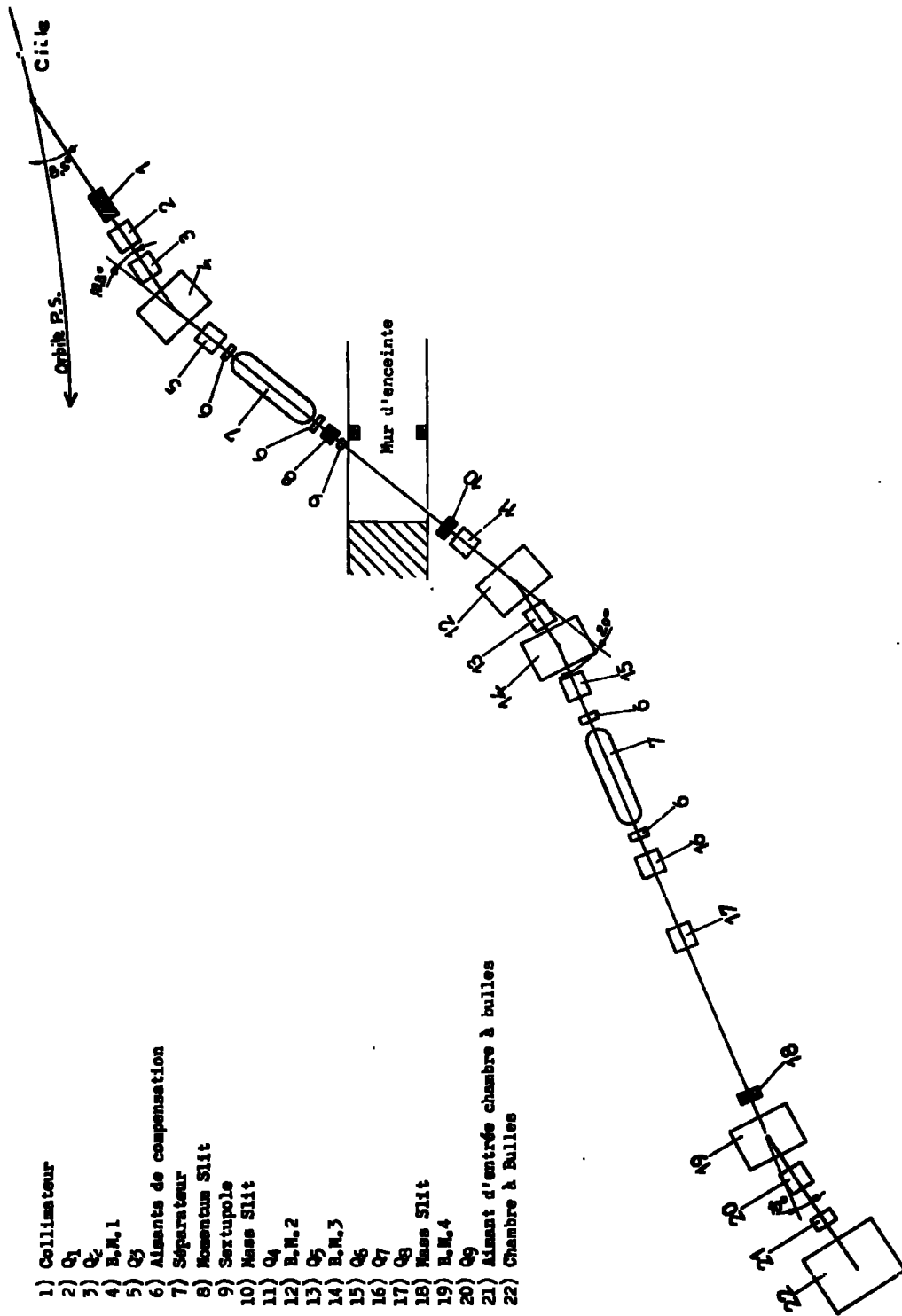
Two exposures have been made at CERN, one with the M2 beam and the Saclay 81 cm. Bubble Chamber filled with deuterium, and the second using the O2 beam and the 150 cm. British national Hydrogen Bubble Chamber (B.N.H.B.C.). The essential features of the beams and bubble chambers are described briefly here and fuller details can be found in the references given.

1.1 The Deuterium Exposure

An exposure was made in June 1963 in which a total of about 70,000 photographs were taken of the Saclay Bubble Chamber to provide data for a general study by CERN and the Ecole Polytechnique, Paris of the interactions of 6 GeV/c π^+ mesons in deuterium, and by Durham, also, of certain aspects of the two- and six-pronged interactions.

1.11 The M2 Beam

The layout of the M2 beam is shown in figure 1 and a complete description is given in the CERN internal report of Goldberg and Perreau (1963). The beam was built specifically to provide separated kaon beams up



- 1) Collimateur
- 2) Q1
- 3) Q2
- 4) B.M.1
- 5) Q3
- 6) Aisants de compensation
- 7) Séparateur
- 8) Momentum Slit
- 9) Sertupole
- 10) Mass Slit
- 11) Q4
- 12) B.M.2
- 13) Q5
- 14) B.M.3
- 15) Q6
- 16) Q7
- 17) Q8
- 18) Mass Slit
- 19) B.M.4
- 20) Q9
- 21) Aisants d'entrée chambre à bulles
- 22) Chambre à Bulles

FIG. 1 SCHEMATIC LAYOUT OF THE M2 BEAM (Goldberg and Perreau, 1963)

to 3.5 GeV/c and antiproton and pion beams are also available up to 6 GeV/c. The length of the beam from target to the Saclay Bubble Chamber is 87 m. The beam is produced at an angle of 8.5° to the internal P.S. beam to provide a suitable intensity of particles (particularly kaons) in the chamber. The production of secondary particles from the target is peaked strongly forward and the angle is therefore kept as low as possible. Momentum separation takes place in the first part of the beam; the first bending magnet B.M. 1 produces dispersion in the horizontal image at the slit no. 8 where the momentum bite is defined. The quadrupole triplet Q1, Q2, and Q3 at the start of the beam produces a converging beam in the first 10 m. electrostatic separator and a focus at the mass slit no. 10. In the second identical mass separator the beam is horizontal so that the maximum separation may be produced and the final mass separation is made at the slit no. 18 where the beam is focussed by the doublet Q7 and Q8. Before entering the bubble chamber the beam is given the desired spread by the quadrupole magnet Q9.

The beam momentum during the exposure was computed by the programme 'TRAMP' to be 6.07 GeV/c.

1.12 The Saclay 81 cm. Bubble Chamber

The Saclay Chamber has a conventional through-illumination system, shown in figure 2, which uses vertical linear flash tubes as light sources focussed by two-section condensers. The chamber windows, 81 cm. in length, are rectangular with semi-circular ends and the depth of the chamber is 32 cm. For this exposure the chamber was filled with about 100 litres of liquid deuterium. The three cameras were located in the positions shown in figure 3 and 35 mm. unperforated film was used. The chamber was expanded and photographed every two seconds. The reference system of crosses engraved on to the inner surfaces of the windows was used to define the fiducial volume as shown in figure 4 which is a photograph taken by the lower camera, View 3. It was necessary to define the fiducial volume on this view instead of the usual central view because the photographs taken by camera 2 were of poor quality and difficult to scan. The magnetic field varied by up to 4% at the edges of the chamber, having an average value of 20.0 Kilogauss and was measured accurately throughout the chamber. The distortion of the optical system and of the chamber as a whole is very small and the trajectories of the tracks have been reconstructed in the geometry programme 'THRESH'

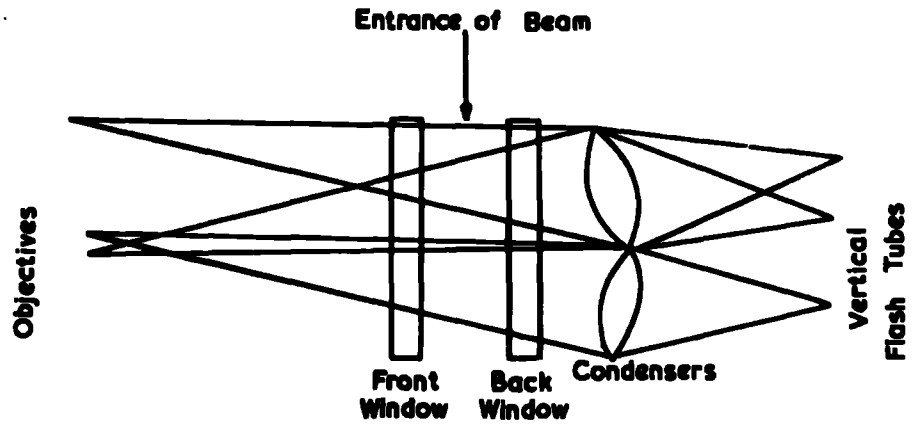


FIG. 2 OPTICAL SYSTEM OF SACLAY 81cm BC.

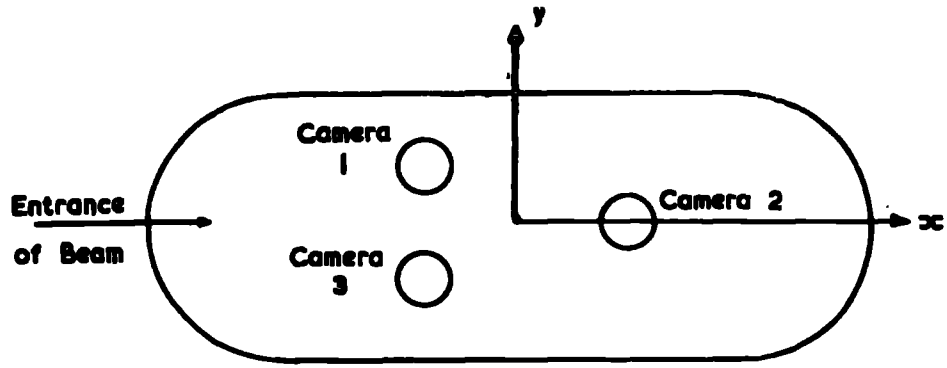
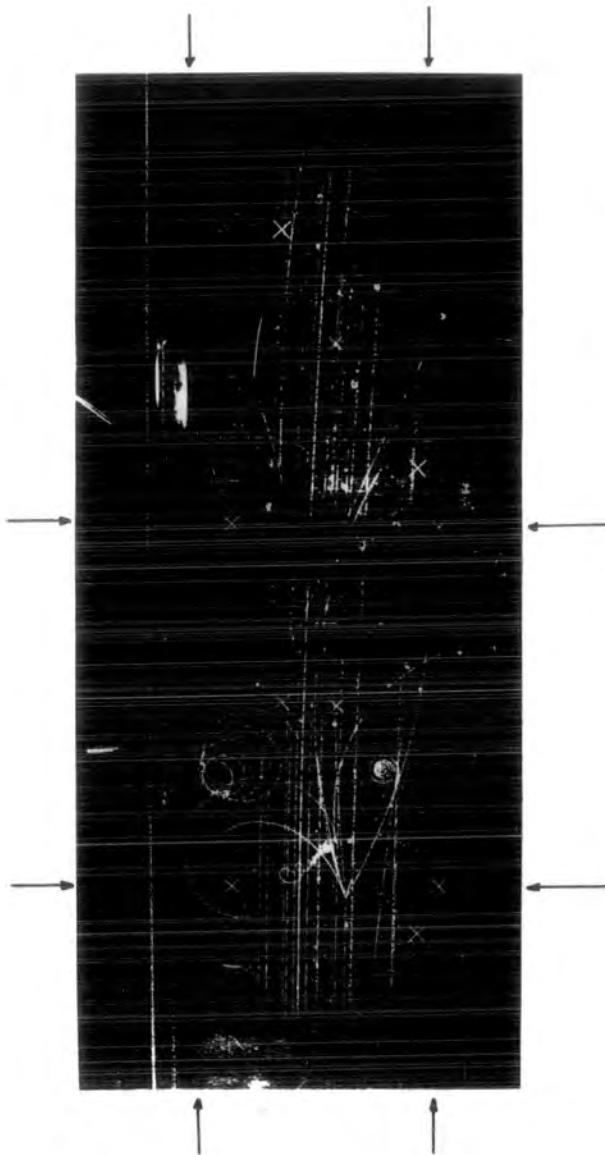


FIG. 3 CAMERA POSITIONS OF SACLAY 81cm BC.



Interaction of π^+ meson in
the Deuterium of the Saclay
81 cm. Bubble Chamber. The
Fiducial Volume is indicated.

Figure 4

without difficulty. No corrections for distortions have therefore been attempted.

1.2 The Exposure in Hydrogen

Approximately 150,000 photographs were taken of the B.N.H.B.C. exposed to a beam of π^+ mesons of 4.98 GeV/c momentum in an experimental run during February 1965. The film was divided between the five collaborating laboratories - Bonn, Durham, Paris (E.P.), Nijmegen, and Turin; subsequently the film of the Ecole Polytechnique was shared with Strasbourg. The run was made in the East Experimental Area using the O2 beam.

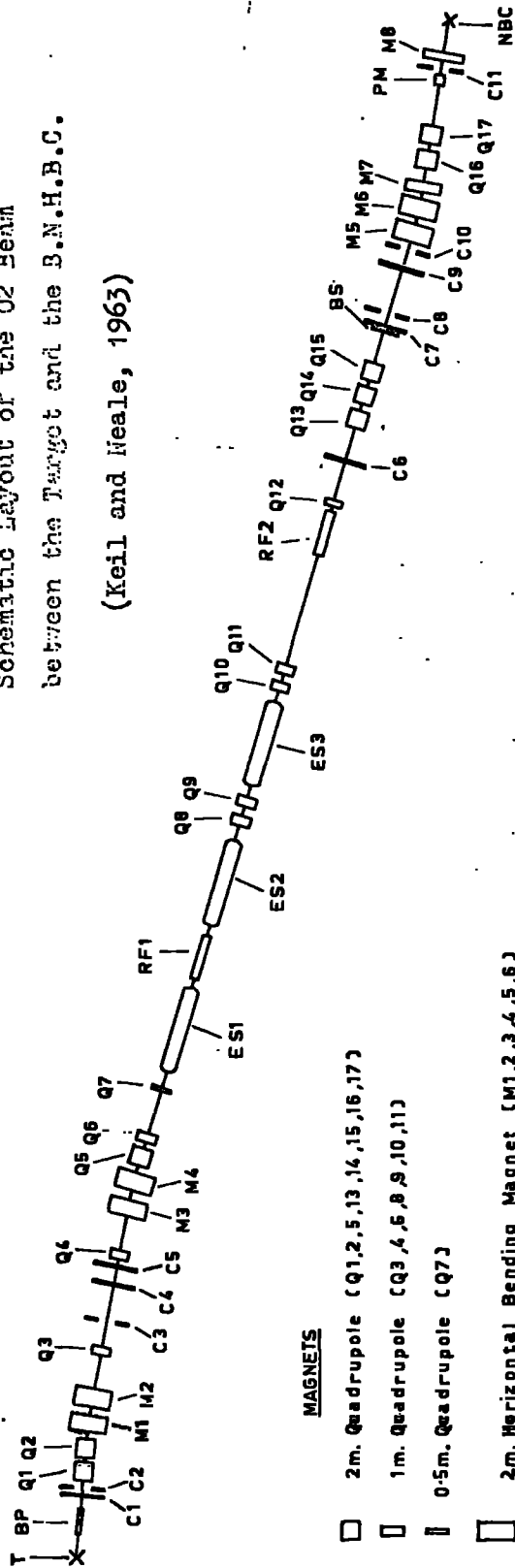
1.21 The O2 Beam

The O2 beam was built to provide reasonably well separated beams of kaons, protons, antiprotons and pions with momenta up to 15 GeV/c. Initially the beam served the British 150 cm. chamber and in this experiment was set up to produce a beam of π^+ mesons at a momentum of close to 5 GeV/c. The beam, described fully by Keil and Neale (1963), is interesting technically because it combines in a single channel both electrostatic and R.F. separation. However, for the purpose of providing the π^+ beam at this momentum only the electrostatic separators were needed, the R.F. separation being of greater

efficiency at higher momenta.

The layout of the beam, which is about 180 m. long between the target and chamber, is shown in figure 5. The internal target produces positive particles at an angle of 5.1° . The circulating proton beam of the P.S. had an intensity of about 5.10^{11} protons per pulse and the O2 beam was given about 10% of the intensity. In the first part of the beam the angular acceptance and the momentum bite are initially defined. In the second part, after mass separation the angular acceptance and momentum selection are redefined and the beam is finally shaped for entry into the bubble chamber. The angular acceptance from the target is defined by the collimators C1 and C2 and later, in the final stage, by C9 in the vertical plane and by the vertical bending magnet in the horizontal plane. The bending magnets M1, M2, M3, and M4 and the horizontal collimator C3 provide the momentum selection in the first stage and C11 redefines the momentum bite just before the beam enters the chamber. The quadrupole triplet q1, q2, and q3 focusses the beam at the centre of the collimator C4 in the vertical plane which then acts as a source for the mass analysis stage. The lens triplet q4, q6, and q7 produces a parallel beam

Schematic layout of the O2 Beam
 between the Target and the B.N.H.B.C.
 (Keil and Neale, 1963)



MAGNETS

- 2m. Quadrupole (Q1,2,5,13,14,15,16,17)
- 1m. Quadrupole (Q3,4,5,8,9,10,11)
- ▮ 0.5m. Quadrupole (Q7)
- 2m. Horizontal Bending Magnet (M1,2,3,4,5,6)
- ▮ 1m. Vertical Bending Magnet (M7,8)
- ▮ 1m. Pulsed Vertical Bending Magnet (PM)

SEPARATORS

- ▮ Electrostatic Separator (ES1,2,3)
- ▮ Radiofrequency Separator (RF1,2)

COLLIMATORS

- ▮ Horizontal Collimator (C2,3,8,10,11)
- ▮ Vertical Collimator (C1,4,5,6,7,9)
- ▮ Beam Stopper (BS)

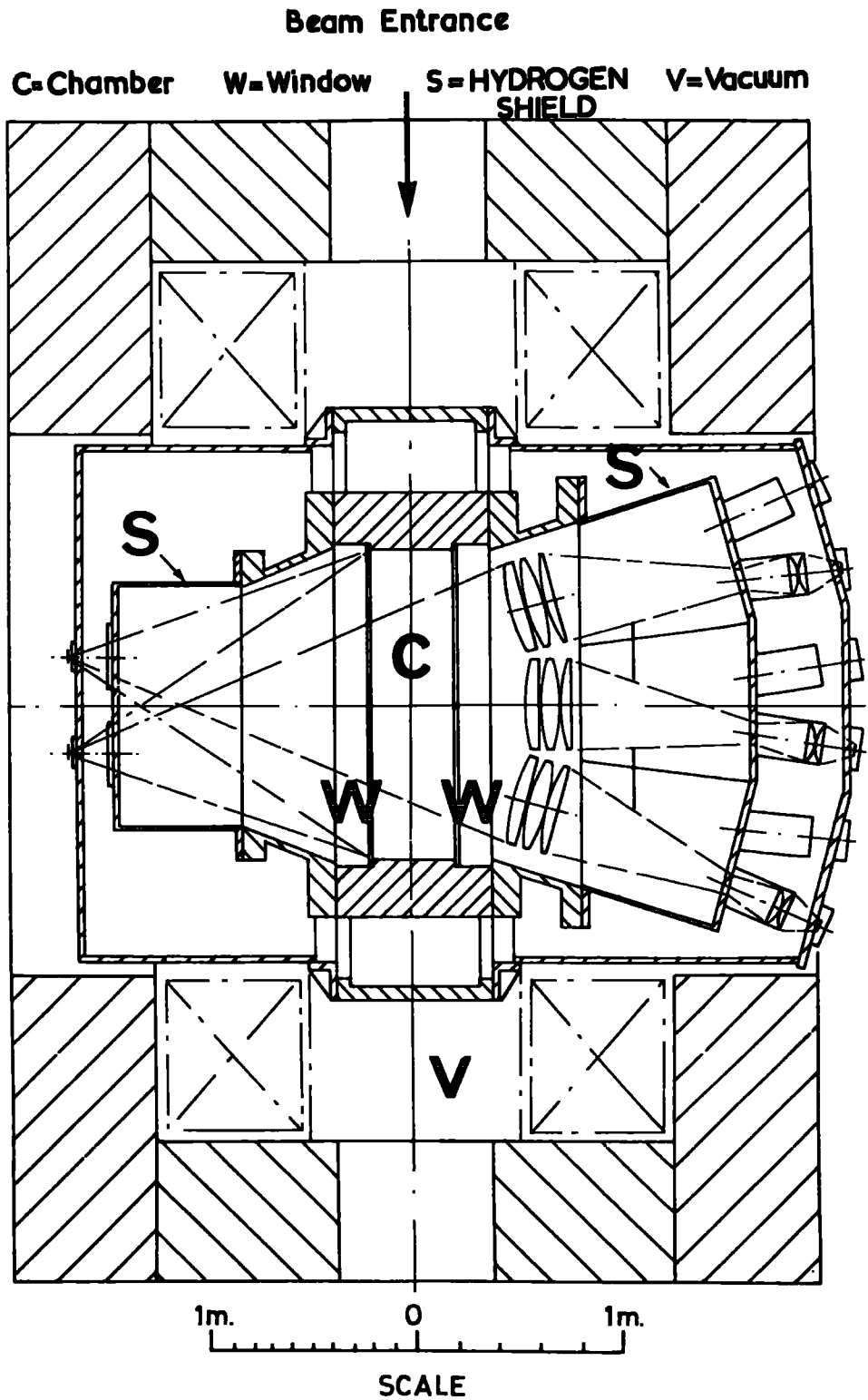
- T = Target
- NBC = Bubble Chamber

Fig 5

in the vertical plane and an intermediate focus inside the mass separators which have a total plate length of 27 m. The final mass analysis is made at collimator C6. The beam is brought to a sharp vertical focus just inside the bubble chamber by Q16 and Q17 and this is then swept across the chamber by the pulsed magnet PM.

1.22 The British National Hydrogen Bubble Chamber

The initial testing and operation of the B.N.H.B.C. took place at CERN. The chamber is described in several papers e.g. Welford (1964). The aperture of the two plane parallel windows is rectangular with semi-circular ends and the clear dimensions are 150 cm. by 50 cm. The windows are 15.5 cm. thick and the spacing between the inner faces is 45.0 cm. producing an effective volume of liquid hydrogen seen by the three cameras of about 300 litres. The optical system is of the through-illumination type using ring-shaped flash tubes and a condenser system in three sections. The cameras, 122.2 cm. from the front window, have axes which are perpendicular to the windows and they are loaded with 35 mm. unperforated film in 300 m. lengths. The chamber, its surrounding magnet and the optical system are shown diagrammatically in figure 6.

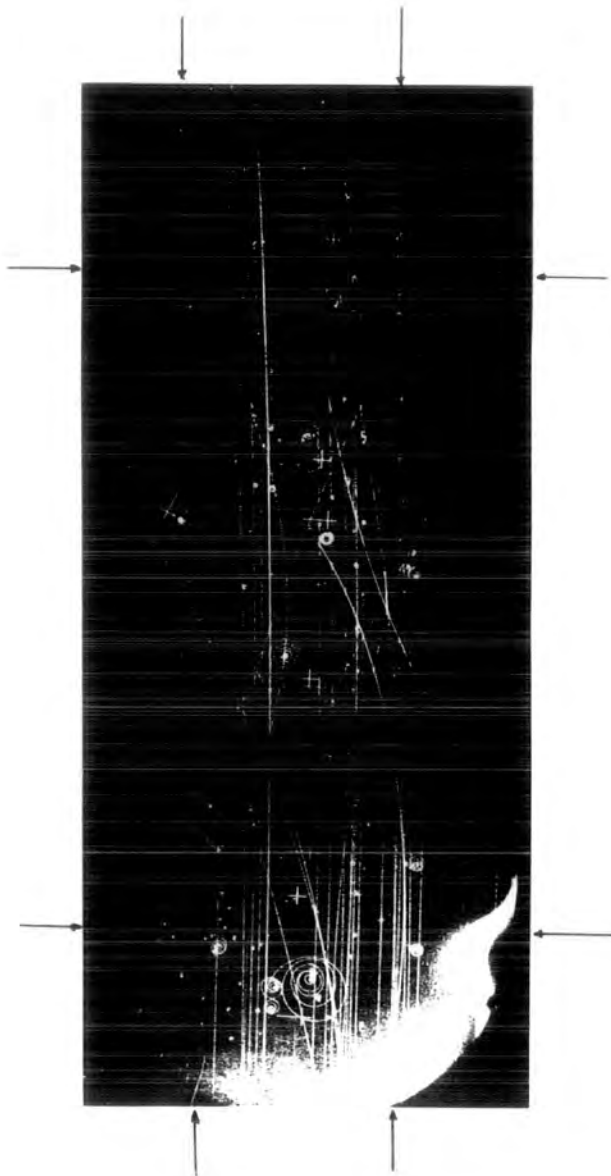


**FIG. 6 PLAN VIEW OF B.N.H.B.C. SHOWING
OPTICAL SYSTEM AND MAGNET.**

Again, the reference system of the chamber in the form of engraved crosses on the inner window surfaces is used to define the fiducial volume and this may be seen in a photograph taken by the central camera, figure 7. The crosses on the camera-side have four equal arms and on the light-side have one longer arm. During the experiment the film was monitored and the chamber working conditions adjusted to produce minimum ionisation tracks with twelve bubbles per mm. The magnetic field had an average field strength of 13.5 kilogauss and varied by about 3% at the sides of the chamber. The field strength was accurately measured throughout the chamber and the results of this survey recorded in the usual way in matrix form for use in the fitting programme.

1.23 Distortions

The distortions produced by the optical system of the chamber are not negligible and reliable geometrical reconstruction is not possible without making corrections. Kellner (1965) has made a study of the corrections required and these are now included in the geometry programme THRESM. The optical distortions were determined with the aid of a glass plate upon which was engraved a grid of intersecting rulings. It was then possible to make use of the optical corrections to determine accurately the



Photograph of Interaction
of 5 GeV/c π^+ meson in
the B.N.H.B.C. The Fiducial
Volume is indicated.

Figure 7

positions of the cameras relative to the chamber.

The grid plate was photographed in three positions corresponding to the inner surfaces of the front and back windows and to the centre of the chamber. These positions of the grid were aligned using a telescope arrangement and the positions of the cameras were estimated carefully. With the relative positions of grid and cameras established the coordinates of the grid intersections x_i^T, y_i^T on an ideal film plane were then calculated. The actual coordinates x_i, y_i on the photographs, were determined by accurate measurements and the effect of film stretch was removed by measuring also the camera-based fiducials printed on to the film in the camera gate. Film tilt and lens distortions were then calculated by a least squares fit to the expression.

$$\sum_{i=1}^N w ((x' - x^T)^2 + (y' - y^T)^2) = \text{minimum}$$

where $\begin{pmatrix} x \\ y \end{pmatrix}' =$

$$\begin{pmatrix} x \\ y \end{pmatrix} \left(1 + \alpha_1 \frac{x}{f} + \alpha_2 \frac{y}{f} + \alpha_3 \frac{xy}{f^2} + \alpha_4 \frac{x^2}{f^2} + \alpha_5 \frac{y^2}{f^2} + \alpha_6 \frac{(x^2 + y^2)^2}{f^4} \right)$$

Here, w is a weight and f the film-lens distance.

The general formula for fitting film tilt and spherical lens distortions would include coefficients only for x , y , r^2 and r^4 , where $r^2 = x^2 + y^2$. The coefficients α_3 , α_4 and α_5 were introduced to study the effects of non-rotational arrangement and other contributions which were not obvious. The corrections made by these coefficients, α_i , in a typical case would be about 5 microns for a track measured on the film 10 mm. from the optic axis.

Finally it was necessary to determine the camera positions relative to the chamber and for this purpose photographs were taken of the chamber fiducial crosses. The coordinates of these crosses were measured and corrected by the polynomial expression given above and the camera positions were then reconstructed. Using the camera positions thus determined and the correction expression given it has been found that points in the chamber space can be reconstructed by TARESH with a similar precision to that of the Saclay 81 cm. Bubble Chamber.

CHAPTER 2

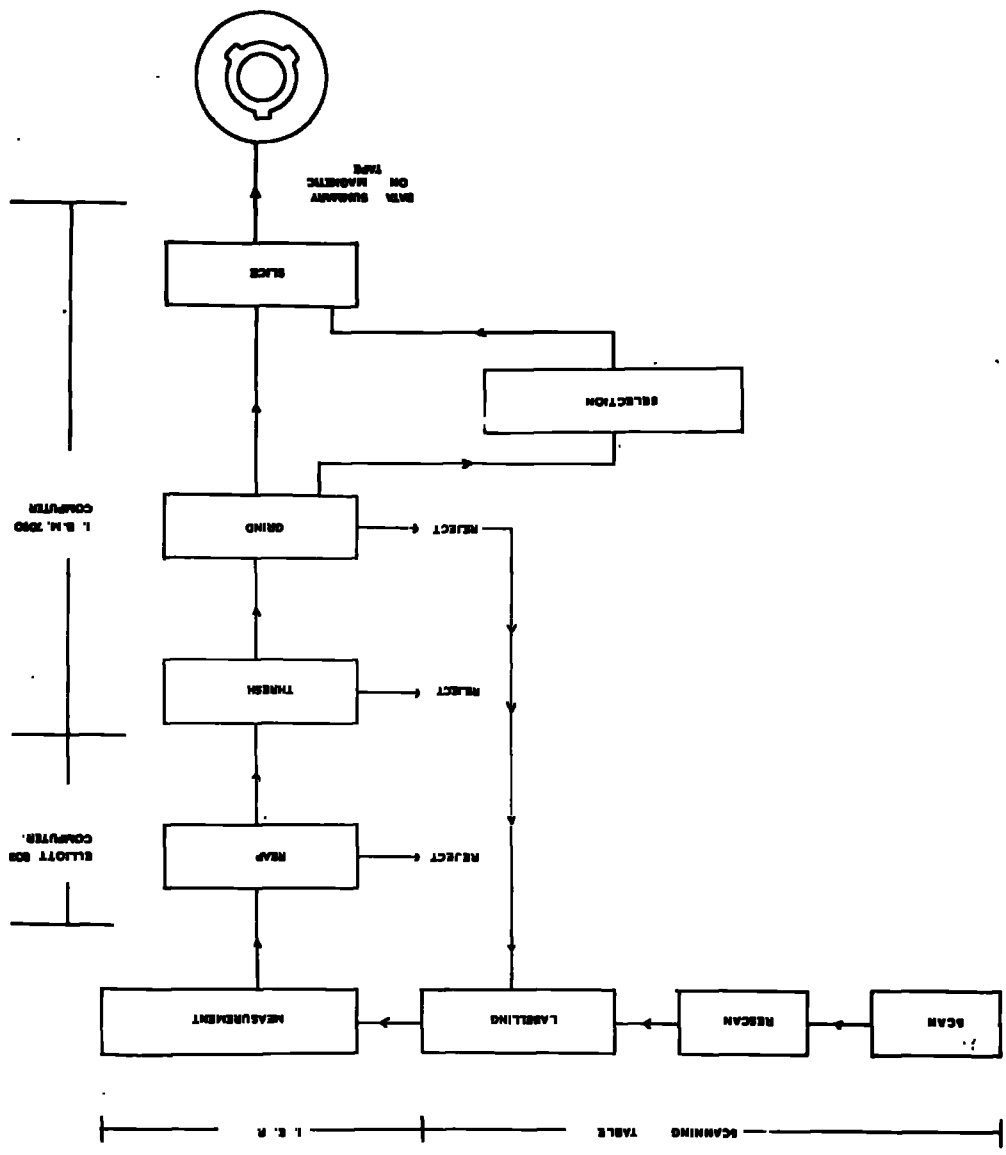
DATA REDUCTION

The system of data reduction by which events of interest were selected, measured and analysed is shown in the block diagram of figure 8.

2.1 Scanning

2.1.1 Scanning Tables

The tables upon which the film was scanned were designed in Durham and constructed in the Departmental Workshop to accommodate a Prevost projection system. To project the film on to a horizontal reflecting surface of convenient height it has been found necessary to tilt the projectors and to use a single reflection from a large cantilevered mirror which is also tilted. The lenses of 135 mm. focal length allow the projected images to be $\frac{2}{3}$ full size and by using other appropriate lenses 50 mm. and 70 mm. film may also be scanned. The table tops which serve as reflection screens are designed to be unobstructed enabling the images to be viewed from three sides if required. Generally the film is scanned



FLOW DIAGRAM OF THE ANALYSIS OF EVENTS

by viewing from the direction of the ingoing beam.

2.12 Scanning of the Hydrogen Film

One fifth of the total number of photographs of the hydrogen film were analysed at Durham, comprising of 30,000 pictures on 25 triads of film. Six of these were rejected after a brief initial scan because the picture quality on one or more of the views was bad. The reasons for the rejections were various - faintness, blurring, fogging and too many tracks in each frame. The remaining film was scanned initially for six-pronged interactions inside the chosen fiducial volume shown in figure 7. Interactions inside the volume were recorded only if the beam track entered the volume somewhere along its bottom edge. The fiducial volume was divided into six zones vertically and horizontally and on the scanning sheets were recorded both the zone of entry and the zone of interaction for each event. In addition to this the following characteristics of each interaction were recorded:

- (a) Secondary interactions
- (b) Stopping tracks and decays
- (c) Associated electron pairs and V^0 s
- (d) Identified protons

The protons were identified where possible from their curvature, estimated by comparison with calibrated curves, and by judging their bubble densities visually. It was found possible to identify protons up to a momentum of about 1.3 GeV/c.

2.13 Efficiency of Scanning

A complete re-scan of the film for six-pronged events was made and the scanning efficiencies calculated in the usual way (Burhop 1962) for the scan and re-scan of each triad. For the first scan the average efficiency for all the film was $(94.8 \pm 1.0)\%$ and for the re-scan $(95.6 \pm 0.8)\%$. The overall efficiency with which six-pronged events were found is therefore $(99.77 \pm 0.06)\%$. The assumption has been made as always that the finding of the events was a statistical process and that the same events were not missed in both the scan and re-scan. This assumption should be valid for six-pronged events since the visibility of such events is generally much better than for events of smaller multiplicities.

2.14 Scanning of the Deuterium Film

The film of the Saclay Bubble Chamber which was

studied at Durham for elastic scatterings had already been scanned and re-scanned completely at CERN as part of an investigation of four-pronged interactions in deuterium. As the results of the study of elastic scattering were of immediate interest and because at that time the scanning equipment was largely committed to the hydrogen experiment it was not possible nor thought necessary to re-scan the film in Durham. Instead the two-pronged events recorded on the CERN scanning sheets were re-examined and a selection made of those events which had the visual characteristics of elastic scatters. This procedure and the manner in which the interactions were analysed is described in section 3.5. The later comparison of the results of the analysis with those of the Ecole Polytechnique have shown that the efficiency of the CERN scanning for two-pronged events in which the recoil track is shorter than about 2 mm. is low and that re-scanning would be desirable. This has not been possible because of the deterioration of the film in handling and the experimental results have been shown with the appropriate errors.

2.2 Labelling

Before measurement the six-pronged events were 'labelled' by a physicist. For each event a sheet was prepared with the track labels for each view in the order in which they were to be measured. This preparation was undertaken mainly to save time at the measuring tables and to minimise errors which might be made by the measurer. In events with six secondary tracks it was found that frequently the relative positions of the tracks changed from view to view. Whilst these changes were easily noted at the scanning table where the labelling took place ~~where~~ and all the views could be consulted simultaneously it was much more difficult to observe them at the measuring table where only one view may be seen at a time. For interactions with smaller multiplicities the labelling was carried out by the operators as the tracks were measured.

2.3 Measurement

A standard measurement procedure was adopted as follows. For each interaction four selected fiducial crosses were measured first and then the interaction point

(apex) of the event and the tracks in counterclockwise order starting with the primary. In general, for the tracks of non-stopping particles the coordinates of six evenly spaced points along the track were measured. For some of the slower non-stopping tracks the curvature could be seen to change significantly along its length and for these care was taken to measure only that part near to the apex where the curvature was essentially constant. No allowance is made in THRESH for energy loss by the particles and therefore these tracks cannot be accurately reconstructed unless this precaution is taken. For stopping tracks of very short range only the coordinates of the end-point were measured and the momentum was then determined in the kinematics programme 'GRIND', after a mass assignment had been made, using known range-momentum data. In the case of stopping tracks with visible curvature, points were measured along their length as well as the end-point. The momentum was then determined from both the range and the curvature and the calculated values checked for compatibility. A weighted average of the two values was finally used.

2.31 Measuring Tables

The machines used for the measuring were designed in Durham and built within the department. The basis of each measuring table is a stage which moves on linear bearings and the movement of the stage is digitized in two directions using the well-known technique of counting Moiré fringes. To provide measurements with sufficient accuracy for the reconstruction and fitting of the events digitizers with a least count of two microns are used. The film is projected on to a vertical screen on which is marked a reference point of about the size of a projected track bubble. The y-motion of the stage moves the optical system and the x-motion moves the clamped film so that any point of the projected image may be brought to the reference point. This arrangement allows the stage to be of compact dimensions but there is a difference in the magnification in the two directions. THRESH takes this difference into account providing four fiducial crosses are measured. The motion of the stage is controlled through servo- and stepping motors for the course motion and the fine motion respectively. It is found that on average the settings can be reproduced to an accuracy of ± 2.5 counts.

The coordinates of the measured points are punched on to paper tape and the read-out from the counter banks to the tape punch is by way of a buffer store which enables immediate movement from one point to the next without waiting for the punching cycle to be completed. The counting and read-out system is illustrated in block diagrammatic form in figure 9. The output from the four photocells of each reading head, after being amplified and shaped, is taken to a sense detector and then to the gate control which is connected to each of the binary counters. These counters cover the range 2^0 to 2^{17} counts. A read pulse (manually operated when a coordinate is to be recorded) transfers the information from the two counter banks (x and y) to the buffer store, figure 10, by a parallel read system. Each of the binary counters has its own location in the store which is connected as a shift register with six locations per row. The upper row is connected through amplifiers to the eight-hole punch which operates on automatic trip. As each row is punched a synchronised signal returns from the punch to the store shifting each row up by one position and filling the store with 'zeros' from the bottom. After six cycles the information is completely read out and the store empty. If one of the rows of a coordinate is completely empty

MK II MEASURING and RECORDING LAYOUT

FIGURE 9

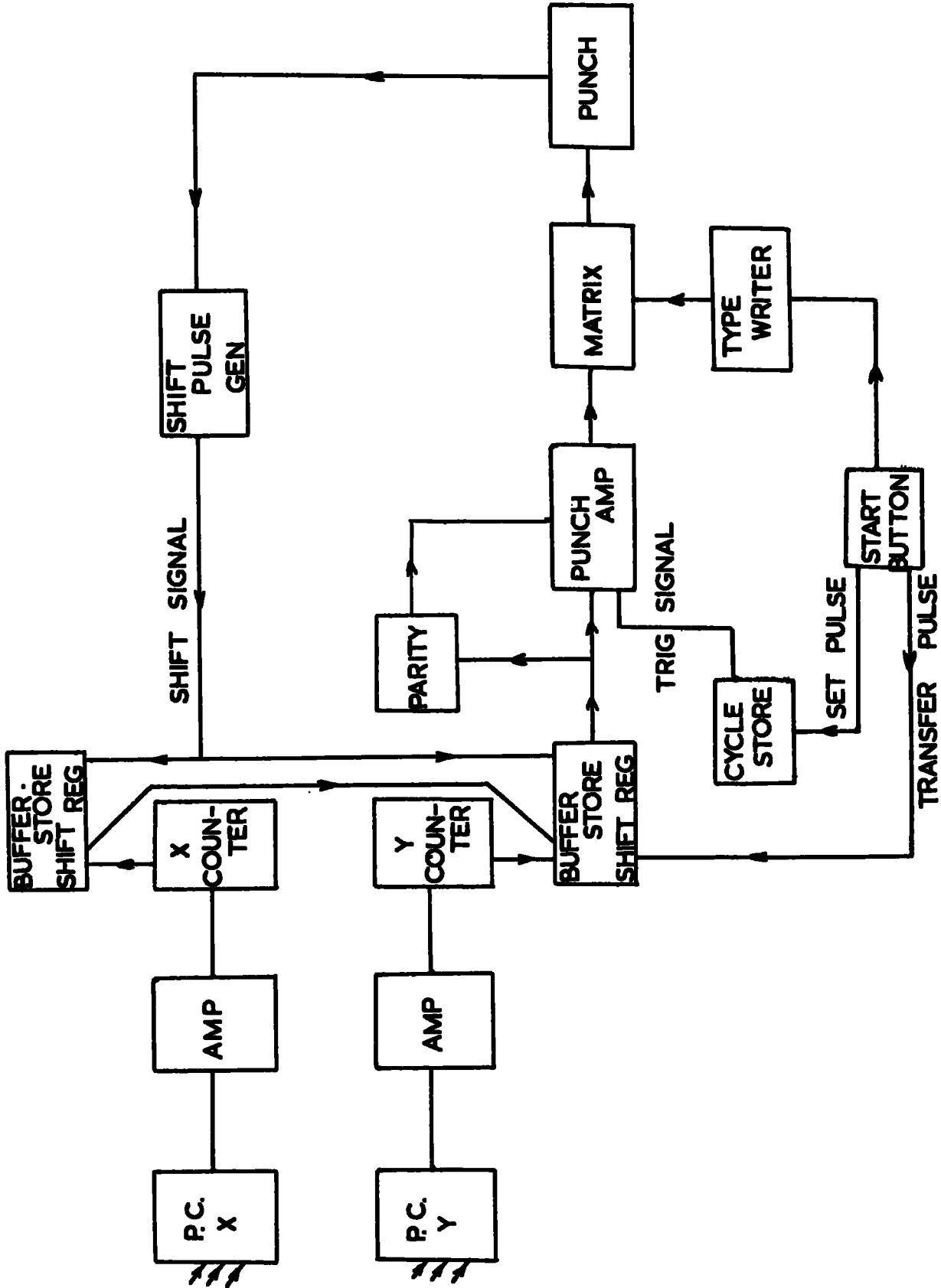
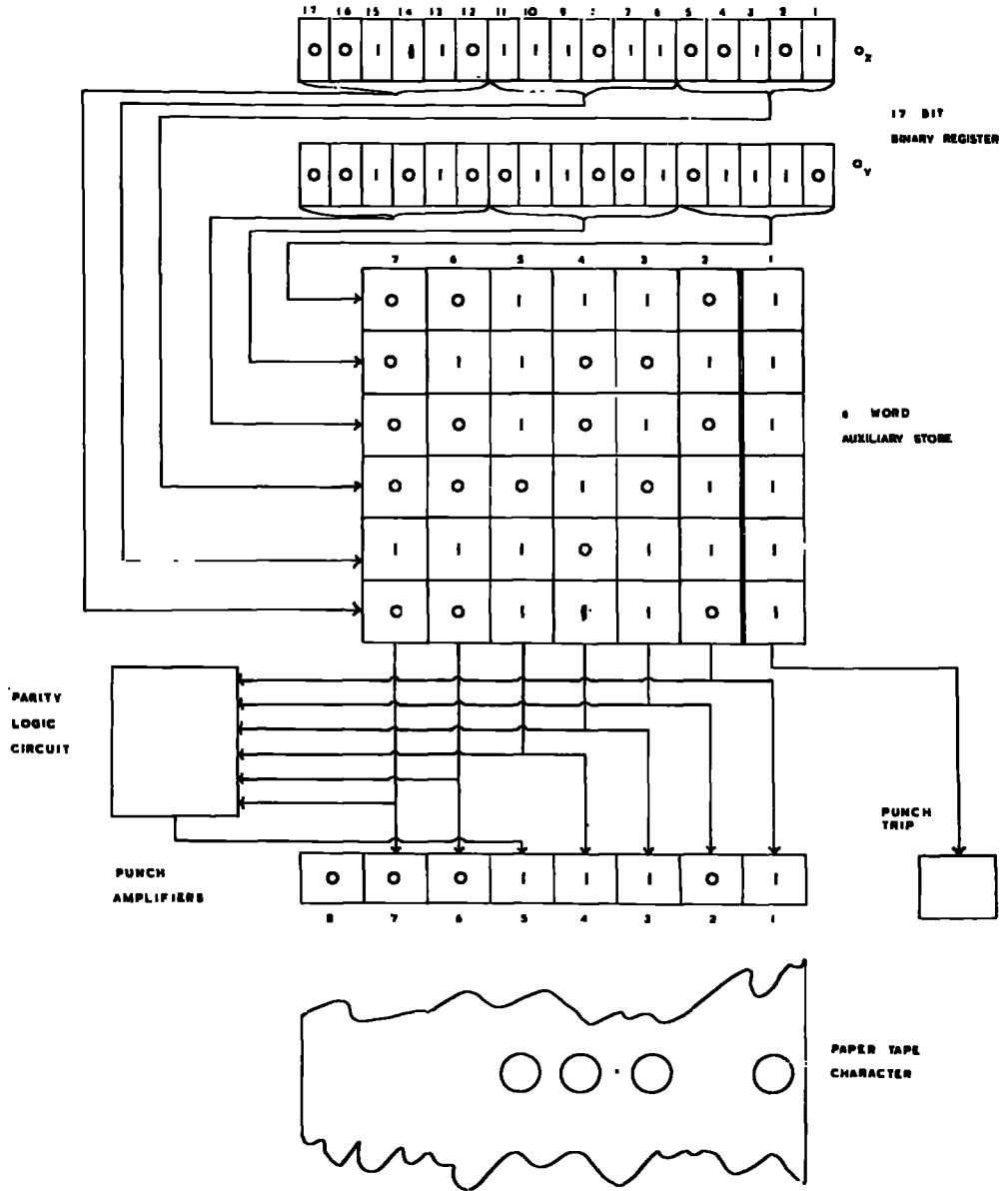


FIG. 10

SCHMATIC DIAGRAM OF CO-ORDINATE PUNCHING



(as by chance it may be) the punch is tripped by a six-row shift register connected to act as a counter. Thus each coordinate is punched on to the tape in six rows. Between the store and the punch amplifiers is an even parity generator.

Together with the measuring table is an electric input typewriter coupled to the punch by way of a diode matrix arranged in the Elliott code. All the other information needed with the coordinates is punched on to the tape using this typewriter. The read pulse is also operated by a key of the typewriter so that a complete record of the order in which each event is measured is kept on paper. The information required by the computer in addition to the coordinates includes labels for each point and track, and a 'title' for each event. This title is a series of reference numbers for a) the frame, b) the event in the frame, c) the event type, and d) the operator.

2.4 Data Processing

The output from the measuring tables was recorded using the programme 'REAP' and then put on to magnetic

tape to serve as input data for the geometry and kinematics programmes, THRESH and GRIND. These two CERN Library programmes were used by all the laboratories in both collaborations. Although these programmes are well known and widely used a brief review of their main features is given here for the purpose of later reference. The computing of the Durham six-prong events was performed using the Bonn I.B.M. 7090 computer and the deuterium two-prong events were processed on a similar computer in Paris.

2.41 REAP

In the form in which it leaves the measuring tables the data cannot be read into the geometry programme. The programme REAP, written by H. Halliwell for the particular requirements of the Durham data, both reorders the data and at the same time checks the accuracy and the completeness of the measurements. REAP is written in such a way that in reordering the data considerable latitude is allowed in the exact form the measurements take. Errors of measurement noted at the time they are made may be corrected simply by relabelling the point or track and repeating the measurement. REAP also allows a general

title, punched on to the tape with the first measured event, to serve as the title for each of the following events, with only those reference numbers altered which change from event to event. In this way usually only the frame number will need to be changed by the operator.

The output from REAP, which is run on the Durham Elliott 803 computer, consists of a paper tape in Ferranti code with the ordered THRESH input data and a second tape with information about the quality of the measurements. If insufficient fiducial marks have been measured or if they have been incorrectly measured the event is rejected. Similarly if a track has been badly measured (perhaps as a result of a counter fault) a simple fitting routine allows this to be noted and the event can usually be remeasured before the film leaves the measuring table so that considerable time can be saved.

Before entering THRESH the input data is transferred on to a magnetic tape using an I.B.M. 1401 computer and the code is changed from Ferranti to I.B.M.

2.42 THRESH

THRESH is the mass-independent geometrical reconstruction programme and the version used for these experiments was written in the Fortran II language. Using some

general information about the bubble chamber used e.g. the positions of the cameras and fiducial crosses and data concerning the optical system, the measurements of each event are used to calculate the curvature (or range) and the direction in the chamber of each track and also the coordinates of all interaction points. The output lists the angles of dip and azimuth at the starting point of the track and the curvature at its middle. For each of these quantities the error is calculated from the difference between the measured and the fitted points. This is the 'internal' error of each quantity.

2.43 GRIND

The kinematics programme GRIND tests the various hypotheses for the interpretation of each interaction. For each experiment the possible exit channels of an interaction are assembled in a 'title' to the programme and these indicate the mass assignments that may be made to the tracks. The other GRIND titles contain data concerning the magnetic field, the range-momentum relations and the 'external' errors.

Besides enabling the different hypotheses to be distinguished GRIND also provides the best estimate of the

complete kinematical state of each particle (given by its four-momentum) after the correct fitting has been made. These values are then used in later analysis. The relativistic conservation laws are imposed upon the interactions by four constraint equations - one for each component of four-momentum. The masses of the particles are fixed by the hypothesis and all the measured quantities are adjusted within prescribed limits until the best fit to the constraint equations is found. The fit is made by the minimisation of a χ^2 function which depends on all the measured quantities. In the case where there are no unmeasured variables the fit has to fulfil all the constraint equations and there are four degrees of freedom. Where there are unmeasured variables, such as the momentum and direction of a neutral particle, some of the equations must be used to calculate these variables and in the case of one neutral particle three of the equations are automatically fulfilled leaving only one degree of freedom for the fit. No fit at all can be obtained when there is more than one neutral particle produced in an interaction unless the decay products can be measured. In such cases only the missing mass can be calculated for the interaction. For any one interaction the number of fits is not necessarily limited to one. The actual number will depend

largely on the particular kinematics of the event and upon the amount of adjustment which is allowed.

The output of GRIND contains a geometry record of the complete unfitted event and for each hypothesis a record of the assigned masses and the corresponding value of χ^2 . For each hypothesis, whether fitted or not, GRIND also calculates the squared missing mass using the unfitted quantities. The relative ionizations of the tracks are determined as seen on the central view from the $1/\beta^2$ dependence and these are corrected for dip. Certain tests are applied during the fitting which if not satisfied are indicated as errors in the printed output. For example, the expected 'external' errors which are defined by certain formulae, are compared with the internal errors computed by THRESH for the curvature and the angles of each track. If the internal error is greater than three times the external error then the correspond^{ing} error is signalled.

2.5 Examination and Analysis

Each six-pronged interaction was studied at the scanning table together with the output from GRIND and a

visual comparison was made between the computed bubble densities of the tracks and those seen on the film. All hypotheses which were not consistent with the ionization of the tracks were excluded. Hypotheses with strange particles were not written in to the GRIND title so it was necessary to identify the proton only to distinguish between hypotheses. Protons can be distinguished from pions up to a momentum of about 1.3 GeV/c when the proton ionization is close to the plateau level. For events where more than one hypothesis satisfied the above examination the values of the squared missing mass, m_{MM}^2 , and of χ^2 were considered to choose the more probable interpretation. The necessary condition for the calculated m_{MM}^2 to be acceptable for a hypothesis was that

$$m_{MM}^2 - 2\Delta(m_{MM}^2) < M_0^2 < m_{MM}^2 + 2\Delta(m_{MM}^2)$$

where M_0 was the mass of the missing particle corresponding to the hypothesis e.g. $M_0 = 0$ for 4C fits. The greatest acceptable value for χ^2 was 6 for the 1C fits and 24.5 for the 4C fits. Where two or more hypotheses still remained the following order of precedence was observed. Four-constraint hypotheses were accepted rather than 1C fits and where further distinction was required the

hypothesis with the lowest value of χ^2 was chosen.

Some events which had not been sufficiently well measured failed to be reconstructed in THRESH and these were picked out from the GRIND printout for remeasurement. Certain other events which had produced fits in GRIND were also remeasured if the errors signalled as a result of the GRIND tests were sufficiently important to cast doubts on the validity of the fit obtained. If, for example, an event had one track too badly measured to be reconstructed a 1C fit might nevertheless be made which could be satisfactory in every other way and in such a case the error signalled would ensure that it was re-measured.

2.51 χ^2 Limits

The χ^2 limits used for the π^+p experiment were the ones that had been found previously to be adequate in distinguishing between the following interactions of one and no degrees of freedom

$$p\bar{p} \rightarrow \pi^+ \pi^+ \pi^- \pi^- \pi^0$$

$$\rightarrow \pi^+ \pi^+ \pi^- \pi^- \pi^0 \pi^0$$

Events of these two types were generated by a Monte Carlo programme 'FAKE' with errors of the variables similar to those found in experimental values. These simulated events were then used as input for GRIND and a study of the resulting fitted hypotheses and associated χ^2 values indicated the extent to which misclassification of events might be expected. It was found that selecting a value of $\chi^2 \leq 6$ for the 1C fits gave a confidence level of 0.01 and this has been adopted for the 1C fits of the six-pronged π^+p interactions also. For the 4C fits a value of $\chi^2 \leq 24.5$ was thought to be adequate and corresponds to a confidence level of 0.0001.

2.52 Data Summary Tape

From the GRIND output a summary tape was prepared which contained only the hypotheses selected by the examination. For each event GRIND produced a 'SLICE' card and upon this was punched the number corresponding to the selected hypothesis. Using these cards the programme SLICE compiled the Data Summary Tape (D.S.T.). This tape held the records of the unfitted and fitted geometry, MM^2 and χ^2 for each event. As the experiment

progressed and more events were fitted the D.S.T. was kept up to date.

2.53 SUMX

The CERN Library programme 'SUMX' was used to calculate the differential cross sections ($d\sigma/d\Delta^2$) and the effective mass and angular distributions from the D.S.T. By adding the appropriate subroutines SUMX may be used to plot any distribution relevant to the experiment. The distributions may be plotted with any 'cuts' needed to study particular features of the interactions by requiring that certain tests be satisfied.

2.6 Phase Space

The distributions prepared by SUMX from the experimental results are presented later and are often compared to the distributions predicted by statistical factors only - usually called 'phase space'. The density of n particles in Lorentz invariant phase space is given by the integral which is defined thus

$$R_n(E, \bar{p}_1, \dots, \bar{p}_n) = \int \prod_1^n \frac{d^3 \bar{p}_i}{2E_i} \delta^3(\sum_1^n \bar{p}_i - \bar{P}) \delta(\sum_1^n E_i - E)$$

where \bar{p}_i are the momenta and E_i the energies of the particles in the centre of mass system of total energy E and total momentum \bar{P} .

For any particular final state R_n is calculated using the programme FOWL which generates events by a Monte Carlo method. The programme has been used chiefly to calculate the phase space distribution of effective mass for all the different combinations of particles possible in the six-pronged interactions. When the distributions are calculated for many thousands of events the results agree well with the curves produced analytically. The weight with which each generated event is plotted is given by the phase space integral and the total weight is normalised to one. To take into account postulated resonances in the final state a Breit Wigner function is introduced to increase the weight of those events for which the effective mass of the particles of the function lies within the width of the resonance.

CHAPTER 3

ELASTIC SCATTERING OF π^+ MESONS IN DEUTERIUM AT 5 GEV/C

3.1 Introduction

The analysis of elastic scattering of pions and protons on nuclei is usually made with the optical model which describes very well in terms of a Bessel function the characteristic diffraction phenomena observed experimentally. Bellettini et al. (1966) at CERN have studied the elastic scattering of protons on nuclei ranging from Li to U and have made such an analysis with an optical model which additionally takes into account the Coulomb interaction. For the heavier nuclei the agreement is very good and evidence for the secondary maxima can be seen; for the lighter nuclei these secondary maxima become masked because the structure of the nucleus, with diffraction from individual nucleons, is then important. In the case of the heavy nuclei the optical analogy works very well because the partial waves are strongly absorbed up to a clearly defined maximum value. This maximum is given by $l_{\max} = kR$, where k is the reduced wave number of the incident particle, and defines the radius of the nucleus R .

In an approximation usually made for the Bessel function at small angles the differential cross section, $d\sigma/dt$, has a simple exponential dependence upon t , the negative square of the four momentum transfer. Using nuclear emulsions Kirillova et al. (1964) have made a study of proton-deuterium elastic scattering and have examined the dependence of $d\sigma/dt$ upon t . They have shown that their results are in fact fitted by the relation

$$d\sigma/dt = (d\sigma/dt)_{t=0} \exp(bt+ct^2)$$

where $(d\sigma/dt)_{t=0} = \pi R^4/4h^2$

The differential cross section has an energy dependence which reflects the well-known 'shrinking' of the diffraction peak for nucleon-nucleon scattering. It is unlikely that the simple optical model for a uniform nuclear potential can be used to describe the deuterium nucleus which has a very small binding energy and consequently diffuse structure. In the analysis of the present experiment, therefore, an attempt has been made to introduce more realistic nuclear potentials into the optical model calculations, based on the Hulthen wave function and an approximation to a 'hard core' wave function.

It has been shown by Fernbach, Green and Watson (1951) and others that the elastic scattering in deuterium may be described in terms of the free neutron and proton scattering amplitudes, $f(\pi^+p)$ and $f(\pi^-p)$ respectively. In the case of π^+d interactions these are both known -- $f(\pi^+p)$ from direct measurements and $f(\pi^+n)$ from the measurements of $f(\pi^-p)$. Quasi-elastic scattering, in which the deuteron breaks up, may also be considered from the same point of view and Harrington (1964), taking into account double scattering effects, has derived expressions for the differential cross sections for both elastic and quasi-elastic scattering. Bellettini et al. (1965) in their p-d scattering experiment at 19.3 GeV/c have analysed their results using these expressions and obtain good agreement for the assumption that both the real and imaginary parts of the p-p and p-n scattering amplitudes are identical. They have at the same time extended the analysis to the results of Kirillova et al. for p-d scattering at 10.9 GeV/c and again have found good agreement. The results of the present experiment have also been studied in this way to try to confirm that the analysis holds for the scattering of pions as well in the lower energy region, namely 5 GeV/c.

3.11 Techniques for Studying Elastic Scattering in Deuterium

The spark chamber and nuclear emulsion techniques have been used most often to study elastic scattering in deuterium. In both cases only one of the particles taking part in the interaction is observed. In counter experiments only the scattered particle is measured and this is performed with extremely good angular resolution, about 0.1 mrad. The momentum resolution, however, although about $1/2\%$ at 19 GeV/c, does not allow the elastic interactions to be separated from the quasi-elastic interactions by means of the kinematical constraints between angle and momentum. At present this represents a limitation when studying deuterium scattering with this technique but with improved momentum resolution and the very large statistics obtained by spark chambers very accurate measurements of elastic cross sections will be possible.

In the emulsion experiments performed at Dubna the proton beam is incident on a thin foil target loaded with a heavy hydrocarbon and the recoil deuterons, which are emitted at almost 90° , are detected with nuclear emulsions placed a short distance away. Very accurate measurements

of the momenta and angles of the deuteron tracks enables the elastic and quasi-elastic interactions to be distinguished. Momentum transfers down to $-t \approx 0.005 \text{ (GeV)}^2$ may be studied in this way. Experiments on the elastic scattering of pions are more difficult to perform because of the need for very intense, pure and well collimated pion beams which are not available as readily as similar proton beams.

In bubble chamber experiments at high energy the angles through which the incident particles are elastically scattered are too small to be easily detected at the scanning table. The recoiling target nuclei, however, are more readily visible and it is by scanning for these characteristic 'black' tracks that elastic scatterings may be selected. It is not possible to separate the quasi-elastic scattering visually nor simply by the fitting of GRIND. The elastic sample is selected by requiring certain tests to be satisfied which are imposed by the constraints of the interaction. The range of momentum transfers which can be covered by the bubble chamber technique is not as great as can be obtained using counters or emulsions because deuteron tracks of range less than 1 mm. are not seen whilst scanning. Thus the smallest transfer which can

be resolved is $-t = 0.015 \text{ (GeV)}^2$ which corresponds at 6 Gev/c to an angle of scattering of about 20 mrad. For this reason the bubble chamber would not be useful to study the real part of the scattering amplitude by observation of the interference between this part and the Coulomb amplitude (essentially real) which is important only at small angles. However, to study elastic scattering at very small impact parameters, bubble chambers would be more suitable for observing and measuring the long recoils than nuclear emulsions where long tracks would have to be followed through the emulsion stack.

3.2 The Optical model

In the optical model a particle scattered by a nucleus is treated as a wave propagating through an attenuating medium having a refractive index. In this case where absorptive effects are considered the interaction potential will be complex. The elastic effects, the refraction inside the nucleus and the diffraction around the nucleus (which is considered to be spherical), are described by the real part of the potential, V_r . Because the thin nuclear surface is considered to be diffuse

reflection may be neglected. The refraction increases the wave number of the incident particle from k to k' inside the potential and in the relativistic case (Fowler and Perkins, 1958)

$$k' = k(1 + (2V_r/p\beta c) + (V_r/pc)^2)^{1/2}$$

where p is the centre of mass momentum of the incident particle. Then if pc is large in comparison with V_r the change in wave number k_1 is given by

$$k_1 = kV_r/p\beta c \quad (1)$$

The attenuation inside the nucleus by the inelastic channels is described by the imaginary part of the potential, V_i , which is therefore related to the coefficient of absorption, K . This coefficient is defined by the product of the nucleon density and the average cross section for scattering of the particle by a nucleon, and is related to V_i in the following way

$$K = 2V_i/\hbar\beta c \quad (2)$$

The refracted wave front re-emerges from the nucleus with smaller amplitude and is out of phase with the wave diffracted around the nucleus. The resulting interference

pattern may be described by Bessel functions. Fernbach et al. (1949) have shown that the scattering amplitude, $f(\theta)$, may be written as follows

$$f(\theta) = ik \int_0^R (1 - e^{(2ik_1 - K)s}) J_0(k\rho \sin\theta) \rho d\rho \quad (3)$$

where J_0 is the zero order Bessel function, $2s$ the distance across the nucleus at distance ρ from the centre, and θ is the angle of scattering. The differential cross section is given by

$$d\sigma/d\Omega = |f(\theta)|^2$$

In large nuclei the wave passing through the nucleus is almost wholly absorbed. The elastic scattering is then essentially diffractive only and the following approximation is usually made.

$$d\sigma/d\Omega = \frac{k^2 R^4}{4} \left[\frac{2J_1(kR \sin\theta)}{kR \sin\theta} \right]^2$$

For small angles of scattering this may be further simplified and written in terms of $-t$, the four-momentum transfer squared, becomes

$$d\sigma/dt = \frac{\pi R^4}{4h^2} \exp\left[-(R/2h)^2 |t|\right]$$

This expression is valid only inside the first minimum of the diffraction pattern.

It may also be shown (e.g. Lock, 1960) that the imaginary part of the forward scattering amplitude is related to the sum of the elastic and inelastic cross sections, the total cross section σ_T , in the following way

$$\text{Im}f(0) = \frac{k\sigma_T}{4\pi} \quad (4)$$

This relationship is known as the optical theorem.

In the optical model the potential inside the nucleus is generally taken to be constant but in the calculations presented later the structure of the deuteron nucleus has been taken into account by considering both the real and the imaginary components of the potential to be dependent upon the nucleon density. An alternative approach to the problem of scattering on deuterium, the model based on the impulse approximation, considers the nucleons separately and allowance^{is} made for diffuseness of the deuteron by the inclusion of a strong interaction form factor.

3.3 High Energy Scattering in the Impulse Approximation

The problem of high energy collisions of particles

with deuterium has been treated in detail by Harrington and by Franco and Glauber (1965) whose work is closely followed in this discussion. In the approximation used the two nucleons are considered to be stationary during the interaction which takes place on the mass shell. Both single and double scatterings are taken into account and the deuteron elastic scattering amplitude is expressed in terms of the elastic scattering amplitudes of the proton and neutron and of the deuteron form factor.

High energy scattering takes place predominantly at small angles and so double scattering may occur with appreciable intensity but scattering of higher orders will require one or more backward scatterings and is therefore of negligibly small amplitude. At the high energies considered the wavelength of the incident particle will be much smaller than the range of its interaction with a nucleon and diffraction theory may be used to describe the collision.

A general expression may be written to describe the two-particle elastic scattering amplitude at small angles

$$f(\bar{k}', \bar{k}) = \frac{ik}{2\pi} \int \exp [i(\bar{K} - \bar{k}') \cdot \bar{b}] (1 - \exp(i\chi(\bar{b}))) d\bar{b} \quad (5)$$

where \bar{k} and \bar{k}' are the propagation vectors of the particle before and after deflection, and \bar{b} is the impact parameter vector perpendicular to the direction of the incident particle. The scattering process is characterised by the function $\chi(\bar{b})$ which represents the change in phase at a point \bar{b} of the emerging wave front resulting from its passage through the interaction region. Absorption of the wave as a result of incoherent processes is represented here again by allowing $\chi(\bar{b})$ to take complex values. Since the Lorentz transformation does not affect the transverse components of the momentum nor the phase shifts, equation 5, is also the correct representation for the scattering amplitude in the laboratory system when the laboratory values of \bar{k} and \bar{k}' are used.

The internal ground state wave function of the deuteron is $\Psi_i(\bar{r})$ and $\Psi_f(\bar{r})$ is the internal final state wave function where \bar{r} is the vector separation of the proton and neutron whose coordinates are \bar{r}_p and \bar{r}_n . In the case of elastic scattering the final state will be the ground state again. The amplitude for the process in which the deuteron is left in a final state $|f\rangle$ and in which the incident particle transfers momentum $\hbar\bar{q} = \hbar(\bar{k} - \bar{k}')$

may be written as

$$F_{fi}(\bar{q}) = \frac{ik}{2\pi} \int \exp(i\bar{q} \cdot \bar{b}) \langle f | \Gamma_{\text{tot}}(\bar{b}, \bar{r}_p, \bar{r}_n) | i \rangle d\bar{b} \quad (6)$$

where the abbreviation has been introduced

$$\Gamma_{\text{total}}(\bar{b}, \bar{r}_p, \bar{r}_n) = 1 - \exp[i\chi_{\text{total}}(\bar{b}, \bar{r}_p, \bar{r}_n)]$$

The total phase shift depends upon the coordinates \bar{r}_p and \bar{r}_n as well as \bar{b} .

Since in the processes considered the momentum transfer is small the recoil of the nucleus may be neglected without introducing any significant error. The centre of mass of the target nucleus is considered to remain fixed at the origin and Eq. 6 may be rewritten as

$$F_{fi}(\bar{q}) = \quad (7)$$

$$\frac{ik}{2\pi} \int \exp(i\bar{q} \cdot \bar{b}) d\bar{b} \int \psi_f^*(\bar{r}) [1 - \exp\{i\chi_n(\bar{b} - \frac{1}{2}\bar{s}) + i\chi_p(\bar{b} + \frac{1}{2}\bar{s})\}] \psi_i(\bar{r}) d\bar{r}$$

Here, \bar{s} is the projection of \bar{r} on the plane perpendicular to the direction of incidence and $\chi_n(\bar{b} - \frac{1}{2}\bar{s})$ and $\chi_p(\bar{b} + \frac{1}{2}\bar{s})$ are the phase shifts produced by the neutron and proton

in their instantaneous positions.

To assist in separating the individual scattering contributions Γ_p and Γ_n are introduced for the proton and neutron respectively. These obey the relation

$$1 - \exp \left[i\chi_n(\bar{b} - \frac{1}{2}\bar{s}) + i\chi_p(\bar{b} + \frac{1}{2}\bar{s}) \right] =$$

$$\Gamma_n(\bar{b} - \frac{1}{2}\bar{s}) + \Gamma_p(\bar{b} + \frac{1}{2}\bar{s}) - \Gamma_n(\bar{b} - \frac{1}{2}\bar{s}) \Gamma_p(\bar{b} + \frac{1}{2}\bar{s}) \quad (8)$$

From Eq. (5) it can be seen that the nucleon scattering amplitude is a Fourier transform of Γ and an approximate inversion is made by multiplying this equation by $\exp(-i\bar{q} \cdot \bar{b})$ and integrating the variable \bar{q} over a plane perpendicular to the direction of incidence. Then

$$\Gamma(\bar{b}) = \frac{1}{2\pi i k} \int \exp(-i\bar{q} \cdot \bar{b}) f(\bar{q}) d\bar{q}$$

Substituting the identity (8) into the integral (7)

$$F_{fi}(\bar{q}) = \langle f | \exp(\frac{1}{2}i\bar{q} \cdot \bar{s}) \frac{ik}{2\pi} \int \exp(i\bar{q} \cdot \bar{b}) \Gamma_n(\bar{b}) d\bar{b}$$

$$+ \exp(-\frac{1}{2}i\bar{q} \cdot \bar{s}) \frac{ik}{2\pi} \int \exp(i\bar{q} \cdot \bar{b}) \Gamma_p(\bar{b}) d\bar{b}$$

$$- \frac{ik}{2\pi} \int \exp(i\bar{q} \cdot \bar{b}) \Gamma_n(\bar{b} - \frac{1}{2}\bar{s}) \Gamma_p(\bar{b} + \frac{1}{2}\bar{s}) d\bar{b} | i \rangle$$

The first two integrals are easily expressed in terms of the neutron and proton elastic scattering amplitudes by means of Eq. 5. In the third integral Γ_n and Γ_p are expressed in terms of f_n and f_p and making use of the Fourier integral representation of the two dimensional delta function it is found that

$$F_{fi}(\bar{q}) = \langle f | F(\bar{q}, \bar{s}) | i \rangle$$

$$\begin{aligned} \text{where } F(\bar{q}, \bar{s}) &= \exp(\frac{1}{2}i\bar{q} \cdot \bar{s})f_n(\bar{q}) + \exp(-\frac{1}{2}i\bar{q} \cdot \bar{s})f_p(\bar{q}) \\ &+ \frac{i}{2\pi k} \int \exp(i\bar{q}' \cdot \bar{s})f_n(\bar{q}' + \frac{1}{2}\bar{q})f_p(-\bar{q}' + \frac{1}{2}\bar{q})d\bar{q}' \end{aligned}$$

The effects of single and double scattering have been separated in this expression. The first two terms are the single scattering amplitudes for the proton and neutron and the third term represents the double scattering amplitude. The form factor of the deuteron in the ground state is

$$S(\bar{q}) = \int \exp(i\bar{q} \cdot \bar{r}) |\psi(\bar{r})|^2 d\bar{r}$$

and this expression is used to rewrite the elastic

scattering amplitude in the form

$$F_{ii}(\bar{q}) = S(\frac{1}{2}\bar{q})f_n(\bar{q}) + S(-\frac{1}{2}\bar{q})f_p(\bar{q}) + \frac{i}{2\pi k} \int S(\bar{q}')f_n(\frac{1}{2}\bar{q}-\bar{q}')f_p(\frac{1}{2}\bar{q}+\bar{q}')d\bar{q}'$$

This is the diagonal element of $F(\bar{q}, \bar{s})$ in the deuteron ground state and by squaring the modulus of the matrix element the angular distribution of the elastically scattered intensity may be obtained

$$\begin{aligned} (d\sigma/d\Omega)_{\text{elastic}} &= |F_{ii}(\bar{q})|^2 \\ d\sigma/d\Omega_{\text{el}} &= S^2(\frac{1}{2}\bar{q})\{ |f_n(\bar{q})|^2 + |f_p(\bar{q})|^2 + 2\text{Re}[f_n(\bar{q})f_p(\bar{q})] \} \\ &\quad - \frac{1}{\pi k} S(\frac{1}{2}\bar{q})\text{Im} \left\{ [f_n(\bar{q}) + f_p(\bar{q})] \int S(\bar{q}')f_n(\frac{1}{2}\bar{q}+\bar{q}')f_p(\frac{1}{2}\bar{q}-\bar{q}')d\bar{q}' \right\} \\ &\quad + \frac{1}{(2\pi k)^2} \left| \int S(\bar{q}')f_n(\frac{1}{2}\bar{q}+\bar{q}')f_p(\frac{1}{2}\bar{q}-\bar{q}')d\bar{q}' \right|^2 \end{aligned}$$

The three terms above each have a straightforward physical significance. The first term contains the intensities for scattering by the neutron and the proton and the interference of the two wave amplitudes. The second term corresponds to the interference between the double scattering

amplitude and the two single scattering amplitudes. Since the form factor is peaked sharply in the forward direction this term has an appreciable contribution only if in the double scattering process the scattering by one of the particles occurs with a momentum transfer very close to \bar{q} and the additional scattering by the other nucleon occurs with nearly zero momentum transfer. The third gives the intensity for pure double scattering.

To derive the form factor, $S(\frac{1}{2}\bar{q})$, for the above expression two different wave functions have been used, described below. These wave functions have also been employed to describe the structure of the deuteron in the optical model calculations.

3.4 The Deuteron Wave Function

If an attractive central force of short range is assumed between the proton and neutron a potential, which must be negative, may be derived having a value different from zero only within the range of the force. The ground state of the deuteron would then be a singlet state, being spherically symmetric, and the radial wave function $u(r)$, ($=r\psi(r)$), would be dependent only on the absolute value of the separation r . For large values of r the

radial wave function is then given by

$$u(r) = e^{-r/\rho}$$

where $\rho = k^{-1} = \hbar(2\mu B)^{-\frac{1}{2}} = 4.31$ fermi,

k being the wave number, μ the reduced mass of a nucleon and B the binding energy of the nucleus. From the value of the 'decay length' ρ which is considerably larger than the range of the force between the nucleons (about 2 fermi) it may be seen that the deuteron has a very diffuse structure.

From measurements of the deuteron quadrupole magnetic moment it is known that there is, besides the S state, a D state probability of about 3%. This gives rise to a spin-orbit interaction so that in addition to the central force there is a tensor force also. Gartenhaus (1955), taking into account the two states, has studied the interaction potential using the Yukawa theory with cut-off. The resulting potential at large separations (>1 fermi) is similar to the potential with no cut-off. At small distances however, the tensor potential is close to zero and the central potential is strongly repulsive. The corresponding

wave function, which is given in numerical form, describes a deuteron with a 'hard core'. The proton and neutron cannot then overlap as would be the case without cut-off. The binding energy and quadrupole moment which may be calculated with this theory are in good agreement with experiment. Moravcsik (1958) has approximated the Gartenhaus wave function by several analytical expressions and two of these have been used in the present calculations. The first is a Hulthen type wave function which has the form

$$u(r) = C (e^{-\alpha r} - e^{-\beta r})$$

Agreement with the asymptotic behaviour of the Gartenhaus S function determines the value of C and α ($\approx 1/\rho$) and β is given by the normalisation. The D-wave function contributes only 7% to the total normalisation and we have neglected this. The resulting approximation to the whole wave function is

$$u(r) = C (e^{-0.232r} - e^{-1.202r}) \quad (10)$$

This wave function does not give good agreement at small separations and cannot be thought to resemble a 'hard core' description of the deuteron. A much better

approximation to the hard core is given by a second function which, however, retains a simple analytical form

$$u(r) = K (1 - e^{-1.59r})(e^{-0.232r} - e^{-1.59r}) \quad (11)$$

We have used this approximation as our hard wave function. The two wave functions are shown in comparison with the Gartenhaus S-wave function in figure 11.

3.5 Experimental Analysis

From the two-pronged events found in the scan at CERN about 1,250 events were selected from 31 triads of film for measurement as candidates for the elastic interaction $\pi d \rightarrow \pi d$. At the Ecole Polytechnique a further 1550 events, selected from 38 triads, were measured. As explained previously the elastic scatters have a characteristic appearance, namely a track of minimum ionisation in the forward direction and a 'black' recoil track. For momentum transfers typical of elastic interactions and for events inside the fiducial volume, the recoil stops inside the chamber. The contamination in the sample selected by scanning is largely made up of quasi-elastic interactions in which the deuteron nucleus breaks up, and the proton

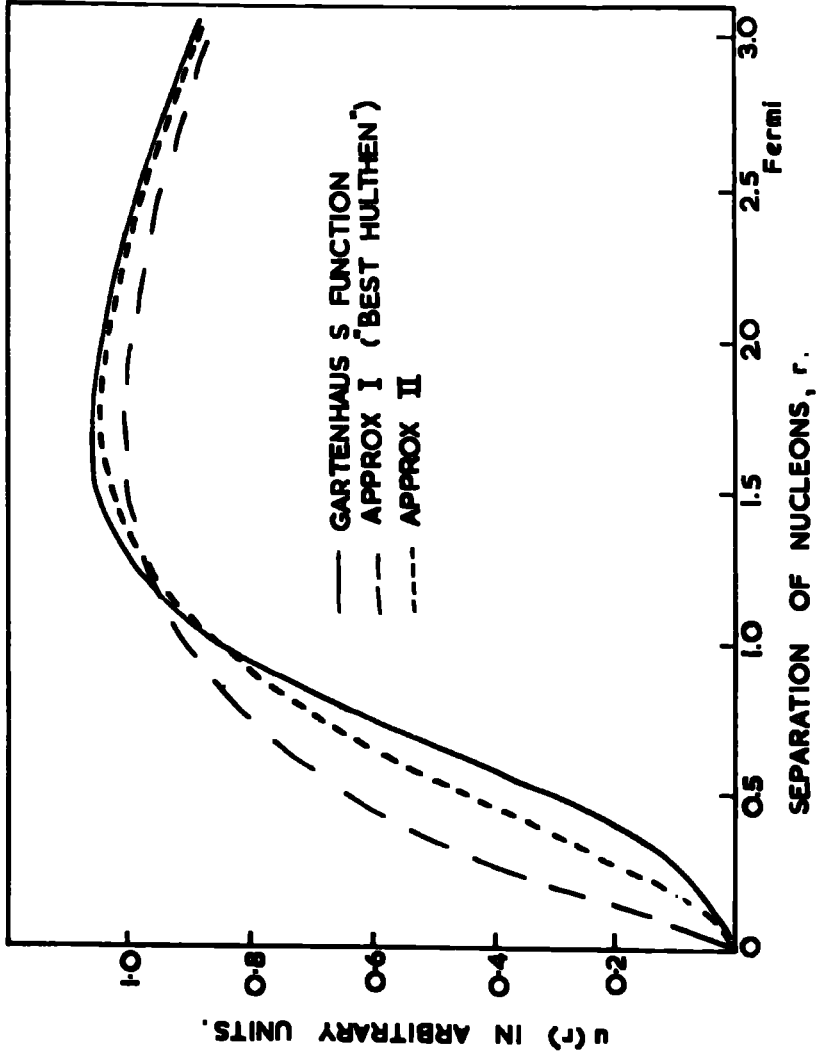


FIG. 11 GARTENHAUS S WAVE FUNCTION WITH
 HULTHÉN WAVE FUNCTION AND APPROXIMATE
 HARD CORE WAVE FUNCTION.

stops in the chamber. In these cases the interaction may take place on the neutron when the proton acts as a 'spectator', or it may take place with the deuteron as a whole and raise its internal energy so that it subsequently breaks up. Since the deuteron is a loosely bound nucleus the impact of a high energy particle may be expected to produce many events of this kind.

Whilst events of the above types cannot be separated visually it is possible to exclude nearly all inelastic events from selection by adopting certain acceptance criteria. It was required that the selected interactions, besides having a stopping recoil track, should also be characterised by a secondary pion with momentum greater than 4 GeV/c, an angular deviation of less than 6° (which allowed momentum transfers up to about 0.6 GeV/c) and a transverse momentum opposite to that of the recoil. There were no other restrictions. The momentum of the secondary pion was estimated at the scanning table using sets of calibrated curves.

After measurement in Durham and Paris the events were analysed by the Paris versions of THRESH and GRIND on the Saclay I.B.M. 7090 computer. The events were fitted to the following hypotheses

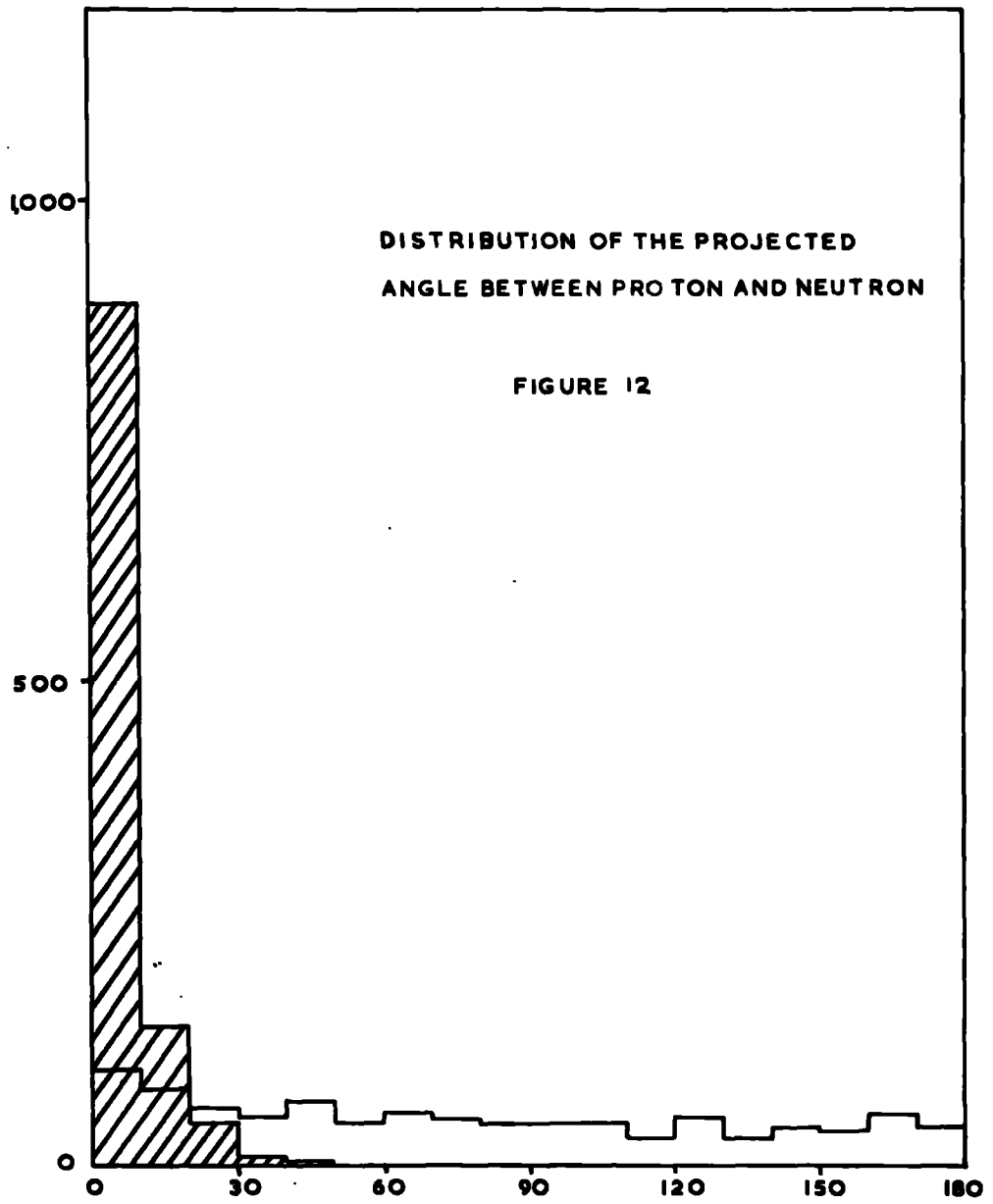
$$\pi^+ d \rightarrow \pi^+ d \quad (i)$$

$$\rightarrow \pi^+ p n \quad (ii)$$

$$\rightarrow \pi^+ d \pi^0 \quad (iii)$$

All fits to the LC inelastic hypothesis (iii) were rejected from further analysis. This did not introduce any bias into the sample of elastic events finally selected because ambiguous fits were obtained in a few cases only between hypotheses (iii) and (ii). It was found, however, that nearly all of the events which make a 4C fit for the elastic scattering hypothesis (i) were also able to fit the LC hypothesis (ii) for quasi-elastic scattering. Thus of the events analysed by GRIND a total of about 2100 interactions from both laboratories gave fits to the LC hypothesis (ii) and of these about 1200 events also fitted the elastic scattering hypothesis (i). That some of the events can be fitted by both hypotheses is mainly a result of the comparatively large errors which are made in the measurement of very energetic and very 'slow' particle tracks. When GRIND tries to fit a recoil deuteron as a proton it is able to adjust the angle and

momentum of the neutron until a reasonable fit is made as the limits of adjustment are rather wide. In general, for a fit made in this way, the angle which the fitted neutron makes to the direction of the recoil should be very small because the deuteron binding energy is very low and the deuteron can therefore be approximated by a proton and neutron moving in the same direction. For quasi-elastic interactions in which the recoil is genuinely a proton the fitted neutron is expected to be distributed isotropically. Two tests have been made to confirm that the 4C hypothesis is the correct interpretation of those events which also give 1C fits. The first test is based on the expectation that if the recoil is really a deuteron then the angle between the fitted proton and neutron should be close to zero. In fact the projected angle is examined rather than the spatial angle because the former is more accurately known. Figure 12 shows the distribution of the projected angle between the proton and neutron directions for all the 1C fits, the shaded part being the contribution of those events which also gave a 4C fit. The distribution has been folded about the ordinate at 0° , and covers a range 0° to 180° . It may be seen that the shaded events form a narrow peak at small angles whilst the other



interactions are isotropically distributed as expected. The events in the peak are identified as genuine elastic scatters.

In the second test measured rather than fitted quantities are used. The recoil track is postulated to be a deuteron and the events sub-divided into groups according to the momentum derived from the range. For each interaction the following quantity is calculated

$$A = T - \beta pc \cos \theta$$

where p is the momentum, T the kinetic energy, θ the angle of emission and βc the c.m.s. velocity of the supposed deuteron. For elastic interactions it is expected that the tested quantity A should be close to zero. This follows because in the transformation relationship

$$E' = \gamma(E - p\beta c \cos \theta)$$

the total energy of the deuteron in the laboratory system after the collision is given by

$$E = M_d + T$$

where M_d is the rest mass of the deuteron. The total

energy of the deuteron in the centre of mass for an elastic collision will be

$$E' = \gamma M_d , \quad \gamma = 1 / \sqrt{1 - \beta^2}$$

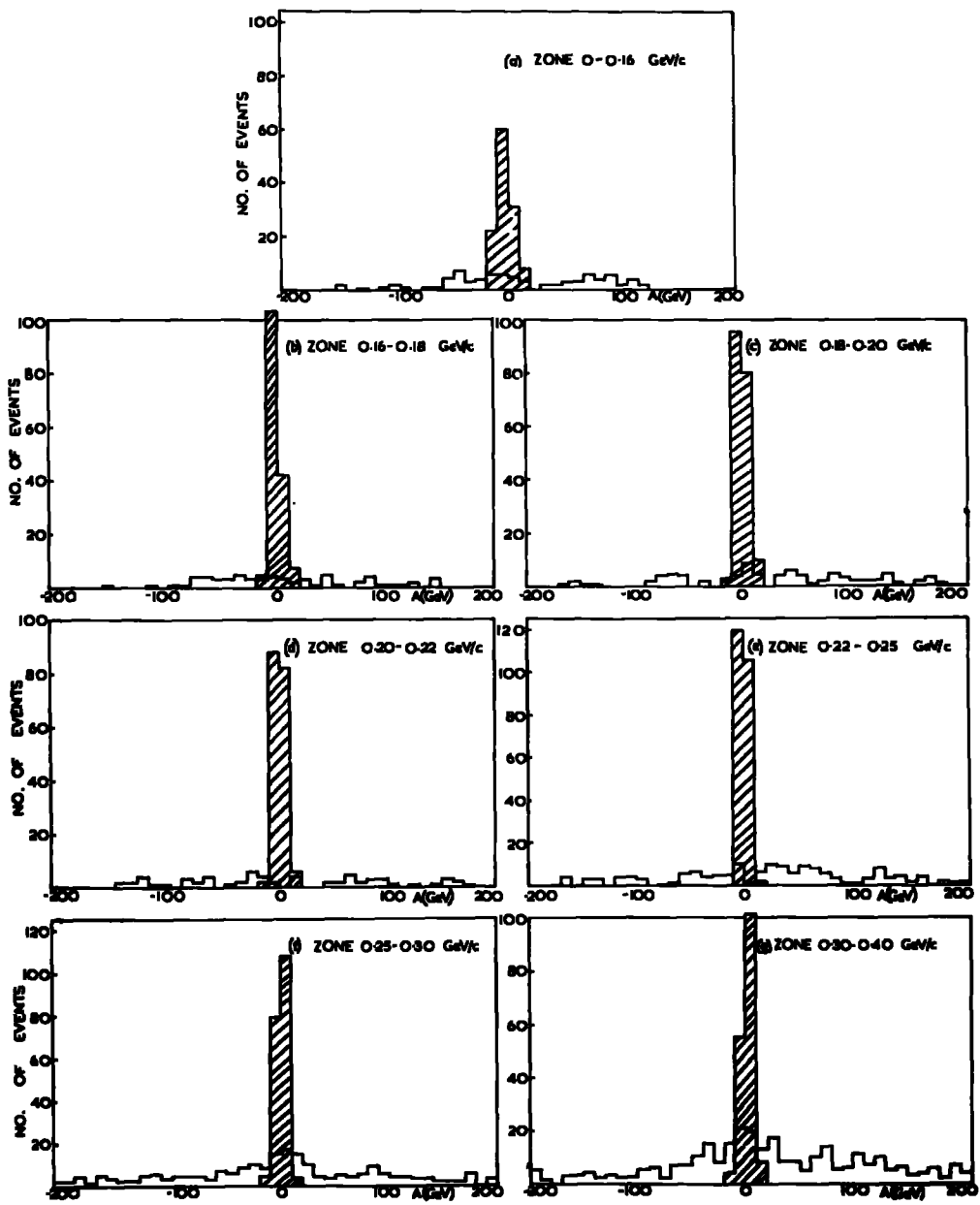
from which it follows that $T - \beta p \cos \theta = 0$.

The background expected for the other events has not been calculated. The distribution of the events for the momentum sub-groups is shown in figure 13 and again the shaded events are those which give 4C fits. In each sub-group these events all fall into a narrow peak centred at $A = 0$ and the background is fairly isotropic. This test confirms the results of the first and it may be assumed therefore that the 4C fits are the real elastic interactions and that the contamination of the selected sample is at most a few percent. The second test also shows that the fits are equally good for all ranges of recoil.

3.51 Corrections for Scanning Loss.

Before calculating the cross sections a correction for scanning losses has been made to the number of events found. Events are missed whilst scanning mainly because the recoil tracks are very short. Besides the loss of events having recoils of short range, events with longer

FIG 13 (a) to (g) Distribution of quantity \dot{A} for different momentum zones of recoil. \dot{A} is defined by $A \pm T - \mu p \cos \theta$.



recoils may also be lost where the tracks are foreshortened by steep dip in the chamber. For tracks in the film plane the minimum range detectable is about 1 mm. as pointed out previously. The sample has been divided as before in 'test A' according to the momentum of the recoil deuteron and for each momentum interval a plot has been made of the distribution of the angle which the recoil makes with the normal to the film plane. These distributions, separately for each laboratory and combined are shown in figure 14. It is seen that for small momenta there is a marked difference between the numbers of events measured by the two laboratories. The high loss of events with short recoils (up to 2 mm.) in the CERN scan may have been the result of a primary concern with interactions of higher multiplicities. Because of this discrepancy only the results of the Ecole Polytechnique have been used to determine cross sections for deuteron momenta less than 0.22 GeV/c. Above this momentum the scanning efficiencies of Paris and CERN become comparable as may be seen from the normalised diagram of figure 15, where the ratios of the numbers of 40 events found by each laboratory in the different momentum intervals are shown.

FIG. 14. (a)-(d) Distribution of events found as function of angle of recoil in chamber for different momentum zones.

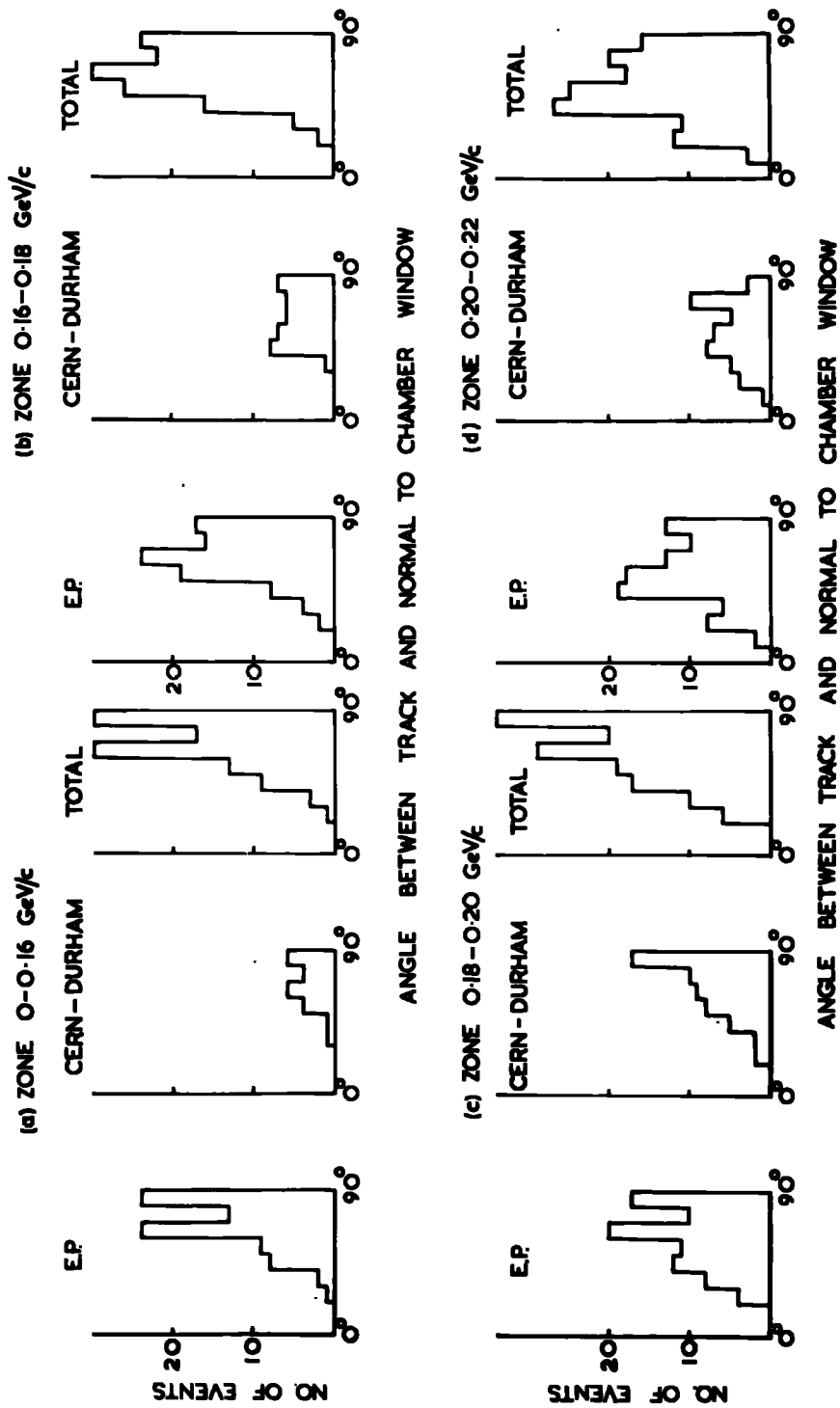
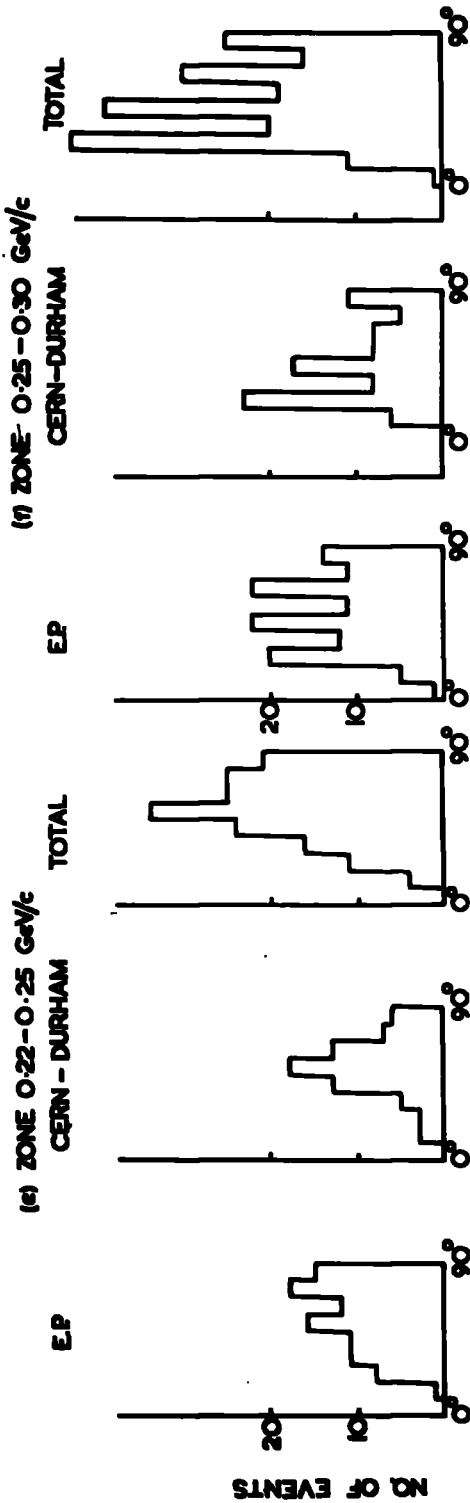
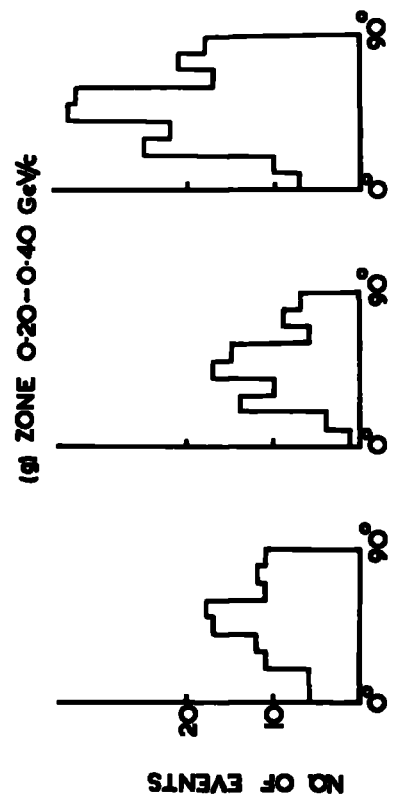


FIG.11. (e)-(g) Distribution of events found as function of angle of recoil in chamber for different momentum zones.



ANGLE BETWEEN TRACK AND NORMAL TO CHAMBER WINDOW



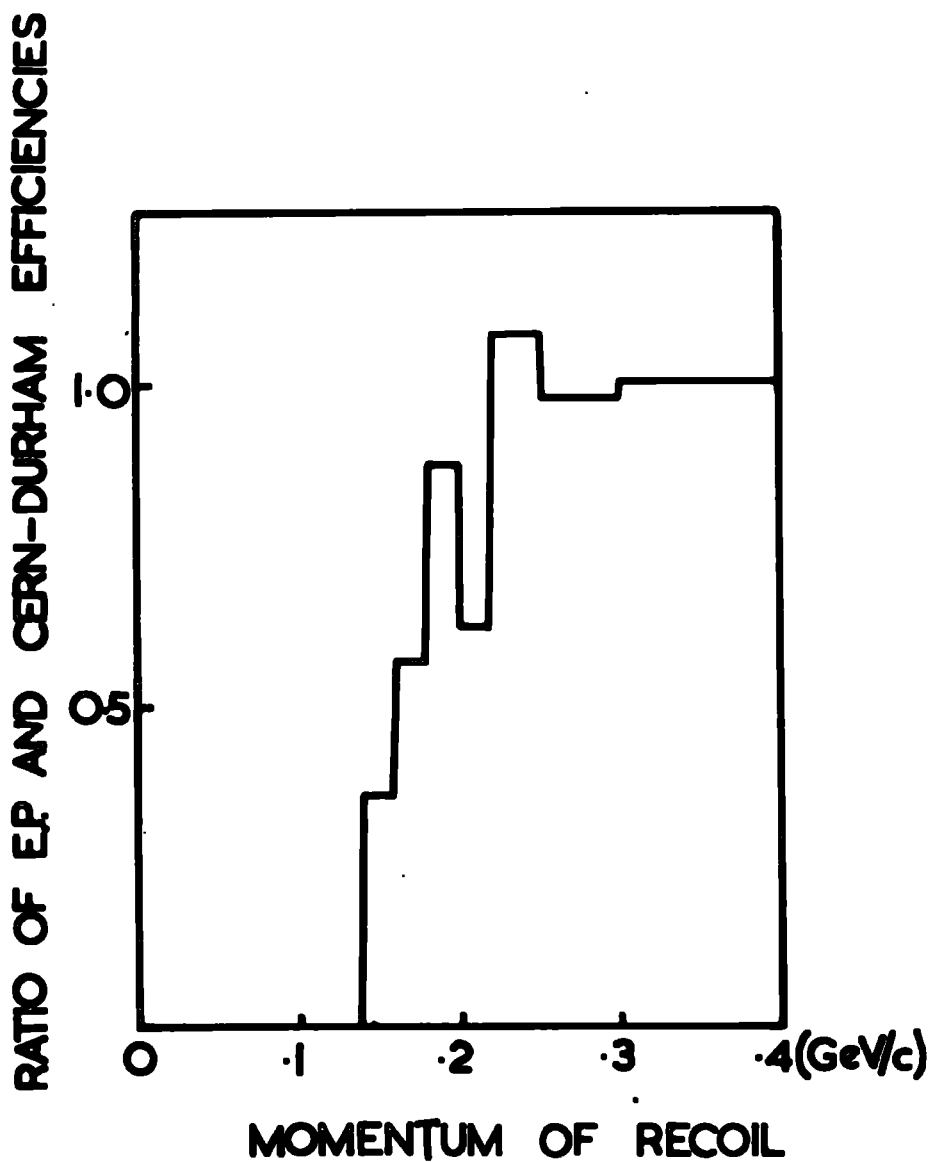


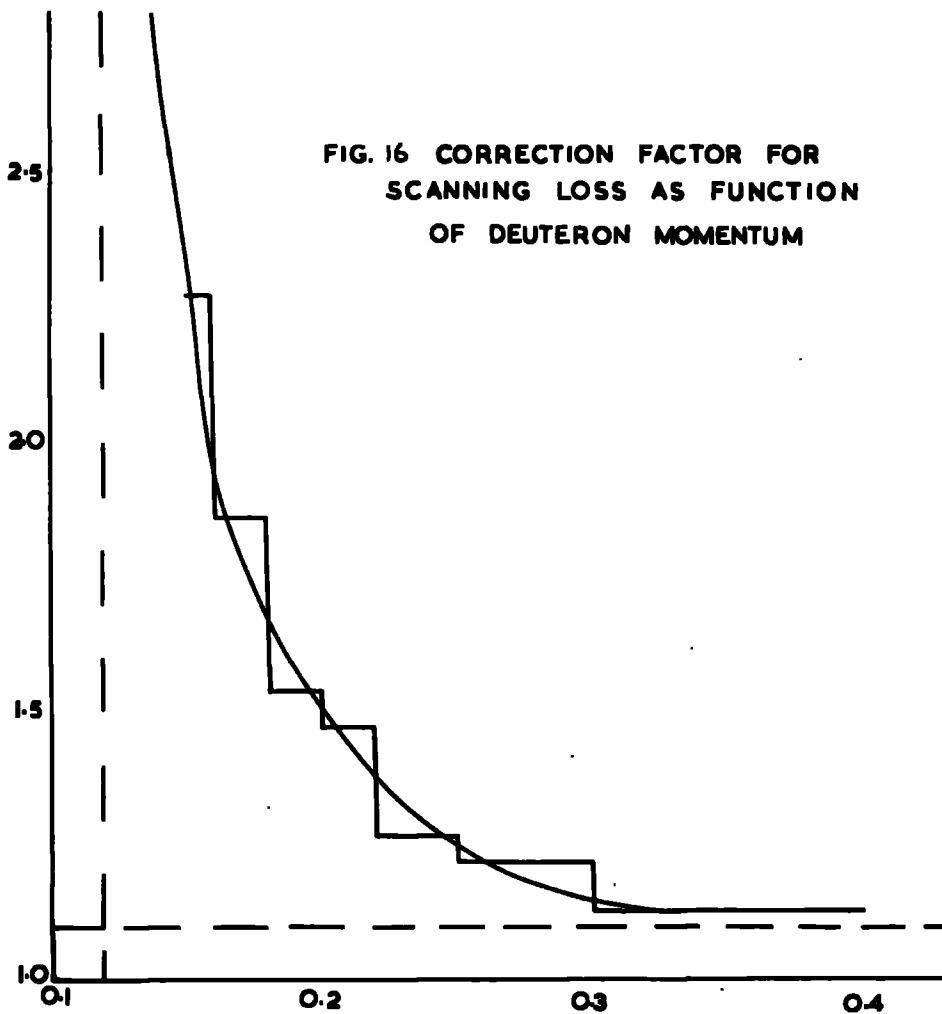
FIG.15 Ratio of EP and CERN-DURHAM scanning efficiencies as function of recoil momentum

To correct for the losses resulting from steep tracks it is necessary to assume that the angle of dip is distributed isotropically. For each of the momentum ranges of figure 14 it is assumed also that the number of events found will reach a plateau value when the recoil makes a certain large angle with the normal to the film plane. The angle and the plateau value are defined for each interval and the corresponding corrected number of events is then calculated. The corrected number will have only the same statistical weight as the smaller number of events falling under the plateau. Figure 16 shows the correction factors (i.e. the ratio of the corrected number to the uncorrected number) which have been determined for each of the momentum divisions. A curve has been fitted to the values which has an asymptotic behaviour for very large and very small recoil momenta. Using this curve the corrections have been made for the points of the differential cross section which are separated at intervals of $-t = 0.02(\text{GeV})^2$.

3.52 Experimental Differential Cross Section

The experimentally observed differential cross section for elastic scattering of 6 GeV/c π^+ mesons in deuterium

FIG. 16 CORRECTION FACTOR FOR
SCANNING LOSS AS FUNCTION
OF DEUTERON MOMENTUM



is shown in figure 17. The two points closest to the origin are based on the Paris data and the other eight represent the corrected combined data. The errors shown have been calculated to have the statistical weight of the uncorrected events found under the plateaux of figure 14. The points have been plotted for a cross section per event of $2.44 \mu\text{b.}$ calculated from the estimated track length scanned at Paris.

3.6 Optical Model Calculations

The differential cross section predicted by the optical model for a uniform deuteron has been calculated for a range of possible values of the radius R using the expression of Eq. 3. For a uniform nucleus the coefficient of absorption, K, may be written as

$$K = \frac{A\bar{\sigma}}{\frac{4}{3}\pi R^3}$$

from its definition given in 3.2, where A is the atomic weight and $\bar{\sigma}$ is the average total cross section for π -nucleon scattering. At 6 GeV/c, $\bar{\sigma} = 27.35 \text{ mb.}$ (Galbraith et al., 1965) when for $R \approx 2$ fermi the coefficient of

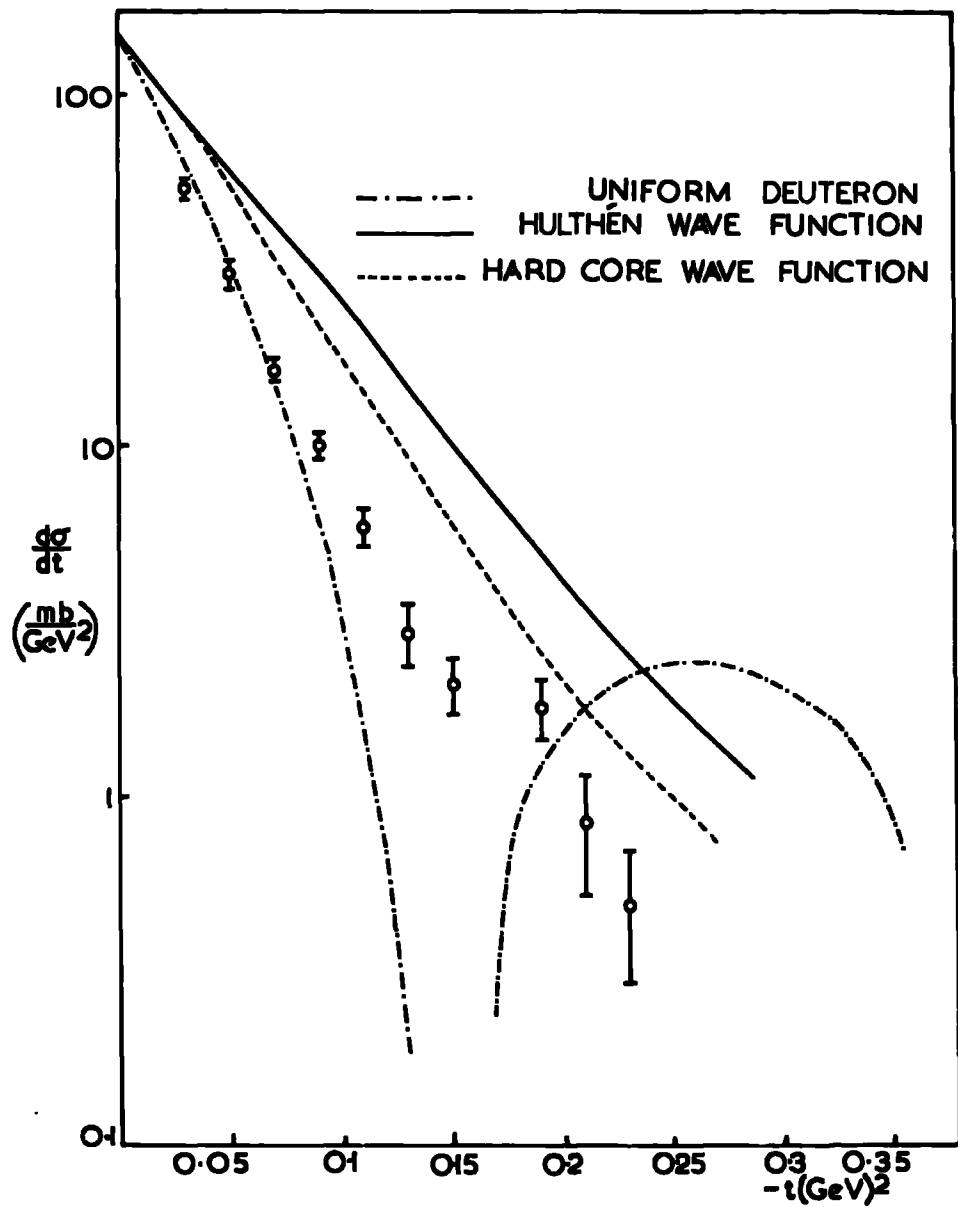


FIG.17. COMPARISON OF EXPERIMENTAL DIFFERENTIAL CROSS SECTION WITH PREDICTIONS OF OPTICAL MODEL .

absorption has typically a value of about 0.13 fermi^{-1} . To determine the change in wave number, k_1 , inside the nucleus using Eq.1 it is necessary to assume a value for the real potential, V_r . Examination shows that the exact value is not critical and $V_r = 35 \text{ MeV}$ has been taken (Evans 1955). Substituting the centre of mass values for k and p the value of k_1 is 0.177 fermi^{-1} .

To calculate the scattering amplitude given by Eq. 3 the expression has been divided into its real and imaginary parts each of which has been integrated numerically using the Elliott 803 computer. The imaginary part of the forward scattering amplitude, $\text{Im}f(0)$, has been normalised to the value given by the optical theorem, Eq. 4. For a total cross section at $6 \text{ GeV}/c$ of $\sigma(\pi-d) = 52.8 \text{ mb}$. (Galbraith et al., 1965) the optical value of $\text{Im}f(0)$ is 4.68 fermi . The ratio of the real to imaginary parts of the forward scattering amplitude is found to be very small, about 0.02 . The differential cross section was calculated for a range of angles in the centre of mass of 0° to 15° , corresponding to about 0° to 5° in the laboratory. For convenience the distribution is plotted finally as $d\sigma/dt$ against $-t$ where the following

relationships have been used as good approximations for small angles

$$d\sigma/dt = - \frac{\pi}{p^2} d\sigma/d\Omega$$

and
$$-t = p^2 \theta^2$$

The differential cross section predicted by the uniform nuclear model gives best agreement with the observed distribution for a deuteron radius, $R = 2.10$ fermi and the two distributions are shown together in figure 17. It can be seen that reasonable agreement is obtained only up to values of $-t$ less than $0.1 (\text{GeV})^2$ and the predicted secondary maximum at $-t = 0.25 (\text{GeV})^2$ is not observed experimentally. This result is not surprising since the deuteron has a diffuse structure rather than a clean edge.

A more detailed calculation has been made using the Hulthen and hard core wave functions described in Eq. 10 and Eq. 11. To use these wave functions in an optical model calculation it is necessary to rewrite them in terms of the distance from the centre of the nucleus, the half-separation, which is considered to be equivalent to the

radial parameter of the optical model. In this form the Hulthen wave function is written as

$$\psi(R) \propto \frac{e^{-\gamma R} - e^{-\delta R}}{R}$$

with $R = \frac{r}{2}$ and $\gamma = 0.464 \text{ fermi}^{-1}$ and $\delta = 2.404 \text{ fermi}^{-1}$:

The density of nucleons at radius R is then proportional to $|\psi(R)|^2$, and is normalised to the number of nucleons in the usual way. The coefficient of absorption may then be written in the following way, using the previously given value of $\bar{\sigma}$:

$$K = 0.743 \left[\frac{e^{-\gamma R} - e^{-\delta R}}{R} \right]^2 \text{ fermi}^{-1} \quad (12)$$

The expected value of K at the centre of the nucleus is then

$$\begin{aligned} K(0) &= 0.743 (\delta - \gamma)^2 \text{ fermi}^{-1} \\ &= 2.80 \text{ fermi}^{-1} \end{aligned}$$

and therefore, $K = 0.265 \left[\frac{e^{-\gamma R} - e^{-\delta R}}{R} \right]^2 K(0) \text{ fermi}^{-1}$

If it is assumed that the real potential is related to the density then the change in wave number may be written from Eq. 1 as

$$k_1 = kVr/p\beta c = \frac{k}{p\beta c} \frac{Vr(0)}{(\delta - \gamma)^2} \left[\frac{e^{-\gamma R} - e^{-\delta R}}{R} \right]^2 \text{ fermi}^{-1}$$

where $V_r(0)$ is the real potential at the centre of the nucleus given in MeV. Then for π^+ mesons at 6 GeV/c in the laboratory system

$$\beta = 1$$

$$k_{c.m.s.} = 11.13 \text{ fermi}^{-1}$$

$$P_{c.m.s.} = 2.20 \cdot 10^3 \text{ MeV}/c$$

and using these values

$$k_1 = 1.34 \cdot 10^{-3} V_r(0) \left[\frac{e^{-\gamma R} - e^{-\delta R}}{R} \right]^2 \text{ fermi}^{-1} \quad (13)$$

Using the expressions above, Eq. 12 and Eq. 13, the variation of K_s and k_1s with impact parameter has been calculated and the results for K_s are shown in figure 18 together with the corresponding curves for the hard core wave function and for the uniform nucleus. The curves are plotted for impact parameters up to 3 fermi, beyond which they have values close to zero.

The real and imaginary parts of the forward scattering amplitude have been calculated from Eq. 3 using a numerical method as before but in this case with K_s and k_1s as functions of the impact parameter ρ . The values of $K(0)$ and $V_r(0)$ were adjusted until the imaginary part of the

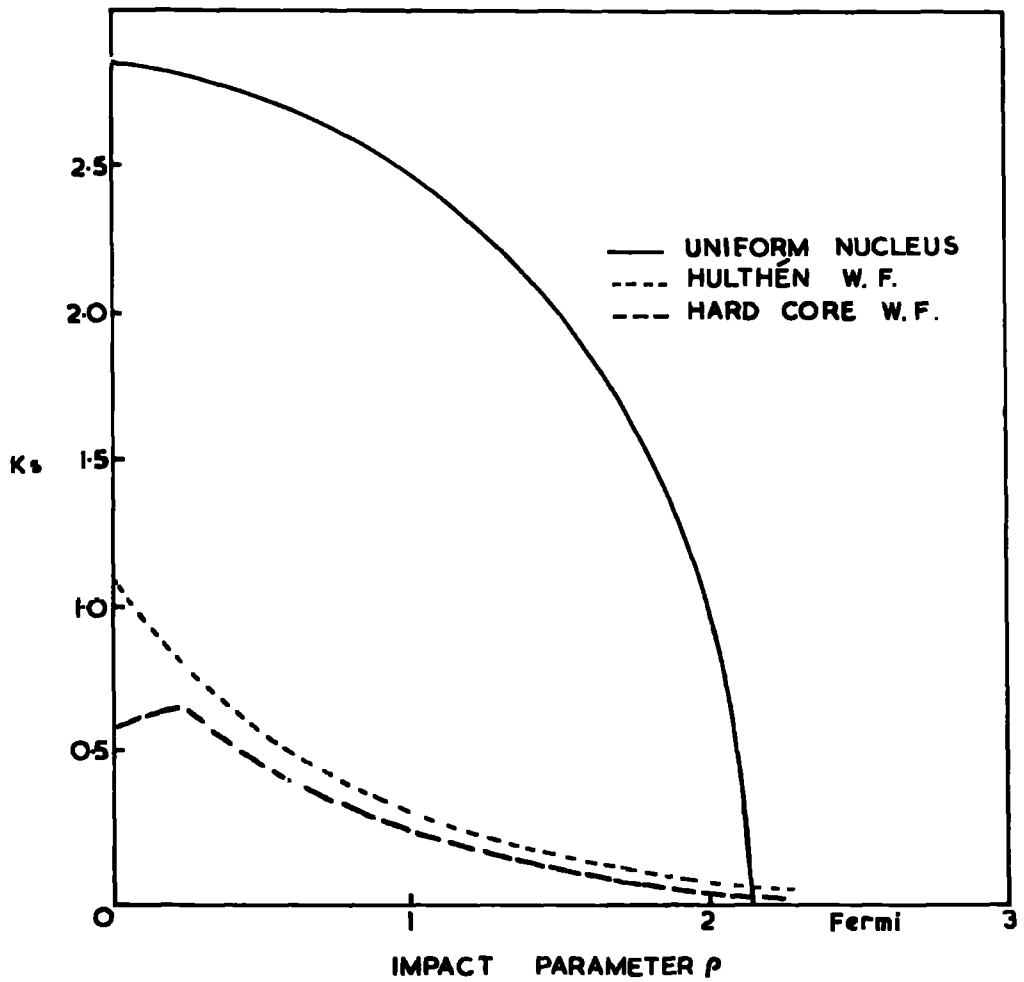


FIG. 18 VARIATION OF K_s WITH IMPACT PARAMETER ρ . FOR UNIFORM DEUTERON AND FOR DEUTERON DESCRIBED BY HULTHÉN AND HARD CORE WAVE FUNCTIONS.

forward amplitude, $\text{Im}f(0)$, attained the value given by the optical theorem. Until recently the real part $\text{Re}f(0)$ was believed to be zero but there are indications that it may not be negligible. An arbitrary value one tenth of that of $\text{Im}f(0)$ has been adopted; the differential cross section is not sensitive to the exact value when it is small. Having normalised the distribution the complete differential cross section was computed for a range of angles 0° to 15° in the c.m.s. Again the distribution has been finally plotted as $d\sigma/dt$. In figure 17 the differential cross sections for the Hulthen and hard core wave functions are shown in comparison with the experimental data and also with the prediction of the uniform nucleus. The secondary maximum associated with the uniform deuteron does not appear in either of the two predicted distributions but apart from this feature the agreement is very poor. Both distributions are too broad and the radii which would correspond to the two distributions if a uniform model were fitted are 1.7 fermi for the Hulthen wave function and 1.85 fermi for the hard core wave function.

3.7 Impulse Model Calculations

In order to evaluate the expression, Eq. 9, given for the angular distribution we require the functions $f_n(q)$, $f_p(q)$ and $S(q')$ and the forms suggested by Harrington have been used. These are

$$f_n(p, q) = iA_n(p) \exp[-a_n(p)q^2]$$

$$f_p(p, q) = iA_p(p) \exp[-a_p(p)q^2] + F_C$$

$$S(q') = \exp(-a_d q'^2)$$

The parameters A_n , A_p , a_n , a_p , and a_d are functions of the incident momentum p and are chosen to fit the low momentum transfer experimental data. F_C is the Coulomb amplitude and is given at these small momentum transfers in the notation of Bellettini et al. to be

$$F_C = -\frac{2\xi}{q} p \quad \text{where} \quad \xi = \frac{e^2}{\hbar\beta c} = \frac{1}{137\beta}$$

$A_n(p)$ and $A_p(p)$ are complex numbers proportional to the total cross sections for π -n and π -p elastic scattering

respectively. Then

$$A_n(p) = f_{on}(1+i\rho_n) \quad \text{and} \quad A_p(p) = f_{op}(1+i\rho_p)$$

where f_{on} is an abbreviation for $\frac{p\sigma_T(\pi n)}{4\pi\hbar}$, and f_{op} for $\frac{p\sigma_T(\pi n)}{4\pi\hbar}$ and ρ_n and ρ_p are the ratios for the real to

imaginary amplitudes for neutron and proton scattering respectively. Making these substitutions the differential cross section is obtained after integration to be

$$\begin{aligned} d\sigma/d\Omega_{el} = S^2(\frac{1}{2}q) & \left[|f_n|^2 + |f_p|^2 + 2(\text{Re}f_n \text{Re}f_p + \text{Im}f_n \text{Im}f_p) \right] \\ & - \frac{S(\frac{1}{2}q)}{\pi p} \left[M(\text{Im}f_n + \text{Im}f_p) - N(\text{Re}f_n + \text{Re}f_p) \right] + \frac{(M^2+N^2)}{(2\pi p)^2} \end{aligned} \quad (14)$$

M and N are given below. Written in the above form the differential cross section $d\sigma/d\Omega$ may be evaluated numerically.

$M =$

$$\frac{2\pi(\rho_p\rho_n-1)p^2f_{op}f_{on}\exp\left[-\frac{1}{8}(\alpha_p+\alpha_n)q^2\right]}{(\alpha_d + \alpha_p + \alpha_n)} - \frac{16\pi p^2f_{on}\rho_n\exp(-\frac{1}{8}\alpha_n q^2)}{q^2(\alpha_d + \alpha_n)}$$

N =

$$\frac{2\pi(\rho_p + \rho_n)p^2 f_{op} f_{on} \exp\left[-\frac{1}{8}(\alpha_p + \alpha_n)q^2\right]}{(\alpha_d + \alpha_p + \alpha_n)} - \frac{16\pi\epsilon p^2 f_{on} \exp\left(-\frac{1}{8}\alpha_n q^2\right)}{q^2(\alpha_d + \alpha_n)}$$

The form factor constants α_i in these expressions for M and N are related to the constants a_i used previously thus

$$\alpha_i = 2a_i$$

The differential cross sections have been calculated using Eq. 14 for both form factors of the strong interaction, derived from the Hulthen and hard core wave functions. The final calculations have been made on the I.B.M. 1620 computer in Paris using a modified CERN programme. For the ratios of the real and imaginary amplitudes for the proton ρ_p and the neutron ρ_n the following values have been used (Bellettini et al., 1965)

$$\rho_p = \rho_n = -0.33$$

and for the total cross sections (Galbraith et al., 1965) for π -p and π -n scattering

$$\sigma_T(\pi p) = 26.2 \text{ mb.}$$

$$\sigma_T(\pi n) = 28.5 \text{ mb.}$$

For the constants of the form factors similar values to those of Bellettini et al.(1965) have been used.

$$\alpha_p = \alpha_n = 7.5 \text{ (GeV/c)}^{-2}$$

$$\alpha_d = 44 \text{ (GeV/c)}^{-2}$$

The results of the calculations are shown in comparison with the observed differential cross section in figure 19 and it can be seen that the predictions of the impulse model are in very good agreement with experiment. For the curve derived for each wave function has been calculated the corresponding value of χ^2 for the ten observed values of $d\sigma/dt$. It is found that

$$\chi^2 \text{ Hard Core} = 8.58$$

$$\chi^2 \text{ Hulthen} = 35.3$$

and it may be concluded that the hard core wave function is a satisfactory description of the deuteron whilst the Hulthen wave function is not.

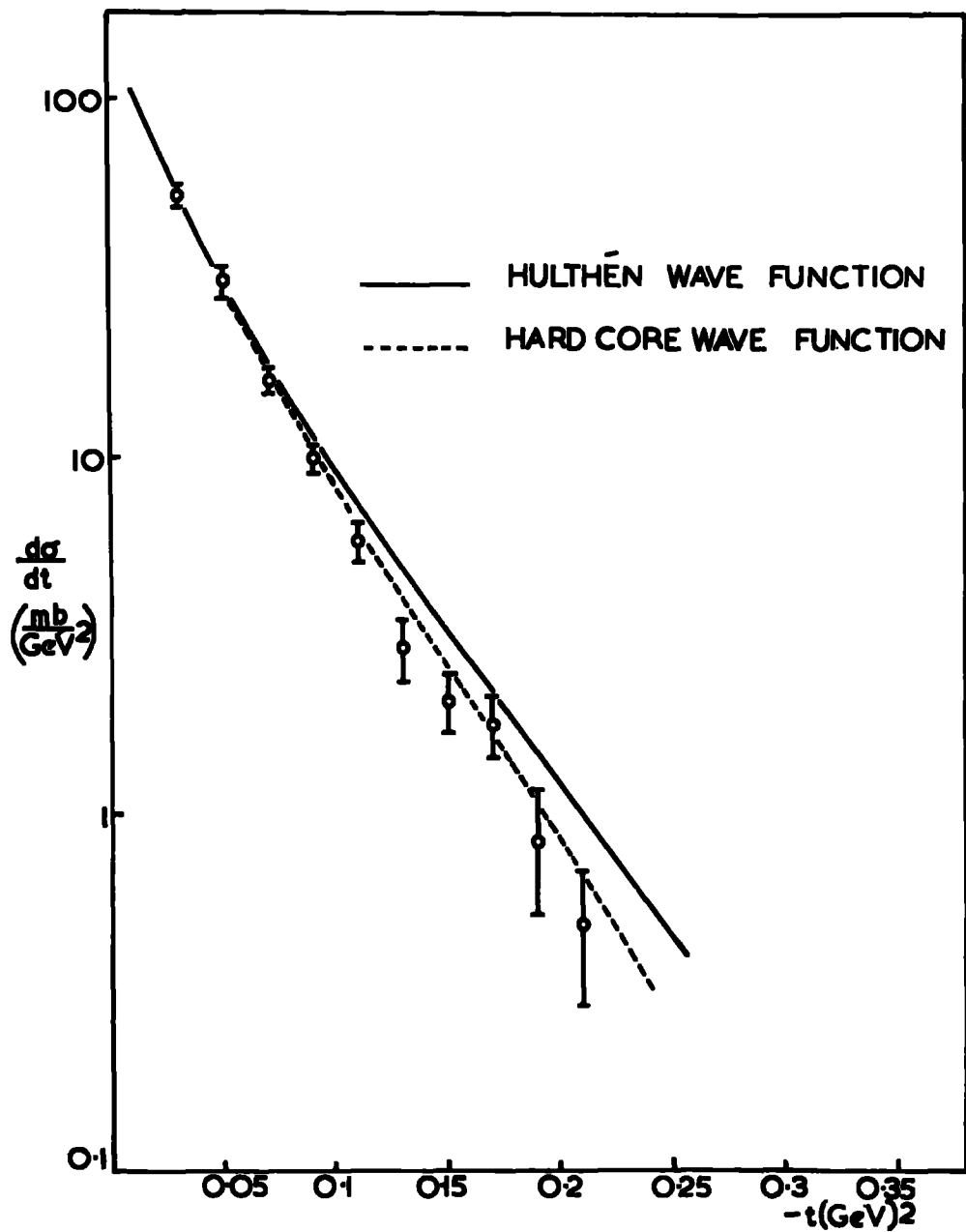


FIG.19. COMPARISON OF EXPERIMENTAL
 DIFFERENTIAL CROSS SECTION
 WITH PREDICTIONS OF IMPULSE
 MODEL.

CHAPTER 4

INELASTIC π^+ p INTERACTIONS OF HIGH MULTIPLICITY AT 5 GEV/c

4.1 Introduction

The majority of the secondary particles produced when meson and proton beams are in collision with nucleon targets are found to be π mesons and a feature of the interactions is the formation of unstable multi-pion resonances and nucleon isobars. The information learned from the kinematic correlation of the particles in the final state is mostly for the energy region up to about 10 GeV and generally only final states containing two to five particles have been closely examined. Comparatively little detailed information is available for interactions in which more secondary particles are produced, largely because of the small cross sections for these events and also because of the difficulties of analysis when so many different combinations of particles must be considered. Until experimental data are adequately available it is difficult to devise a dynamical model for the analysis of very high multiplicity interactions but lately a group of physicists at CERN, under the guidance of Professor Van Hove, have begun to study the theoretical aspects of the

problem. At the present time therefore the analysis of such interactions can only be made in general terms following the models which have been successful in interpreting the interactions of lower multiplicity, and in particular the peripheral model whose most important features are described briefly here.

4.11 The Peripheral Model

A detailed analysis of inelastic interactions in which there are less than six particles in the final state shows that frequently the production takes place by way of a quasi-two-body interaction in which one or both of the mass centres are resonances. Such processes are found to occur usually for small momentum transfers with the decay products of the resonances collimated into the forward and backward directions of the centre of mass system. It may be inferred from this that there is a tendency for the directions of the incident particles to be maintained and that therefore the interaction does not take place centrally after a head on collision but that rather the particles meet in a glancing manner. From this point of view a meson scattering on a nucleon will interact only with the outer structure of the nucleon, the mesic 'cloud' and not with its 'core'. For such peripheral interactions the long range force concerned is described, using the

Yukawa theory, in terms of the exchange of a virtual particle. Generally it is assumed (Ferrari and Sellari, 1962) that the exchanged particle is a meson since these are the lightest of the strongly interacting particles and have, therefore, the largest interaction radii. The Feynman diagram for a two-body reaction with one meson exchange (O.M.E.) of the type

$$a + b \rightarrow c + d$$

is shown in figure 20 and occurs with the exchange of particle e. Generally c and d are resonances which later decay into the particles seen in the final state, sometimes by way of other lighter resonances. The invariant square of the four-momentum transfer between particles a and c or between b and d is defined by

$$\begin{aligned} \Delta^2 &= -(p_c - p_a)^2 = -(p_d - p_b)^2 \\ &= -(m_c^2 + m_a^2) + 2E_c E_a - 2\bar{p}_c \bar{p}_a \cos \Theta^* \end{aligned} \quad (15)$$

where the p_i are the four-momenta of the particles and Θ^* is the production angle. The notation is

$$p_i = (E_i, \bar{p}_i), \text{ from which } p_i^2 = E_i^2 - \bar{p}_i^2 = m_i^2$$

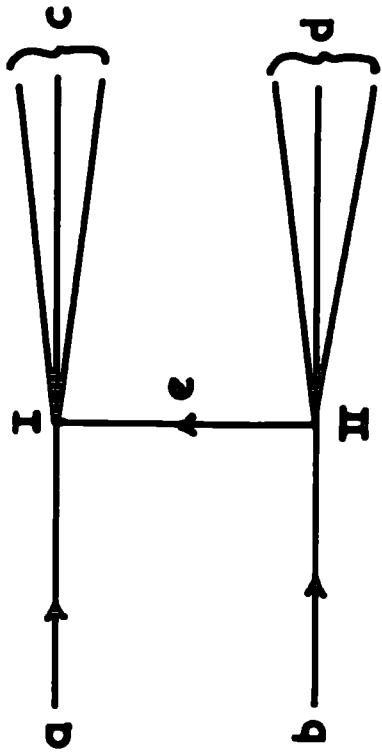
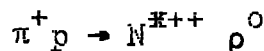


FIG. 20 FEYNMAN DIAGRAM FOR REACTION $ab \rightarrow cd$

where E_i , \vec{p}_i , and m_i are the total energy, three-momentum and mass of the particle indicated. It follows from the conservation of four-momentum that $p_e = p_c - p_a$ and therefore $\Delta^2 = -m_e^2$ where m_e is the mass of the exchange particle. Since Δ^2 is always positive the interaction takes place off the mass-shell and m_e is a virtual mass. The matrix element for this reaction (see e.g. Schmitt, 1965) includes a term, $1/(\Delta^2 + m_e^2)$, the propagator of the exchanged particle, and this term has a singularity in the unphysical region at the point $\Delta^2 = -M_e^2$ where the exchange particle is real, M_e being the physical mass of the particle. The influence of the propagator upon the differential cross section, $d\sigma/d\Delta^2$, will depend on the physical mass of the exchange particle and will be greatest for the exchange of a pion because the pole will then lie close to the physical region and the distribution will be peaked at small values of Δ^2 . In a typical example of one pion exchange, the reaction at 4 GeV/c



reported by the Anglo-German Collaboration (1965) the distribution of Δ^2 is peaked at $0.1 (\text{GeV})^2$ and almost all of the events occur for $\Delta^2 < 0.5 (\text{GeV})^2$. It is found,

however, that the differential cross section predicted by the O.M.S. model has a much larger peak at small Δ^2 and falls off less rapidly than the observed distribution (Jackson, 1965 from data of the Saclay-Ursay-Bari-Bologna Collaboration, 1964). By including form factors in the matrix element (Ferrari and Sellari, 1964) it is possible to fit the experimental distribution using the O.M.S. model but the fitting is largely empirical and it is found also that the form factors have an energy dependence. A more satisfactory explanation can be made if the absorptive effects of the other open inelastic channels are considered (Gottfried and Jackson, 1964). At high energies there are many other open inelastic interactions competing with the quasi-two-body process and this leads to the reduction of the amplitude of the two-body process particularly for small impact parameters. The quasi-two-body interaction then depends almost entirely upon high partial waves which lead to large scattering angles and it becomes possible to predict satisfactorily the observed distribution of Δ^2 . In peripheral interactions the resonant particles will be produced in a mixture of spin states (see e.g. Jackson, 1965) dependent upon the spin and parity of the exchange particle. Information may therefore be obtained about the exchange particle by observing the decay distribution of the resonances.

In the present experiment the data have been examined to see whether the peripheral model is still applicable to the interpretation of very high multiplicity interactions. Evidence for peripheralism has been looked for in the distributions of the production angles of the secondaries and in the distributions of Δ^2 . The effective mass plots of the different particle combinations have been studied to see if quasi-two-body processes occur and a systematic study has been made of the decay distributions of the resonances which have been observed.

4.2 Experimental Results

From the 150,000 photographs of the interaction of π^+ mesons in hydrogen at 4.98 GeV/c the six laboratories of the collaboration have analysed approximately 3,500 events in which there are six charged particles in the final state. These interactions have been fitted to the following interpretations which include only non-strange particles

$\pi^+ p \rightarrow p \pi^+ \pi^+ \pi^+ \pi^- \pi^-$	1052 events	(i)
$\rightarrow p \pi^+ \pi^+ \pi^+ \pi^- \pi^- \pi^0$	1595 events	(ii)
$\rightarrow n \pi^+ \pi^+ \pi^+ \pi^+ \pi^- \pi^-$	279 events	(iii)
$\rightarrow n \pi^+ \pi^+ \pi^+ \pi^+ \pi^- \pi^- \pi^0$	152 events	(iv)
$\rightarrow p \pi^+ \pi^+ \pi^+ \pi^- \pi^- + m\pi^0, \quad m > 2$	389 events	(v)

The analysis into the 4C channel, (i), and the two 1C channels, (ii) and (iii), has been made in the manner described in section 2.5 using the bubble densities of the tracks and accepting events with $\chi^2 \leq 6$ for the 1C fits and $\chi^2 \leq 24.5$ for the 4C fits. The two nofit channels, (iv) and (v), have been separated by means of the squared missing mass calculated for each interaction from the measured quantities.

4.21 Cross Sections

The cross sections given here have been calculated from the Durham data after determining the average number of tracks per frame. Corrections have been made to take into account

- i) the dip and curvature of the beam
- ii) the number of tracks leaving the side of the fiducial volume
- iii) the shorter track length of particles which interact in the volume,

and the total length of track scanned has been calculated to be $(16,20 \pm 0.02) 10^4$ metres. The error given is due mainly to the statistical error resulting from counting tracks in only one tenth of the frames of each film. The

overall scanning efficiency is $(99.8 \pm 0.1)\%$ (see Chapter 2, 2.13) and the corrected total number of six-prong events is found to be 743. The total cross-section for the six-pronged events is

$$\sigma_{\text{total}} = (1.13 \pm 0.07) \text{ mb.}$$

The partial cross sections for the different channels are summarised in table I.

TABLE I

Channel	Partial Cross Section $\mu\text{b.}$
$p \pi^+ \pi^+ \pi^+ \pi^- \pi^-$	400 ± 30
$p \pi^+ \pi^+ \pi^+ \pi^- \pi^- \pi^0$	600 ± 40
$n \pi^+ \pi^+ \pi^+ \pi^+ \pi^- \pi^-$	110 ± 10
$n \pi^+ \pi^+ \pi^+ \pi^+ \pi^- \pi^- \pi^0$	} 210 ± 20
$p \pi^+ \pi^+ \pi^+ \pi^- \pi^- + m\pi^0$	
$m \geq 2$	

A comparison of the cross sections given above with the results derived from small statistics by the Aachen-Berlin-

Bonn-Hamburg-Munich Collaboration (1966) for the same reactions at 4 GeV/c shows that the cross sections for high multiplicity interactions have a strong energy dependence. In channel (i), for example, the cross section at 4 GeV/c is 250 ± 40 $\mu\text{b.}$ and the same cross section is given for channel (ii) at this lower momentum.

In this dissertation a report is given of the results of the study of the 4C events in channel (i).

4.22 Distributions of M^2 and χ^2 for 4C events

The distribution of the missing mass squared is shown in figure 21 for the events of this channel and as expected the distribution is peaked sharply at $M^2 = 0$ having a width of 0.0004 $(\text{GeV})^2$. The distribution is skewed slightly towards positive values of M^2 but this asymmetry is not thought to represent any significant bias of the sample. The χ^2 distribution, shown in figure 22 is in reasonably satisfactory agreement with the theoretically predicted curve for four degrees of freedom. The sample of 4C events is believed to be free from any systematic biases due to faults of measurement or selection.

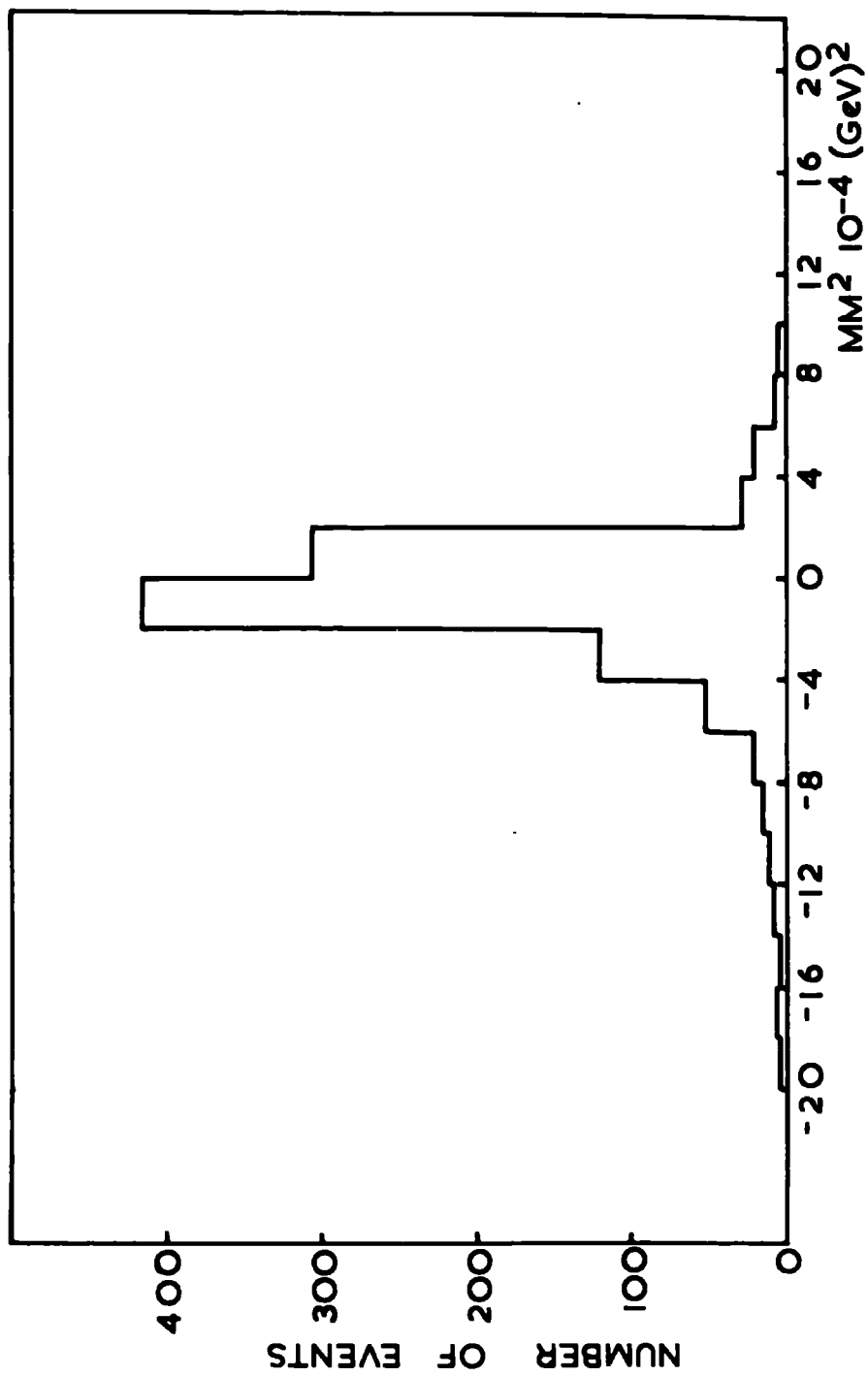


FIG. 21 DISTRIBUTION OF SQUARED MISSING MASS

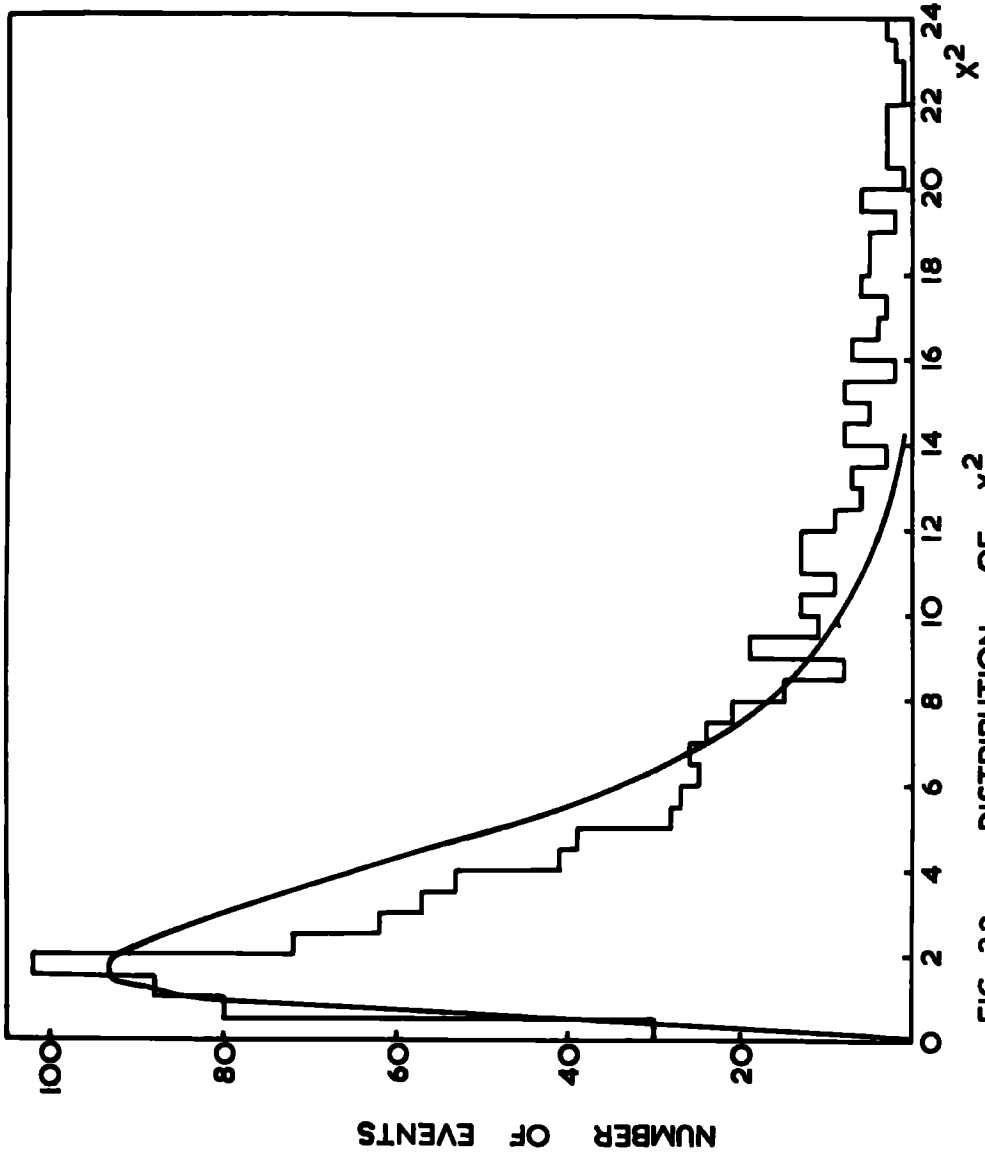


FIG. 22 DISTRIBUTION OF X²

4.23 Effective Mass Distributions of $p\pi^+$, $\pi^+\pi^-$, and $p\pi^-$

The overall effective mass distributions of the $p\pi^+$ and $\pi^+\pi^-$ combinations are shown in figures 23 and 24 and contain three and six entries per event respectively. Both mass distributions differ greatly from the predictions of pure phase space and they show that, as in the lower multiplicity interactions in this energy region, there are large numbers of the N^{*} (1236) and of the ρ resonances produced. The $p\pi^+$ mass distribution is seen to be dominated by the N^{*} formation centred at 1210 MeV. The large shift from the accepted value of 1236 MeV has been observed in other experiments (e.g. Boldt et al., 1964) and is thought to depend on the angular momentum of the resonant state and the orbital angular momentum of the two-body decay (Jackson, 1964). The width, Γ , has been estimated by fitting to the observed mass distribution a Breit Wigner shape and the best fit has been obtained for $\Gamma = 125$ MeV.

In the $\pi^+\pi^-$ mass distribution the only observed enhancement is the peak centred at 730 MeV which is attributed to the production of the ρ^0 particle. The shifting of the centre of the peak from its accepted value of 765 MeV may be due in part to interference effects as well as to an angular momentum effect. It has not been

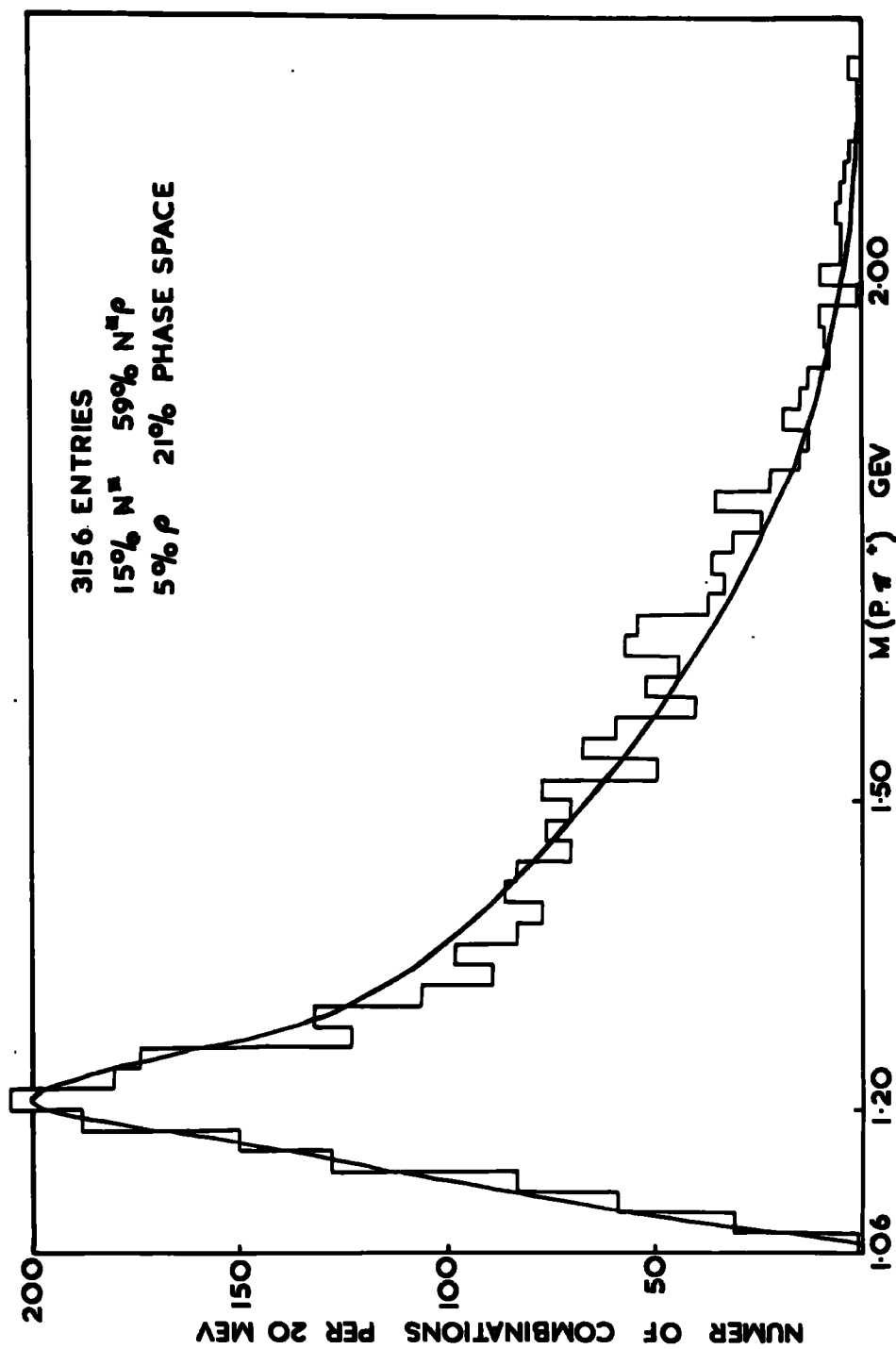


FIG. 2.3 EFFECTIVE MASS OF P π^+

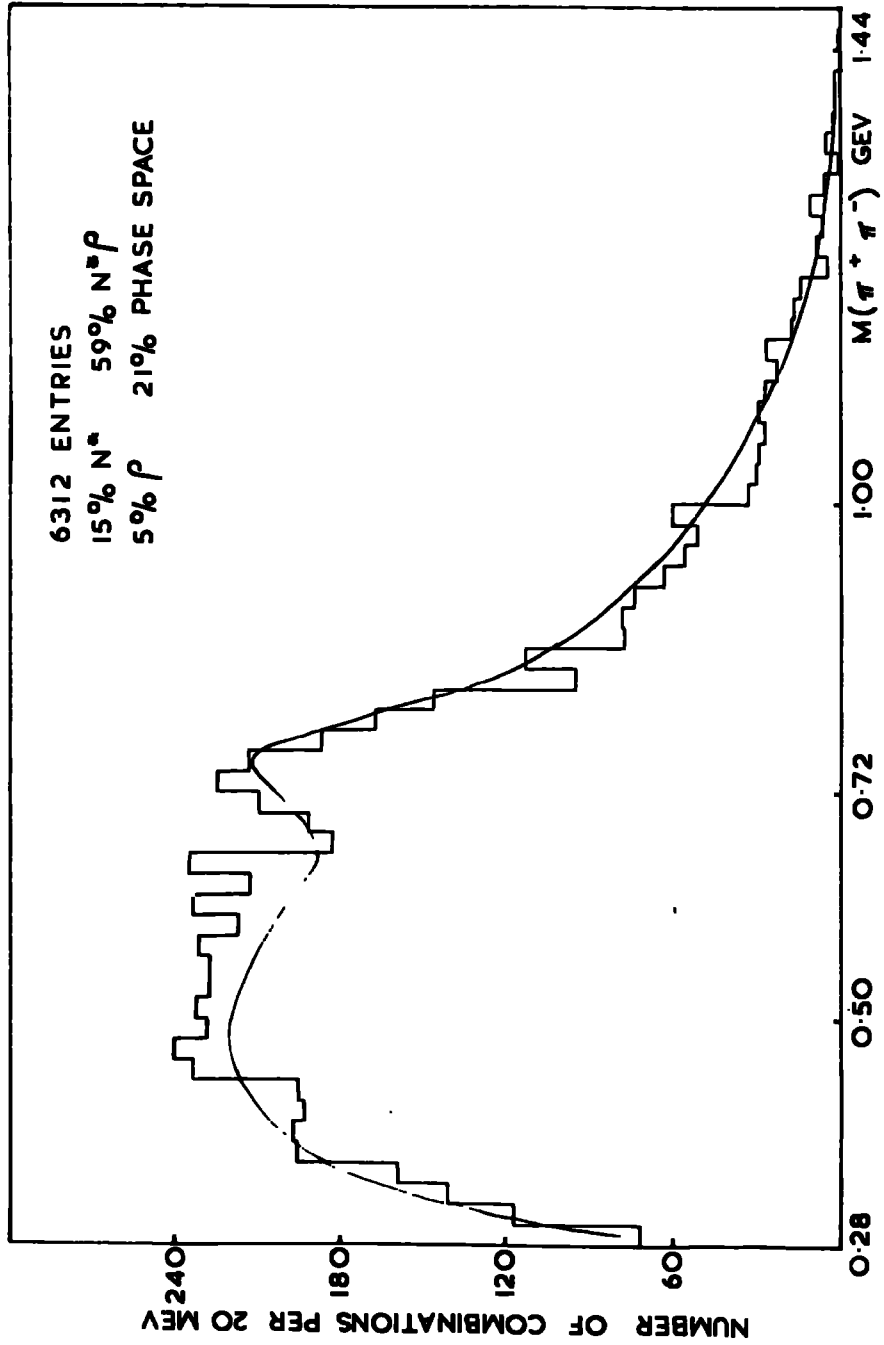


FIG. 2.4 EFFECTIVE MASS OF $\pi^+ \pi^-$

possible to estimate the width of the observed peak because the large background prevents the fitting from being sensitive to the value of the width. An enhancement at 670 MeV in the $\pi^+\pi^-$ distribution has been reported recently for the same reaction at 4 GeV/c (Aachen-Berlin-Bonn-Hamburg-Munich Collaboration, 1966) and it is suggested that this might be connected with the ϵ meson (Hagopian et al., 1965). In the present experiment which has much larger statistics there is no evidence for this enhancement which is therefore believed to be a statistical fluctuation.

An estimate of the proportions of the production of the N^* and the ρ^0 has been made as follows. Mass spectra have been computed by FOWL for both combinations, $\pi\pi^+$ and $\pi^+\pi^-$, based on the assumption that all the interactions take place by way of

- i) pure phase space
- or, ii) the production of an N^*
- or, iii) the production of a ρ^0
- or, iv) the production of an N^* and a ρ^0 .

The two observed effective mass distributions have then been fitted with backgrounds which are the sum of these four spectra in proportions which have been estimated by

a least squares fit. The best fit has been obtained for the following proportions

15% N^* , 5% ρ^0 , 59% $N^*\rho^0$, and 21% pure phase space.

Whilst it is believed that the estimations of the total N^* and ρ^0 production, 74% and 64% respectively, are valid representations of the data it should be pointed out that the proportion of the correlated $N^*\rho^0$ cannot be sensitively determined. Therefore the estimated 59% of correlated production is considered to be an upper limit and the true proportion may lie between this figure and the 47% expected statistically. The calculated backgrounds are shown with the experimental distributions in the figures and the fit is seen to be satisfactory. The background spectra for all the effective mass distributions have been calculated with the proportions given and the pure phase space distributions are not shown. It is hoped in this way to avoid large deviations from the backgrounds resulting from kinematic reflections of the N^* and of the ρ^0 production.

The effective mass distribution of the $\pi\pi^-$ combination is shown in figure 25 and no enhancement is observed in the region of the $N^*(1236)$.

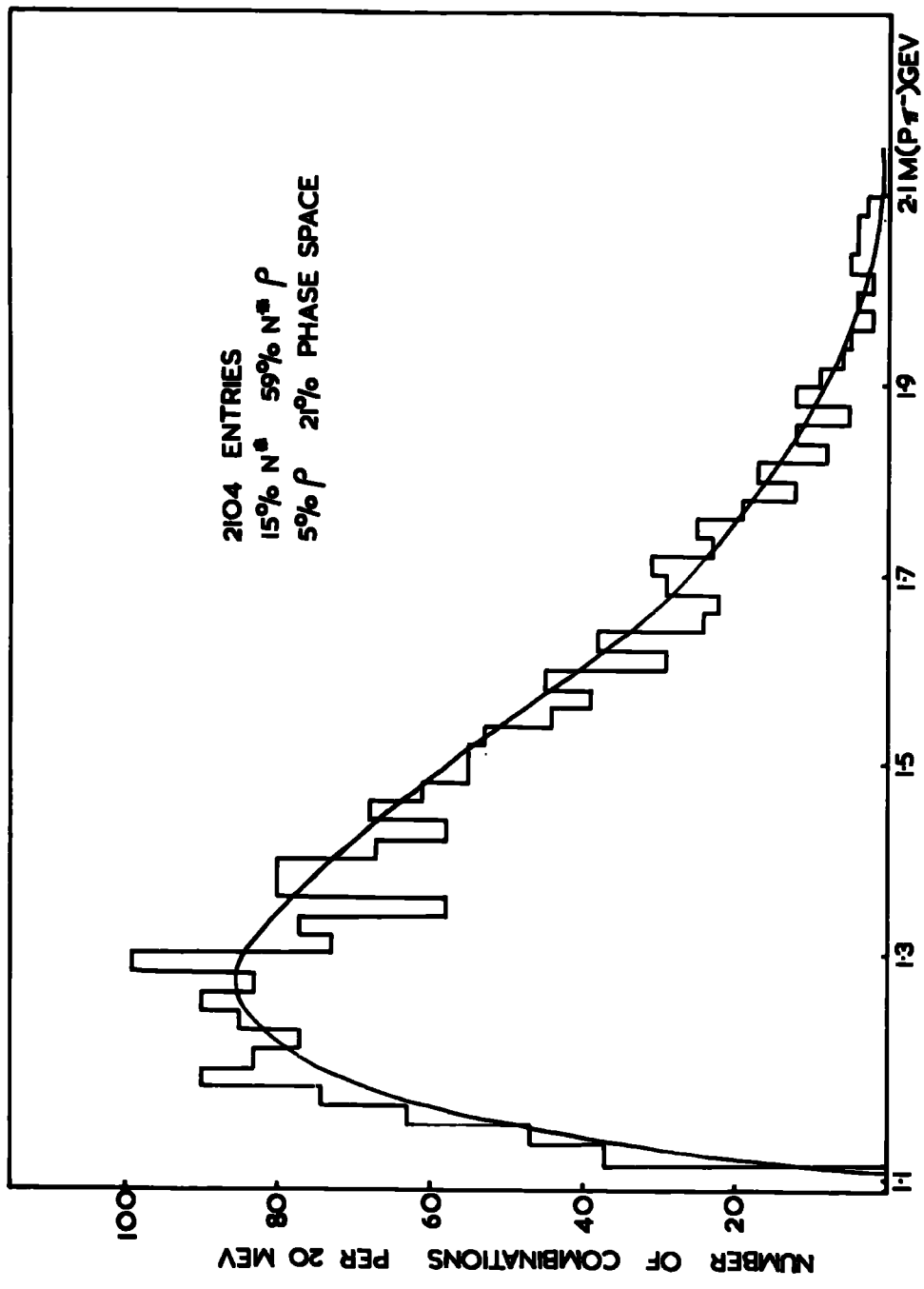


FIG. 2.5

4.24 Angular Distributions of the Secondary Particles

The angular distributions of the outgoing particles, proton, π^+ and π^- , in the centre of mass of the interaction have been plotted in figure 26. The protons show a pronounced peak in the backward direction between $-1 < \cos \theta^* < -0.75$ with a forward-backward ratio, F/B, of 0.52. The secondary π^+ mesons are almost isotropically distributed whilst the π^- mesons are peaked, though not strongly, in the forward direction. Table II below contains the results for the forward-backward ratios and the asymmetry parameter, $(F-B)/(F+B)$, for the three distributions. F and B are numbers of entries contained in the forward and backward hemispheres respectively.

TABLE II

Secondary	F/B	$(F-B)/(F+B)$
proton	0.52 ± 0.03	0.32 ± 0.02
π^+	1.09 ± 0.04	0.05 ± 0.002
π^-	1.25 ± 0.06	0.11 ± 0.01

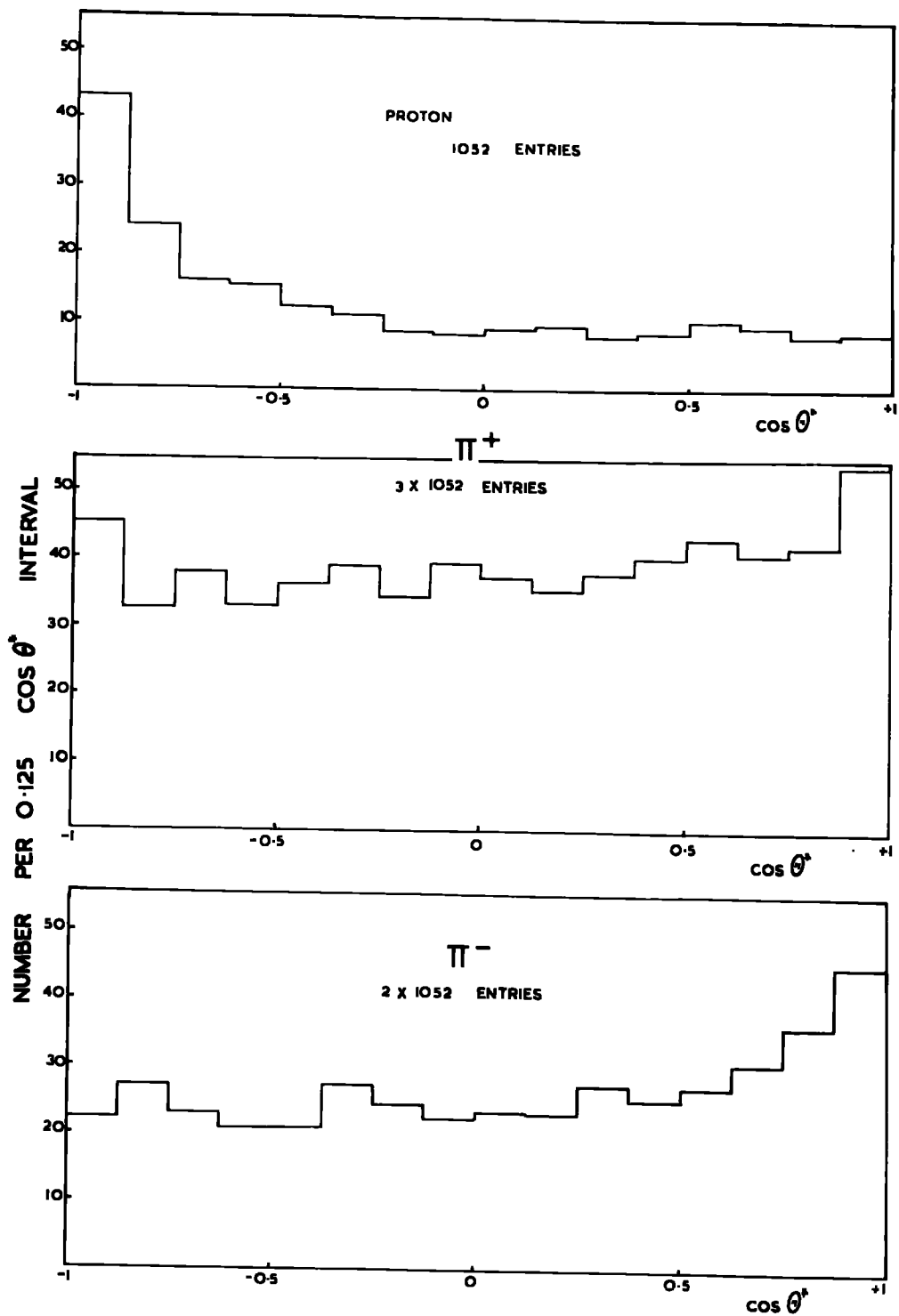
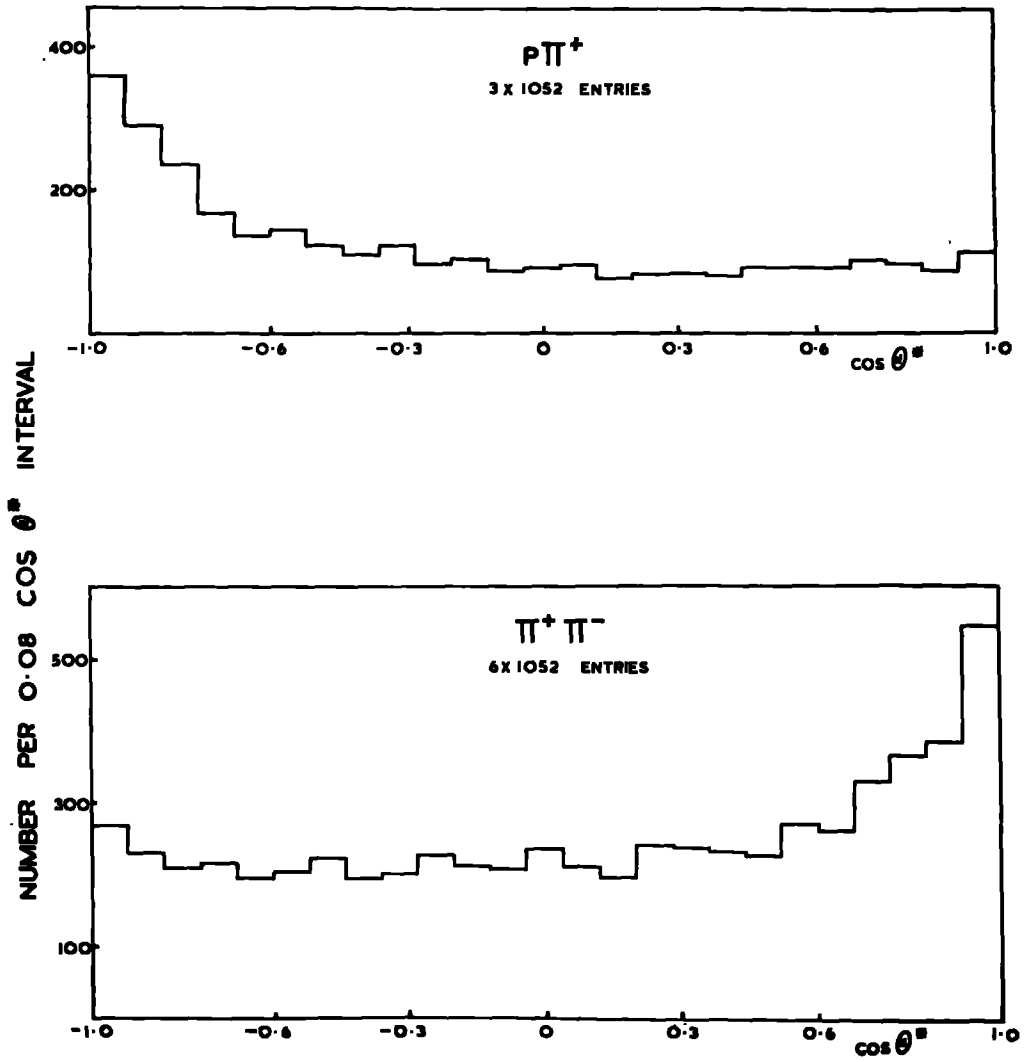


FIG.26 ANGULAR DISTRIBUTIONS IN CENTRE OF MASS.

Plotting the overall $p\pi^+$ and $\pi^+\pi^-$ angular distributions, figure 27, shows that the backward peaking of the proton is reflected in the rather broader distribution of the $p\pi^+$ whilst the forward peak of the $\pi^+\pi^-$ distribution is rather more pronounced than that of the π^- . This forward peak is attributed to the ρ^0 and examination of the distribution of those $p\pi^+$ combinations which lie in the mass region 1120 to 1320 MeV, figure 28, shows that the N^* production is strongly collimated in the backwards direction. From these distributions it is apparent that an appreciable proportion of the collisions are glancing, and peripheralism is therefore still important. The lack of a forward peak in the distribution of the π^+ is not considered to be in contradiction to this in view of the large numbers of N^* isobars which are produced backwards and whose decay products also travel predominantly in that direction.

Whilst evidence of collimation of the secondaries is found in these differential cross sections it should be noted that the F-B asymmetry is much less pronounced than in the case of interactions of smaller multiplicities. It is therefore of interest to look at the reflections of these angular asymmetries in the distribution of Δ^2 for the $p\pi^+$ and in particular for those events which both the N^* and the ρ^0 are produced.

FIG. 27 ANGULAR DISTRIBUTIONS IN CENTRE OF MASS.



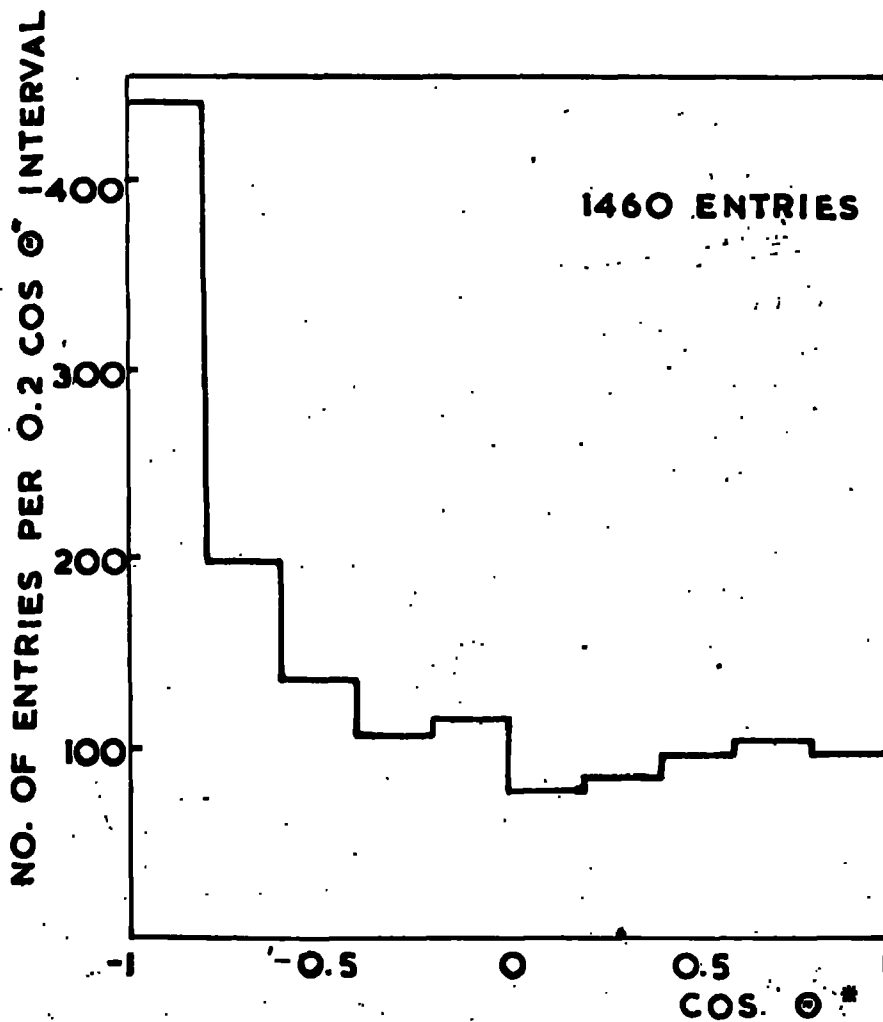
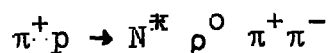


FIG.28
DISTRIBUTION OF PRODUCTION
ANGLE OF $p\pi^+$ COMBINATION FOR CONDITION
 $1120 < M(p\pi^+) < 1320$ MeV

4.25 Distribution of Δ^2 Between the Incident Proton and the $p\pi^+$

The overall distribution of Δ^2 between the incident proton and the $p\pi^+$ combination is shown in figure 29 together with the background predicted by phase space for an equal number of events. Although the observed distribution is very broad there is a marked tendency towards lower values of Δ^2 than would be expected for statistical production only. This represents the effect of the peak in the $p\pi^+$ angular distribution, Δ^2 and $\cos \Theta^*$ being related by Eq. 15. To illustrate the values of Δ^2 which are associated with the most peripheral six-prong interactions and to provide a basis for comparison with values of Δ^2 typical for quasi-two-body processes a selection has been made of the interactions of the type



where the N^* is produced in the backwards peak, $-1 < \cos \Theta^* < -0.75$. The sample has been chosen by requiring that the mass of the $p\pi^+$ taken as the N^* should lie between 1120 and 1320 MeV and that the $\pi^+\pi^-$ taken as the ρ^0 should have a mass between 670 and 850 MeV. The additional

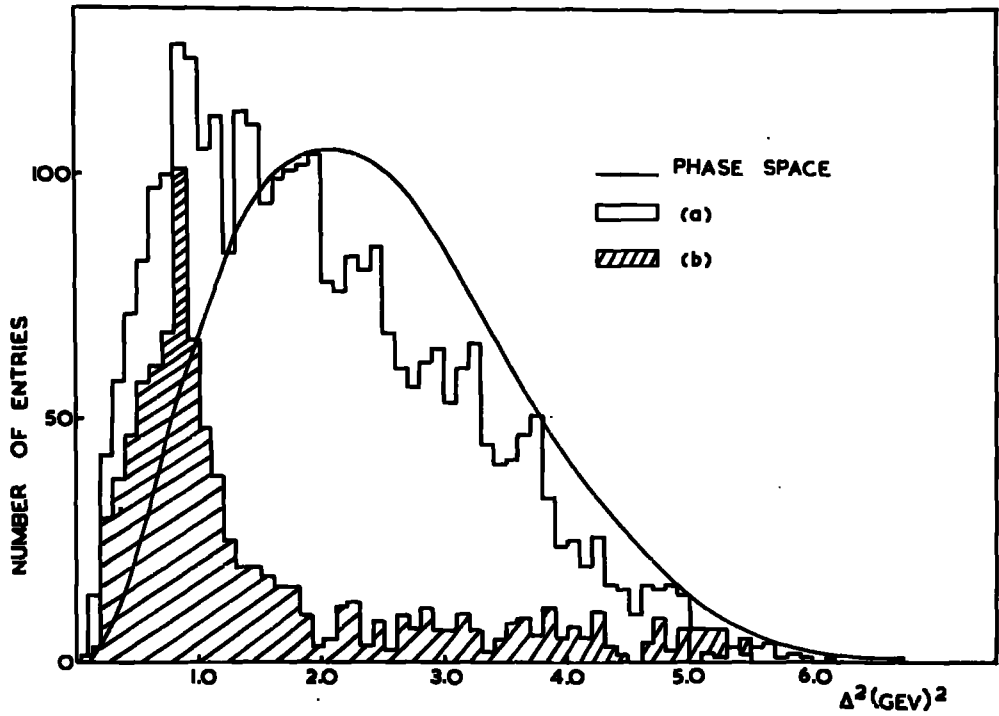


FIG.29. DISTRIBUTION OF Δ^2 ($p\pi^+/\rho$).

(a) OVERALL, 3156 ENTRIES

(b) FOR $1120 < M_{p\pi^+} < 1320$ MEV,

$670 < M_{\pi_2^+ \pi_1^-} < 850$ MEV,

$-1 < \cos \theta^* < -0.75$, 894 ENTRIES.

angular condition also represents a constraint upon Δ^2 and the phase space for the sample will, as a result of this, be peaked at small values of Δ^2 . This distribution must, however, lie within the phase space for all the events. It can be seen in figure 29 that the observed distribution of the sample has a significant peak outside even the overall phase space and this may be considered to be confirmation of the peripheralism of the events in which the N^{π} is produced backwards. The peak is centred at 0.8 (GeV)^2 , and it is apparent that, although the tendency to small values of Δ^2 is significant, the momentum transfers typical of a peripheral interaction of high multiplicity are much larger than those characteristic of quasi-two-body interactions with four or five particles in the final state. Small partial waves evidently are still of importance for peripheral interactions of high multiplicity. Greater momentum transfers are to be expected generally for interactions of higher multiplicity simply in order to create the larger number of particles but it seems unlikely that quasi-two-body interactions should occur with such high values of Δ^2 unless the exchange particle were particularly massive. It may be that the peripheralism of the six-pronged interactions has a more complicated explanation in terms of multi-peripheral diagrams with several vertices (Amati and Stanghellini, 1962)

4.26 Three-pion Effective mass Distributions,
 $\pi^+\pi^+\pi^-$ and $\pi^+\pi^-\pi^-$

The results have been examined for evidence of the production of the A_1 and A_2 particles both of which are reported to decay principally by way of the $\pi\rho$ mode (Chung et al., 1964 and others). There is still some uncertainty concerning the enhancement, seen in the region of 1100 MeV in the $\pi\rho$ mass distributions of these experiments, which is tentatively attributed to the A_1 resonance. Deck (1964) has suggested that the peak could be the result of kinematic effects whereby $\pi\rho$ masses just above threshold are favoured. Certainly the independently reported enhancements which are found in both charged and neutral modes cannot be explained as statistical fluctuations. The interpretation of the peak at 1320 MeV in the $\pi\rho$ system as a genuine resonance is well established and enhancements have also been observed at this mass in the $K\bar{K}$ and π systems (Chung et al., 1964 and the Anglo-German Collaboration, 1964). If these are decay modes of the same particle then the quantum numbers of the A_2 are established to be, in the usual notation, $J^{PG} = 2^{+-}$. The isospin is $I = 1$ found from the observation of both charged

and neutral forms of the A_2 .

The present experiment should be very suitable to observe resonances which decay into a ρ^0 and a π^+ or π^- as there is abundant formation of the ρ^0 and there are additional pions besides those associated with the N^* and the ρ^0 . Furthermore, it has been pointed out that the peripheralism of the six-pronged events is not dominated so completely by high partial waves as are four and five pronged interactions so that kinematic effects dependent upon very low momentum transfers should not be important. The overall effective mass distributions for the $\pi^+\pi^+\pi^-$ and $\pi^+\pi^-\pi^-$ combinations are shown in figures 30 and 31. Surprisingly there are no significant enhancements in either distribution. The background of the $\pi^+\pi^-\pi^-$ distribution is not in good agreement with the observed spectrum but this is thought to be the result of some dynamical reflections of the production which cannot be included in the computation of the background using FOWL. If the mass distributions for the two pion combinations above are plotted with the requirement that one $\pi^+\pi^-$ combination should lie in the mass region of the ρ^0 (670 to 850 MeV) there is still no indication of any resonance production.

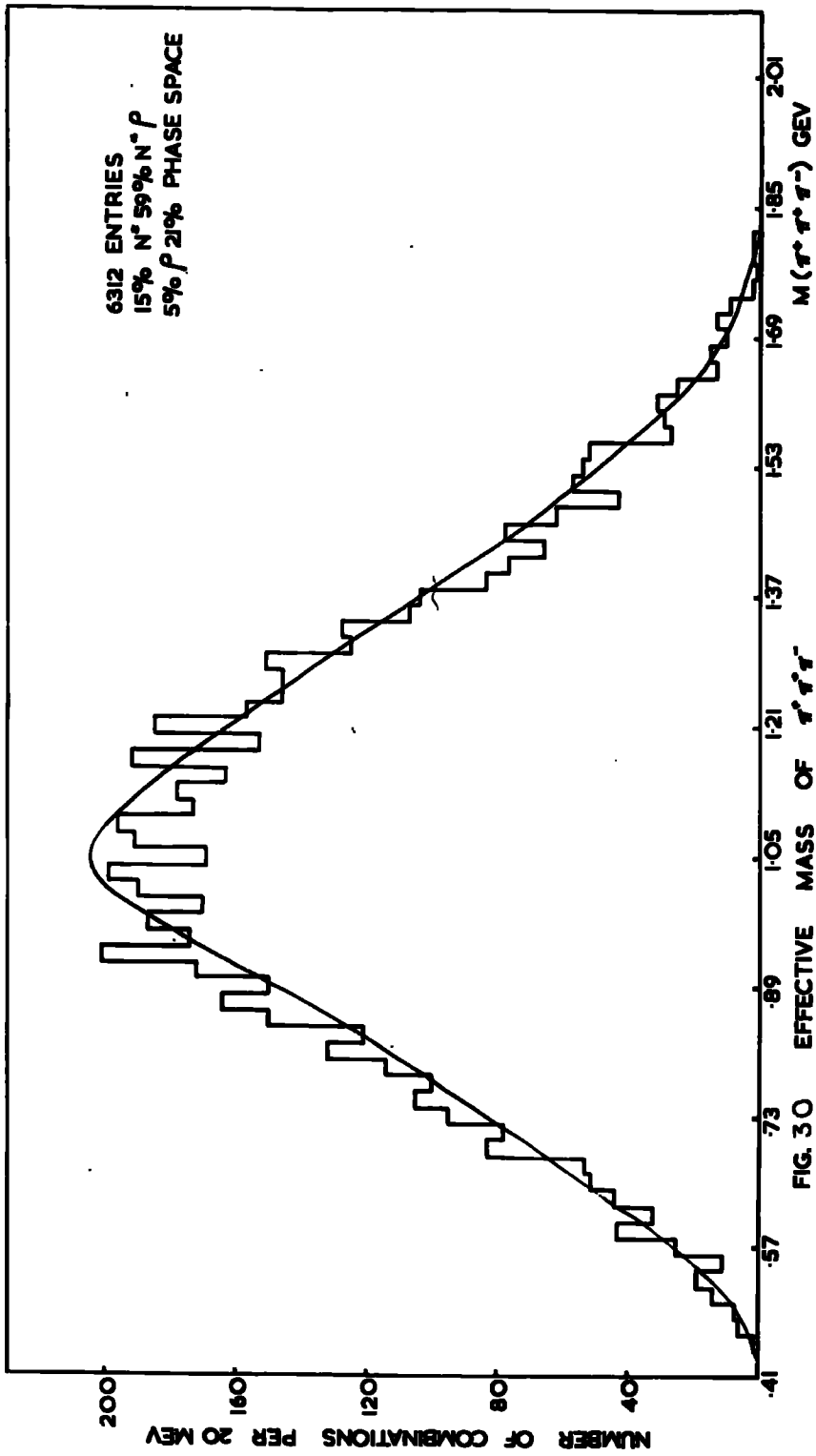


FIG. 30

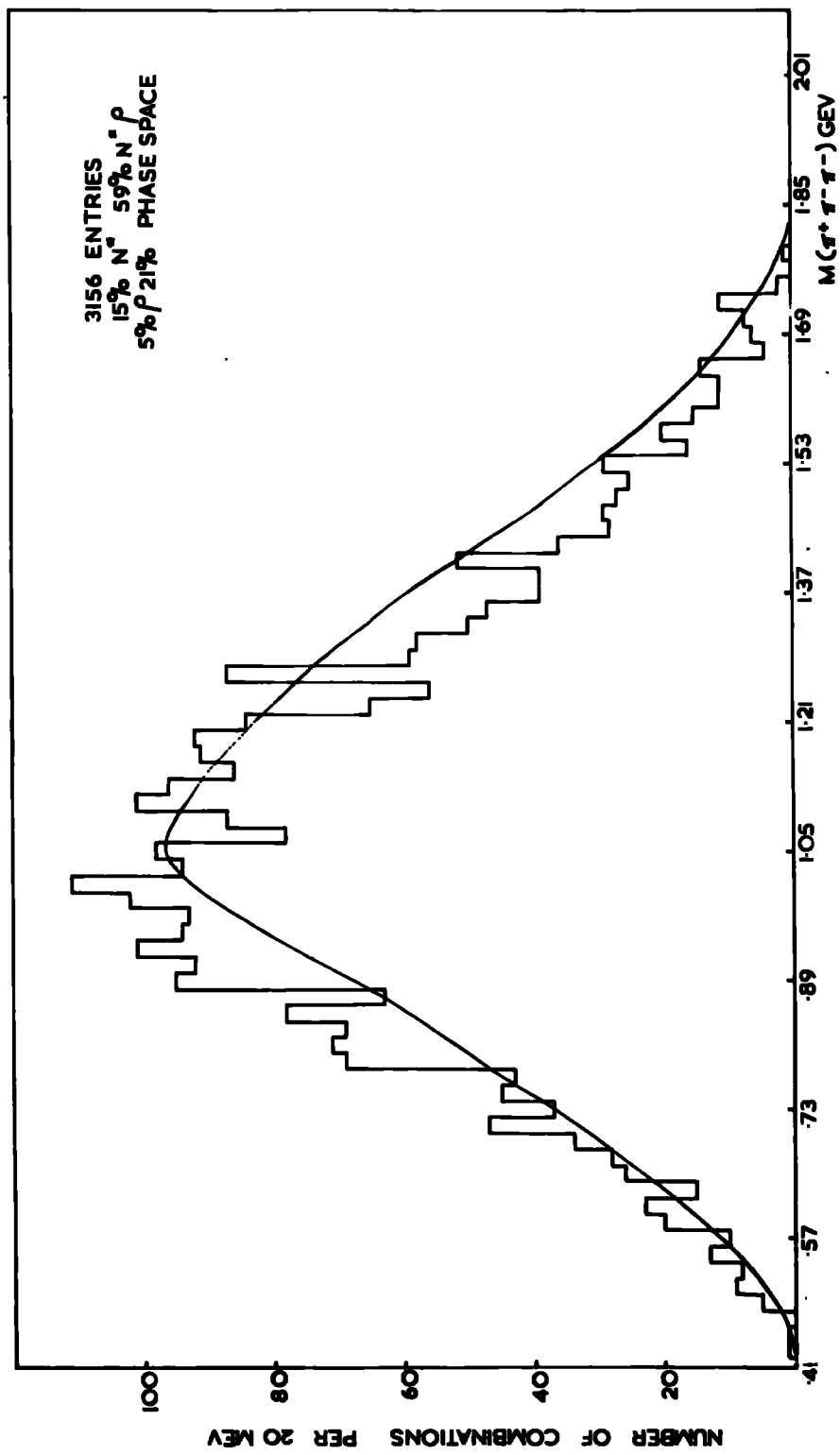
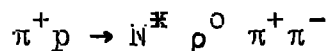


FIG. 31 EFFECTIVE MASS OF π⁺ π⁻ π⁺ π⁻

only when the additional condition is imposed that there should be a π^+ combination in the mass region of the N^* moving backwards ($-1 < \cos \Theta^* < -0.75$) is any evidence for a $\pi\rho$ resonance observed. Figure 32 shows the effective mass distribution for the $\rho^0\pi^+$ combination in these events which must largely be of the kind



and an enhancement is seen, centred at 1300 MeV, which may be attributable to the A_2 . The distribution has been plotted together with a normalised control distribution produced for the same mass restrictions but for the angular region $-0.75 < \cos \Theta^* < 0$. Against this background the enhancement has about a three standard deviation effect. The smaller enhancement observed in the same distribution at about 1000 MeV is about two standard deviations above the background but it has the asymmetric appearance of a statistical fluctuation. In the complementary distribution for the $\pi^-\rho^0$ with the same conditions there are no enhancements and this casts doubt upon the peak at 1300 MeV in the $\pi^+\rho^0$ system. The surprising result of this study seems to be that in the six-pronged interactions there is essentially no production of the A_1 or A_2 particles in

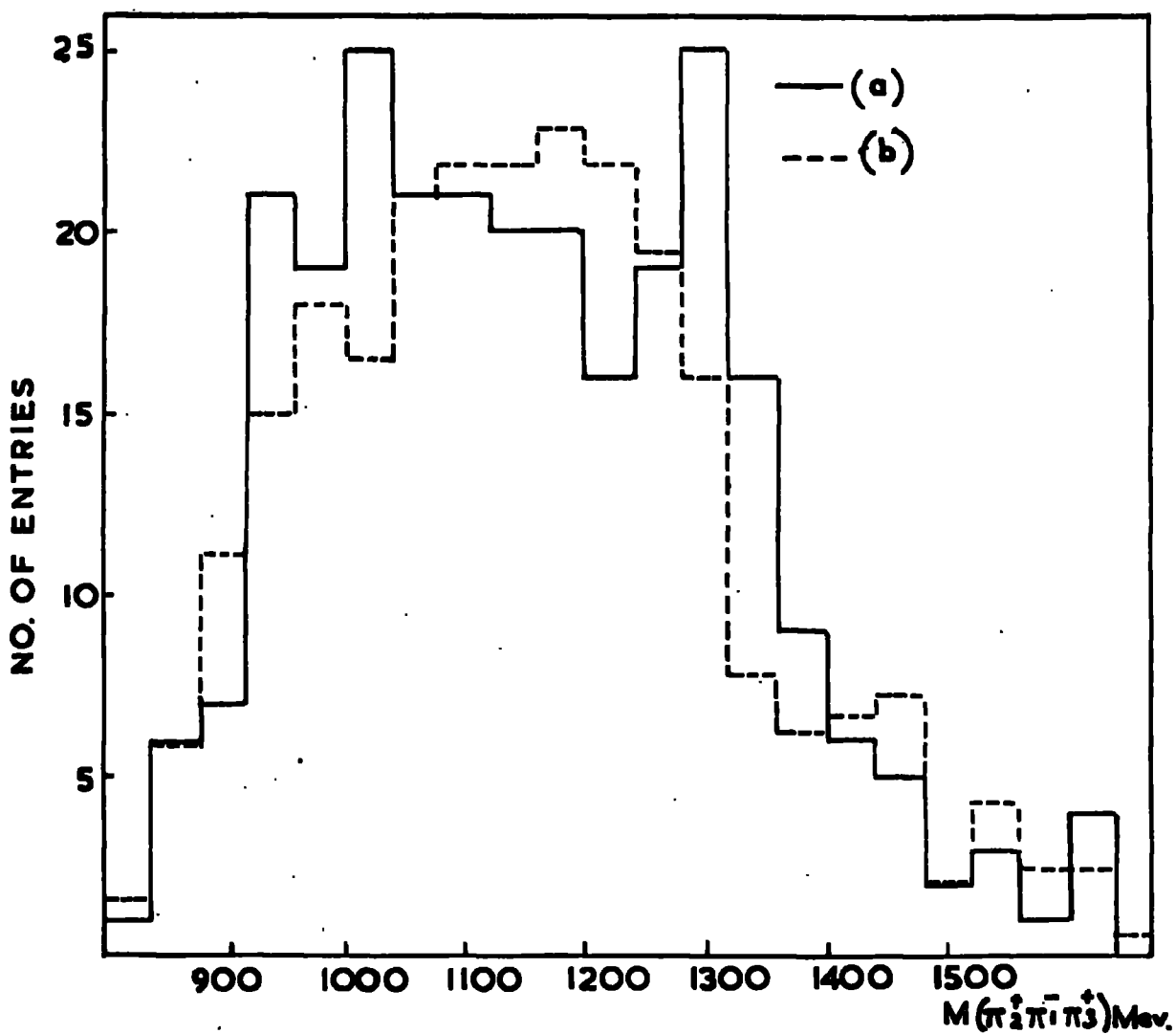


FIG. 32.

Effective Mass of $\pi_2^+ \pi_1^- \pi_3^+$ for

$$1120 < M(p\pi_1^+) < 1320 \text{ Mev.}$$

$$670 < M(\pi_2^+ \pi_1^-) < 850 \text{ Mev.}$$

and

$$(a) \quad -1 < \cos \Theta_{p\pi_1^+} < -0.75.$$

$$(b) \quad -0.75 < \cos \Theta_{p\pi_1^+} < 0.$$

spite of the general importance of ρ^0 formation. In view of the lack of evidence for the production of the A_2 which is considered to be a genuine resonance it is not possible to put forward any evidence against the A_1 .

4.27 Four-pion Effective mass Distribution $\pi^+\pi^+\pi^-\pi^-$

The effective mass distribution of the $\pi^+\pi^+\pi^-\pi^-$ combination is shown in figure 33 and it can be seen that in spite of the rather poor agreement of the background there are no statistically significant enhancements. Any important quasi-two-body processes involving the N^* and a four-pion resonance are therefore considered to be unlikely. Imposing various conditions on to the selection of events does not have the effect of revealing any peaks which are difficult to see on account of the background. Both the f^0 meson and the recently reported g particle (Goldberg et al., 1965), which has a mass of about 1670 MeV, may be expected to decay into this four-pion mode but peaks in these regions are not seen and no conclusions can be derived about the upper limit of the branching ratios of these particles into two and four pions until the full analysis has been made of the four-pronged events.

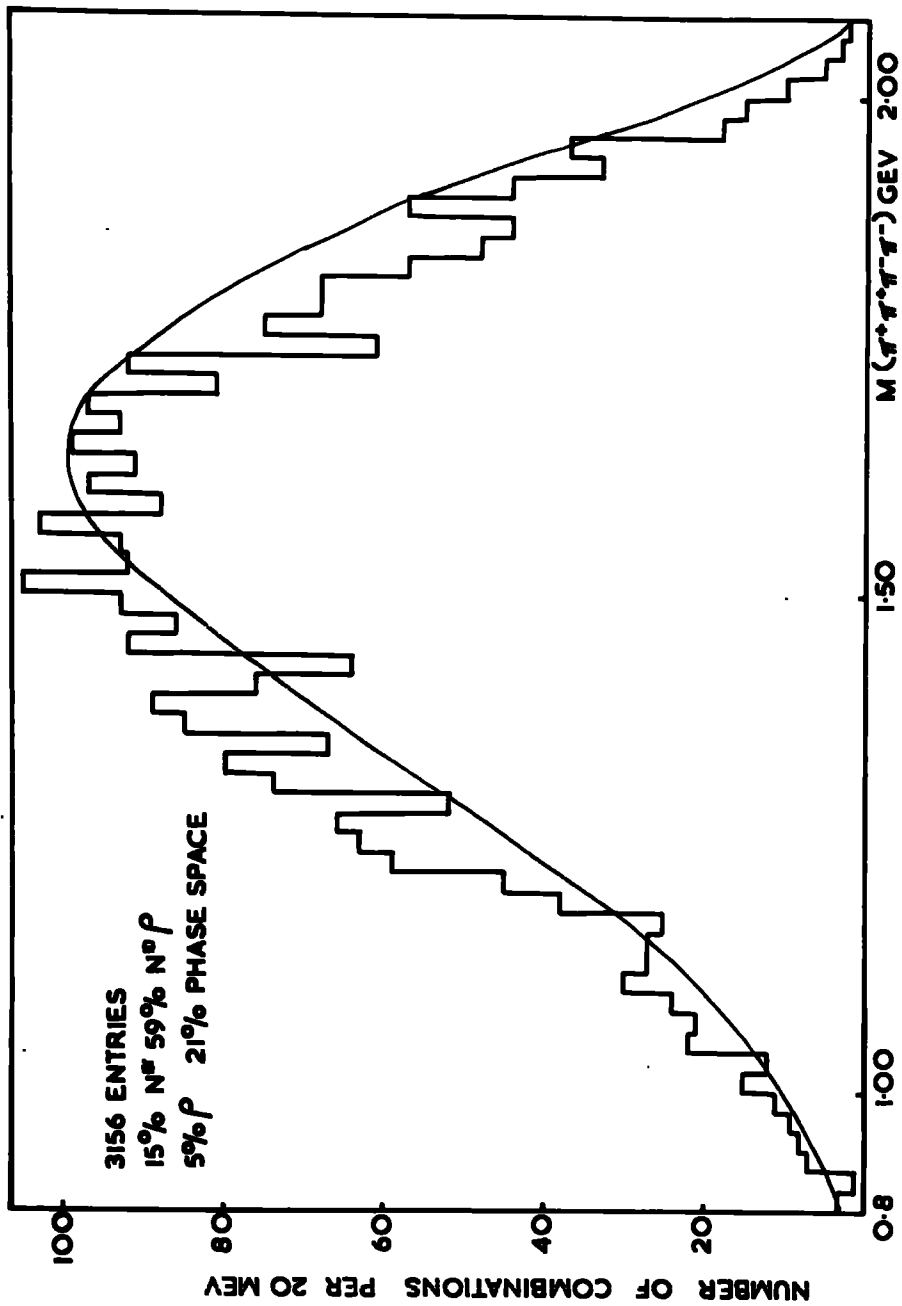


FIG. 33 EFFECTIVE MASS OF $\pi^+\pi^+\pi^-\pi^-$

4.28 Higher Nucleon Isobars

The possible production of higher nucleon isobars being produced in the interaction and later decaying into the N^* has been investigated by looking for enhancements in the effective mass distributions of the combinations $p \pi^+ \pi^+$, $p \pi^+ \pi^-$, $p \pi^+ \pi^- \pi^-$, and $p \pi^+ \pi^+ \pi^-$ which are shown in figures 34 to 37. The backgrounds are not all in very good agreement but none of the deviations seem to be statistically significant and they are not enhanced by making selections of those events in which a $p \pi^+$ combination in the mass region of the N^* moves backwards. It seems that higher nucleon isobars are not a feature of the six-pronged interactions. Taking into account the negative results in the search for the multi-pion resonances (other than the ρ^0) it is clear that the quasi-two-body processes which are favoured in four and five particle final states do not occur with appreciable frequency for these interactions of higher multiplicity.

4.29 Decay Distribution of the $\pi^+ \pi^-$

The distribution of the decay angle of the dipion combinations in the ρ^0 band has been examined in a

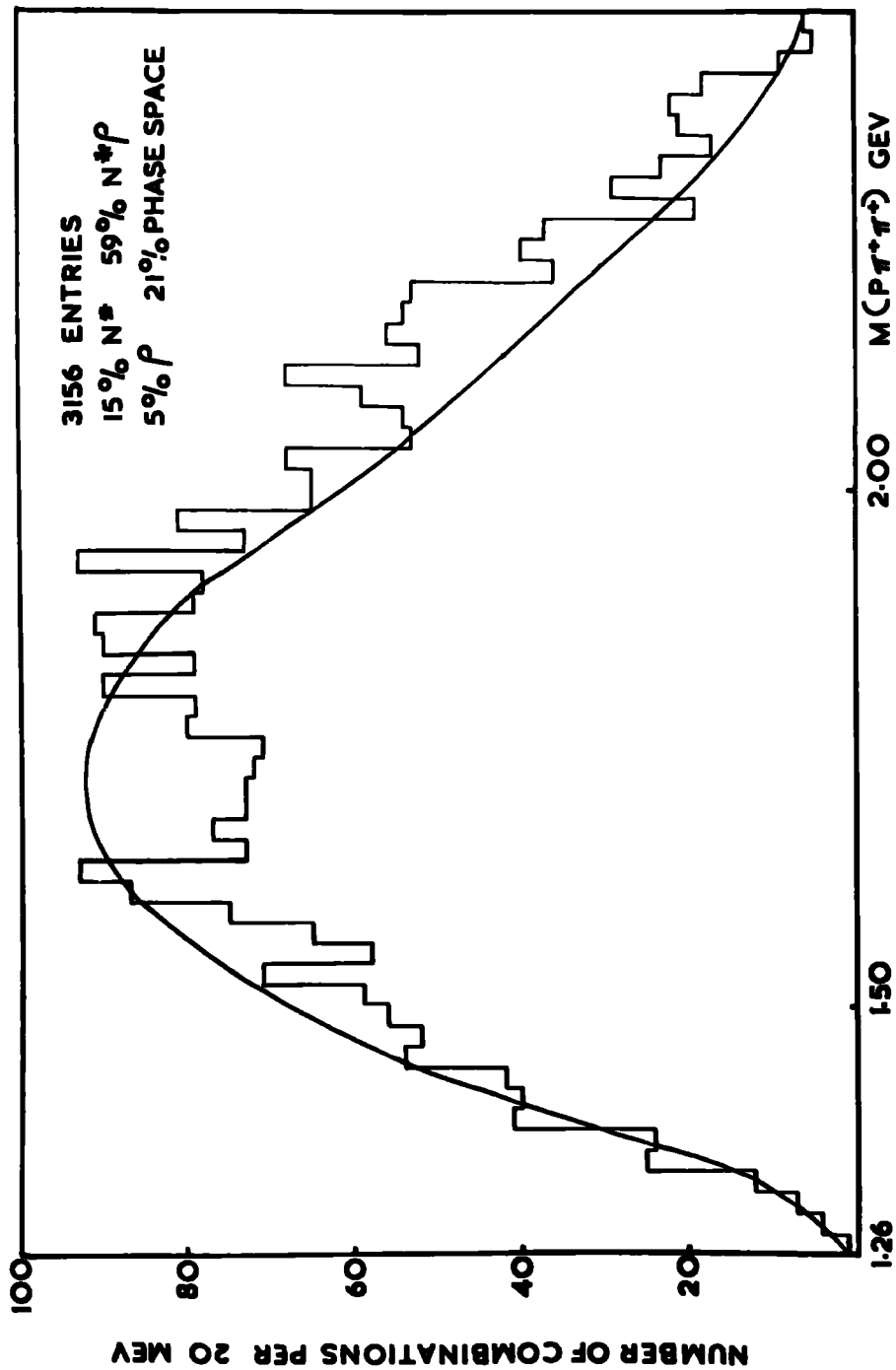


FIG. 34 EFFECTIVE MASS OF $\pi^+ \pi^-$

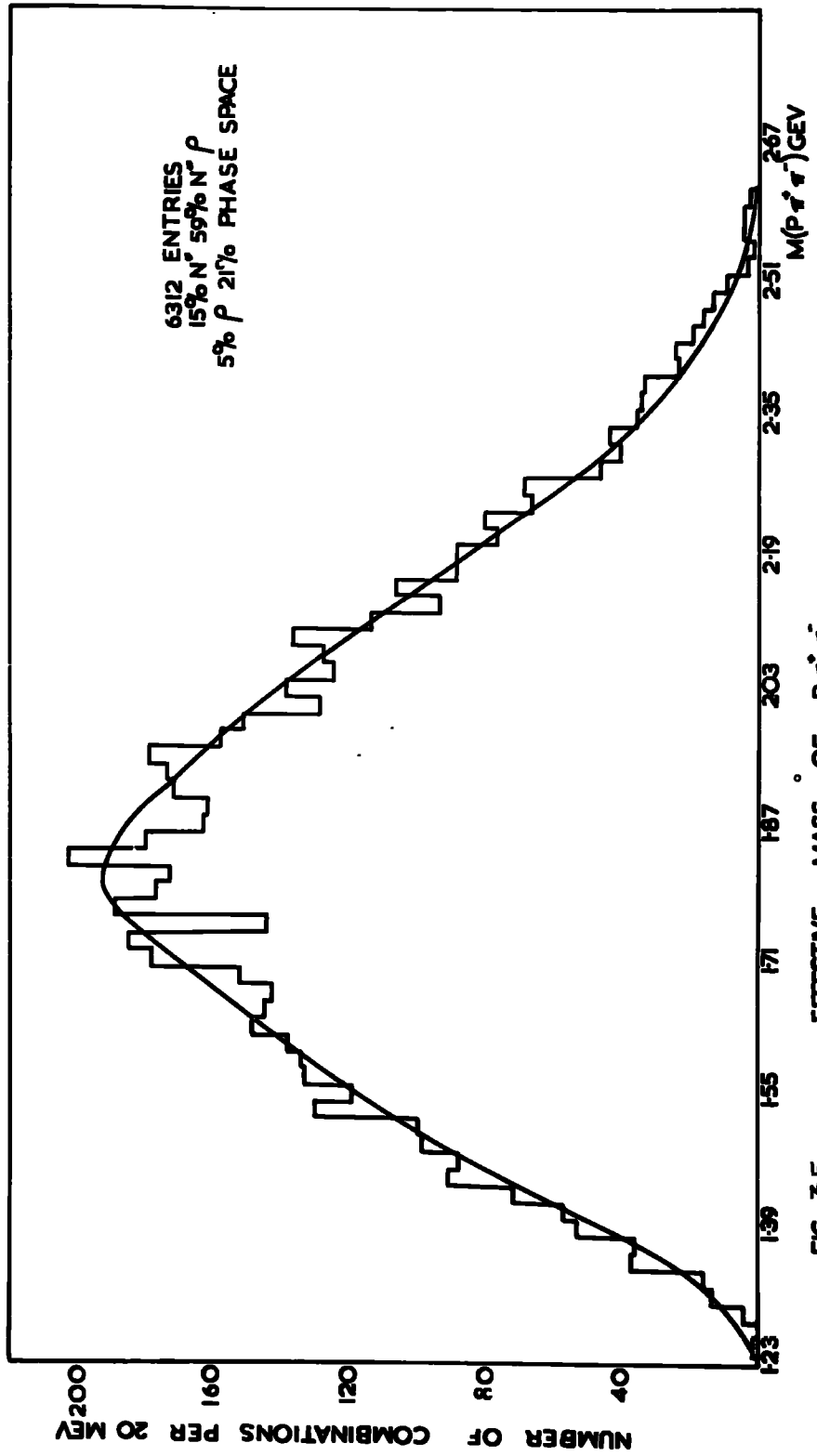


FIG. 35

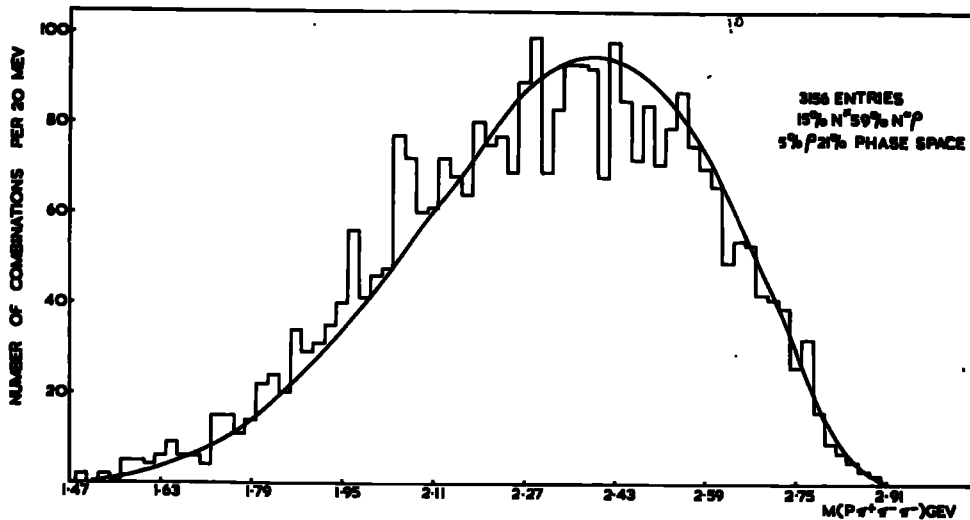


FIG. 36 EFFECTIVE MASS OF $P\pi^+\pi^-\sigma^-$

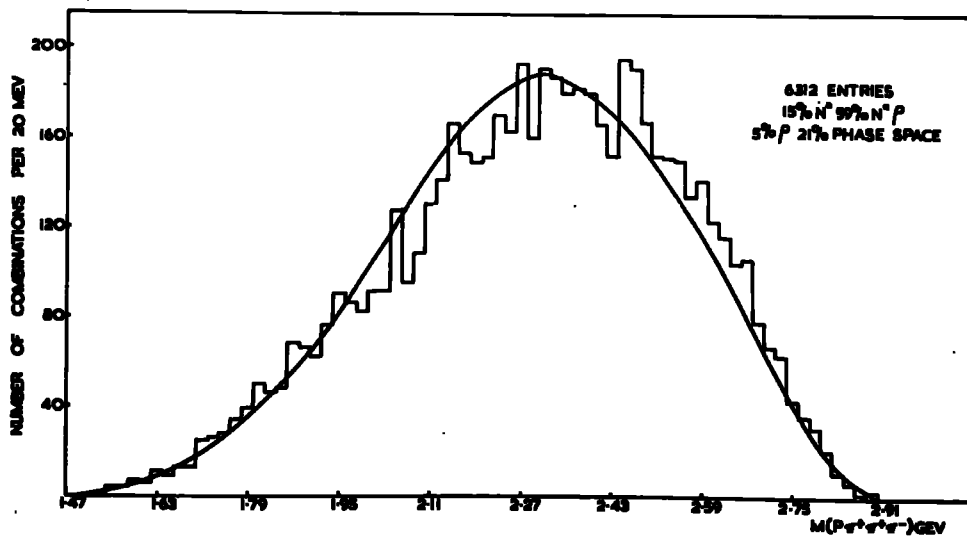
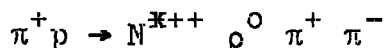


FIG. 37 EFFECTIVE MASS OF $P\pi^+\pi^-\sigma^-$

sample of peripheral events of the type



The usual constraints upon the mass and angle of the $N^{\kappa++}$ have been imposed, $1120 < m_{\rho\pi^+} < 1320$ MeV and $-1 < \cos \theta^{\kappa} < -0.75$ respectively, and the ρ^0 mass region has been taken between 670 and 850 MeV. The angle of decay, θ_d , has been defined as the angle between the direction of the π^+ meson in the centre of mass of the ρ^0 and the direction of the ρ^0 . The resulting distribution for the conditions given is shown in figure 38(a). The distribution does not appear to be consistent with isotropy and a curve of the form $1 + a \cos^2 \theta_d$ has been fitted by a least squares method. For the ten observed values of $\cos \theta_{\text{decay}}$ the value of χ^2 for the best fit, $1 + 1.65 \cos^2 \theta_d$, is 20.5 and may be compared with $\chi^2 = 29.5$ for an isotropic distribution. In case the effect might be the result of kinematic reflections from the pion decaying from the nucleon isobar two control regions have been plotted, figures 38(b) and (c), for the dipion mass regions on either side of the ρ^0 band, 490 to 670 MeV and 850 to 1010 MeV. Both distributions are essentially isotropic and it is believed therefore that the decay asymmetry of the ρ^0 region is a real effect indicating a spin polarization of the resonance in its

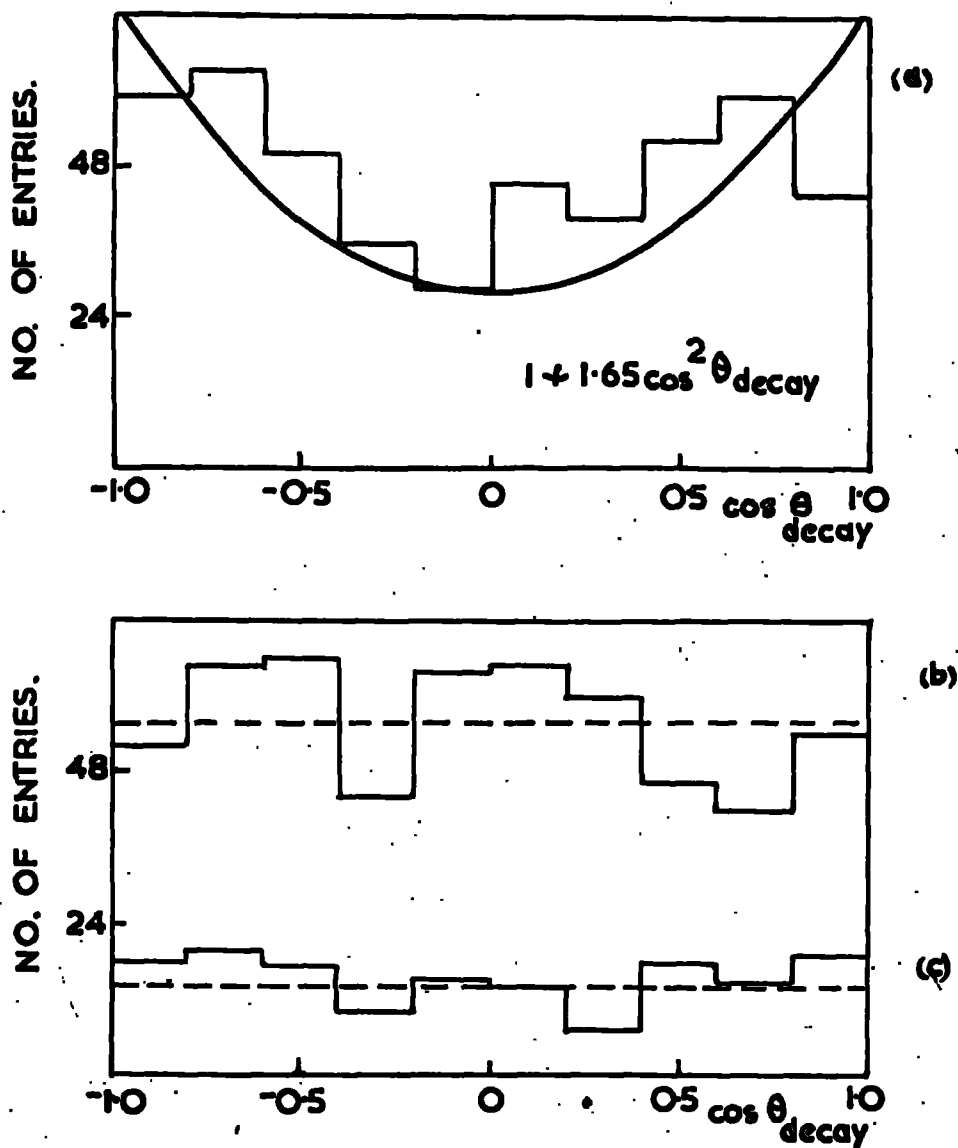


FIG. 38. Decay distribution of $\pi_2^+ \pi_1^-$ for

$$1120 < M_{p\pi_1^+} < 1320 \text{ Mev}$$

$$-1 < \cos \theta_{p\pi_1^+} < -0.75$$

and

(a) $670 < M_{\pi_2^+ \pi_1^-} < 850 \text{ Mev}$ 474 entries.

(b) $490 < M_{\pi_2^+ \pi_1^-} < 670 \text{ Mev}$ 564 entries.

(c) $850 < M_{\pi_2^+ \pi_1^-} < 1010 \text{ Mev}$ 153 entries.

production. To confirm this tentative conclusion experiments at higher energies would prove helpful as the control region 850 to 1010 MeV does not contain many events in the present experiment.

CONCLUSIONS

An experiment has been reported in which the elastic scattering of 6 GeV/c π^+ mesons in deuterium has been investigated. The observed differential cross section is in very good agreement with the prediction of the impulse approximation to high energy diffraction scattering when the deuteron form factor is derived from a hard core wave function. It is shown that the Hulthen wave function does not provide an adequate description of the structure of the deuteron. The diffuseness of the deuteron does not allow the optical model description of elastic scattering to be extended to this light nucleus.

In a second experiment which has been reported on the high multiplicity interactions of 5 GeV/c π^+ mesons in hydrogen the partial cross sections have been determined for the different channels leading to six charged particles in the final state and these have been shown to be increasing rapidly with energy. The 4C channel is dominated by the production of the $N^*(1236)$ and of the ρ^0 ; there is no evidence to show that these are the products of the decays of heavier resonances. There is a surprising absence of any significant enhancements in the πp system and in particular there is no evidence for the A_1 and apparently

only a small number of A_2^+ particles are formed. The examination of the effective mass distribution of the four-pion combination, $\pi^+\pi^+\pi^-\pi^-$, does not reveal any evidence for the four-pion decay modes of the f^0 or the g particles. The ρ^0 is therefore essentially the only pion resonance observed in the interactions. The search for higher nucleon isobars has also produced no positive result and it seems that quasi-two-body processes do not play any significant part in interactions of very high multiplicity.

The angular distributions of the secondaries, and in particular that of the $\pi\pi^+$ combinations in the N^* mass region, show that a significant proportion of the resonances are produced in glancing collisions. In view of the absence of quasi-two-body processes it seems unlikely that the interactions take place by the exchange of a single particle; such an exchange particle would have to be very massive to lead to the comparatively broad angular distributions. Perhaps a multi-peripheral model with several vertices should be used to explain the association of the two pions which do not take part in the N^* and ρ^0 resonances. The six particle final state is apparently

reached through a more complicated production mechanism than that of four and five particle systems and is dependent upon smaller partial waves.

A decay asymmetry of the ρ^0 is observed in the most peripheral interactions which seems to be the result of polarization of its angular momentum at production. Confirmation of this effect should be looked for in experiments at higher energies where possible kinematic effects could be more easily distinguished.

ACKNOWLEDGEMENTS

The author wishes to thank Professor G.D. Rochester for his encouragement and for his interest in the work. The author is especially indebted to Drs. A.J. Apostolakis and J.V. Major who have provided guidance for this work at all stages. He wishes to thank the other colleagues with whom he has worked and in particular Dr. A.D. Martin for many helpful discussions. Of the many members of the technical staff who have assisted in various ways the author would like to thank Mrs. E. Errington, Miss T. Jopling, Miss A. McKellar and Miss J. Watson for their painstaking work in the scanning and measurement of the photographs, Miss C. Guyll and Mr. R. White for assistance with the preparation of diagrams, and Mr. E. Lincoln, Mr. W. Mounsey and Mr. D. Jobling for their help in building the measuring tables. He would also like to thank Miss R. Noble for typing the thesis in its final draft. Thanks are due to the personnel at CERN who enabled the exposures to take place. The author would like, finally, to thank the D.S.I.R. for a maintenance grant during three years and for travelling grants.

REFERENCES

Aachen-Berlin-Bonn-Hamburg-Munich Collaboration,
1966, DESY Report DESY 66/11

Amati D. and Stanghellini A.,
1962, Nuovo Cimento, 26, 896.

Anglo-German Collaboration: Aachen-Berlin-Bonn-Birmingham-
Hamburg-London (I.C.)-Munich,
1964, Phys. Letters, 10, 226,
1965, Phys. Rev., 138, B 897.

Bellettoni G., Cocconi G., Diddens A.W., Lillethun E.,
Matthiae G., Scanlon J.P., Wetherell A.M.,
1965, Phys. Letters, 19, 341,
1966, Nuclear Physics, 79, 609.

Boldt E., Duboc J., Duong N.A., Eberhard P., George R.,
Henri V.P., Levy F., Poyen J., Pripstein . ., Cussard J.,
and Tran A.,
1964, Phys. Rev., 133, B220

Burhop E.A.S.,
1962, Proceedings of the CERNS Master School, 275.

Crang S.O., Dahl O.I., Hardy L.M., Hess R.I., Kalbfleisch G.R.,
King J., Miller D.H., and Smith G.A.
1964, Phys. Rev. Letters, 12, 621.

Deck R.T.,
1964, Phys. Letters, 13, 169

Evans R.D.,
1955, The Atomic nucleus, 315.

Fernbach S., Serber R., Taylor T.B.,
1949, Phys. Rev., 75, 1352

Fernbach S., Green F.A., Watson K.M.,
1951, Phys. Rev., 82, 980.

Ferrari E., and Selleri F.,
1962, Nuovo Cimento Suppl., 2r, 453.

Fowler P.H., and Perkins D.H.,
1958, Private Communication quoted in
Allen J.E., Apostolakis A.J., Lee Y.T., Major J.V., Perez
Ferreira E.,
1959, Phil.Mag., 4, 858.

Franco V., and Glauber R.J.,
1966, Phys. Rev., 142, 1195

Galbraith W., Jenkins S.W., Kycia T.F., Leontic B.A.,
Phillips P.H., Read A.L., Rubinstein R.,
1965, Phys. Rev., 137, 893

Gartenhaus S.,
1956, Phys. Rev., 100, 900.

Goldberg J., and Perreau J.M.,
1963, CERN Internal Report, CERN 63-12

Goldberg J., Judd F., Vegni G., Wingeler H., Fleury P.,
Huc J., Lestienne R., De Rosny G., Vanderhaghen R.,
1965, Phys. Letters, 17, 354.

Gottfried K., and Jackson J.D.,
1964, Nuovo Cimento, 34, 735.

Magopian V., Selove W., Alitti J., Baton J.P., Neveu-Rene M.,
Gessaroli R., and Romano A.,
1965, Phys. Rev. Letters, 14, 1077.

Harrington D.R.,

1964, Phys. Rev., 135, B358

Jackson J.D.,

1964, CERN Internal Report 8622/TH. 416

1965, Revs. Modern Phys., 37, 484, from data of

Saclay-Orsay-Bari-Bologna Collaboration,

1964, Proceedings of Dubna Conference.

Keil E., and Neale W.W.,

1963, CERN Internal Report, CERN/TC/02 63-3.

Kellner G.,

1965, CERN Internal Report, CERN/TC/WBC 65-4

Kirillova L., Nikitin V., Pantuev V., Strunov L.,

Khachatryan M., Khristov L., Shafranov M., Korbel Z.,

Rob L., Damyanov S., Zlatanov V., Jordanov V., Dalkhazhav N.

Tuvdendorzh D.,

1964, Dubna Preprint, E-1820

Lock W.O.,

1960, High Energy Physics, 45

Moravcsik M.J.,

1958, Nuclear Physics, 7, 113

Schmitt M.,

1965, Proceedings of the CERN Easter School, 1, 1.

Welford W. T.,

1963, Applied Optics, 2, 981.

